Variability of age of air derived from MIPAS SF_6 measurements

Zur Erlangung des akademischen Grades eines
DOKTORS DER NATURWISSENSCHAFTEN
von der Fakultät für Physik des
Karlsruher Instituts für Technologie (KIT)

genehmigte

DISSERTATION

von

Dipl.-Phys. Florian Johannes Haenel

aus Heidelberg

Tag der mündlichen Prüfung:	27. Januar 2017
Referent:	Prof. Dr. Johannes Orphal
Korreferent:	PD Dr. Michael Höpfner

Summary

A new and improved setup of the SF_6 retrieval together with a newly calibrated version of MIPAS-ENVISAT level 1b spectra (version 5, ESA data version 5.02/5.06) was used to obtain a new global data set of vertically resolved SF_6 mixing ratios, covering the total observational period of MIPAS from July 2002 to April 2012 for the first time. This data set was validated with balloon-borne in-situ measurements as well as with data from the other renowned satellite instrument measuring SF_6, the Atmospheric Chemistry Experiment Fourier Transform Spectrometer (ACE-FTS). Monthly and zonally averaged SF_6 vertical profiles were converted into mean age of air (AoA) using a tropospheric SF_6 reference curve. The obtained data set of age of air was compared to airborne age of air measurements. The temporal evolution of the mean age of air was then investigated in 10° latitude and 1–2 km altitude bins. A regression model consisting of a constant and a linear trend term, two proxies for the quasi-biennial oscillation variation, sinusoidal terms for the seasonal and semiannual variation and overtones was fitted to the age of air time series. The annual cycle of age of air for particular regions in the stratosphere was investigated and compared to other studies. The age of air trend over the total MIPAS period consisting of the linear term was assessed and compared to previous findings of Stiller et al. [2012]. While the linear increase of mean age is confirmed to be positive for the northern midlatitudes and southern polar middle stratosphere, differences are found in the northern polar upper stratosphere, where the mean age is now found to increase as well. The magnitude of trends in the northern midlatitude middle stratosphere is slightly lower compared to the previous results and the trends fit remarkably well to the trend derived by Engel et al. [2009] for northern midlatitudes. Negative age of air trends found by Stiller et al. [2012] are confirmed for the lowermost tropical and southern midlatitudinal stratosphere. Differences to the previous data versions occur in the middle tropical stratosphere around 25 km, where the age trends are now negative. Overall, the new latitude–altitude distribution of trends appears to be less patchy and more coherent than the previous one. In addition, different sensitivity studies on the calculation of age of air have been carried out, including a further developed non-linearity correction with simulated age of air spectra as opposed to the traditional method where an inverse Gaussian function was used to parametrise the age spectrum as a function of the mean

age. Age of air trend patterns were found to be robust with respect to these variations of the analysis method. Applying the same methods as for MIPAS, it was tried to infer decadal age of air trends also from ACE-FTS SF_6 data. Even though data coverage is very sparse, significant positive decadal trends for the northern midlatitudes were found also for this data set. The hemispheric asymmetry of negative age of air trends in the Southern Hemisphere, and positive trends in the Northern Hemisphere was found to be consistent with simulations by the Lagrangian chemistry transport model CLaMS driven by ERA-Interim data. The decadal trends are also compared to trends calculated from SF_6 mixing ratios simulated by the Karlsruhe Simulation Model of the Middle Atmosphere (KASIMA) and good agreement is found.

While CLaMS model calculations for the MIPAS period have shown that trends in AoA can often be attributed to trends in mixing processes and not necessarily to circulation changes, the negative AoA trends in the southern midlatitudinal lowermost stratosphere could unambiguously be attributed to an accelerating shallow branch of the Brewer-Dobson circulation.

Contents

Chapter 1

Introduction

The Earth's atmosphere is usually classified into different layers based on the vertical temperature profile. The lowest layer is the troposphere, which contains about 80% of the atmosphere's mass and is characterised by a decrease of temperature with altitude. The upper boundary of the troposphere, called the tropopause, is defined by the region where the vertical temperature gradient changes sign. This minimum in temperature is found at altitudes between 17 to 18 km in the tropics and at about 9 to 13 km in higher latitudes. In the layer above, the stratosphere, temperature increases with altitude mainly due to solar short-wave absorption by ozone, the most prominent trace gas in the stratosphere. The temperature maximum is reached at the stratopause at approximately 50 km, where the vertical temperature gradient again changes sign. The mesosphere extends from the stratopause to about 80 km altitude and exhibits a decreasing temperature profile reaching its minimum at the mesopause, where the lowest temperatures of the atmosphere are found. The so-called "middle atmosphere" comprises stratosphere and mesosphere, whereas the term "upper atmosphere" designates the thermosphere and above. The troposphere can be considered as well-mixed due to convection, whereas the temperature inversion causes a stable stratification in the stratosphere, where convection and vertical exchange is inhibited. The pressure in the atmosphere decreases approximately exponentially with a scale height (the altitude where pressure has dropped by 1/e) of roughly 7 km and is commonly used as a vertical coordinate. As a rule of thumb, pressure drops approximately by one magnitude every 15 km.

The Brewer-Dobson circulation (in the following abbreviated BDC) is the meridional circulation of air in the stratosphere and mesosphere and is named after its two discoverers Brewer and Dobson, who analysed water vapour, ozone and temperature distributions in the stratosphere. The first hypothesis of such a circulation was formu-

lated by Dobson et al. [1929]. The major part of ozone was expected to be produced in the tropics due to enhanced insolation. However, observations yielded high concentrations in the Arctic and low concentrations in the tropics. Thus, Dobson et al. [1929] proposed a "slow poleward drift in the highest atmosphere" accompanied with a "slow descent of air near the Pole".

Brewer [1949] noticed that the dryness of the stratosphere could only be explained by the extreme low temperatures at the tropical tropopause and postulated that stratospheric air has its origin in the troposphere and enters the stratosphere through the extremely cold tropopause at the equator. Thus, he proposed a slow circulation of air which transports air into the stratosphere in the tropics, moves air poleward in the stratosphere which, in turn, descends again into the troposphere at higher latitudes. Brewer [1949] stated that such a circulation could also transport ozone from the tropics to high latitudes. This way the proposed circulation could additionally explain the high ozone values observed in these regions corroborating the original hypothesis of Dobson.

Complementarily Dobson [1956] argued that the slightly steeper gradient of water vapour found in the stratosphere as compared to the troposphere in midlatitudes could be explained by a slow sinking of very dry air from altitudes above. The great difference in the gradients of ozone and water vapour was also a hint of subsidence of ozone-rich air from above. This descent of air into the troposphere in midlatitudes would have to be compensated by a flow of air from the troposphere into the stratosphere which, taking the dryness of stratospheric air into account, could only take place in the tropics.

Combining the findings of Brewer and Dobson, the idea of the circulation in the stratosphere, with rising air in the tropics, meridional transport to higher latitudes, and subsequent subsidence in these regions was born.

Until today the picture of the BDC has become more complex and has been extended. Birner and Bönisch [2011] introduced a second branch of the BDC, also called "shallow branch" or "secondary circulation" between pressures of 100 and 70 hPa ($\approx$ 16-19 km altitude), which transports air from the tropical tropopause into the lowermost stratosphere of higher latitudes, while the original circulation introduced by Brewer and Dobson has been termed "deep branch" (between 70 and 1 hPa $\approx$ 45 km). The two branches were discussed e.g. in Birner and Bönisch [2011]. In addition, the so-called overturning circulation transports air from the summer pole into the mesosphere and again downwelling at the winter pole.

The BDC is very important for the budget of ozone and its distribution in the stratosphere. Ozone is probably the most important trace gas in the stratosphere,

protecting us from the harmful solar UV radiation. The BDC transports also ozone-depleting substances such as CFCs, greenhouse gases like water, carbon dioxide or methane and also any kind of pollutants into the stratosphere.

While it is widely accepted that climate change with enhanced greenhouse-gas abundances leads to a warming of the troposphere and a cooling of the stratosphere, the secondary effects, in particular on the BDC, are still an issue of current research [Butchart, 2014]. A changing BDC will have large impact on the overall composition of the stratosphere, on the ozone budget and distribution as well as its recovery in the stratosphere [Li et al., 2009; Shepherd, 2008] and on the lifetimes of ozone-depleting substances such as CFCs [Butchart and Scaife, 2001; Douglass et al., 2008] and greenhouse gases like methane and N_2O [Butchart and Scaife, 2001]. A change in the lifetime of these gases will in turn influence the recovery of ozone in the polar regions and climate change via a modified radiative forcing due to change in the abundances and distributions of the greenhouse gases, respectively. As air descends back into the troposphere via the downwelling branch of the BDC it can even impact air quality at the surface. As these issues are evolving towards major concerns in this century, monitoring of any changes in the BDC is therefore essential.

The mean age of air (AoA), which is the average transit time of an air parcel from the entry point of the stratosphere, the tropical tropopause, to a place in the stratosphere, has become a measure for the strength of the BDC in particular for observational analysis [Hall and Plumb, 1994; Waugh and Hall, 2002], and can be derived from the analysis of trace gases like CO_2 and SF_6. The mean age of air comprises both information on the speed of the advection and the amount of mixing and stirring exerted on the air parcel. In model studies the strength of the BDC is often also quantified by the velocity of tropical upwelling at 70 hPa. A faster BDC corresponds to shorter transit times and therefore to younger air. Austin and Li [2006] found a linear relationship between 1/age and tropical upwelling in the stratosphere.

Modern general circulation models (GCMs) and chemistry–climate models (CCMs) consistently simulate an acceleration of the BDC in a greenhouse-gas-induced changing climate [Austin and Li, 2006; Bunzel and Schmidt, 2013; Butchart and Scaife, 2001; Butchart et al., 2006, 2010; Calvo and Garcia, 2009; Garcia and Randel, 2008; Li et al., 2008; McLandress and Shepherd, 2009; Oberländer et al., 2013; Okamoto et al., 2011; Rind et al., 1990] and therefore predict negative mean age trends throughout the stratosphere [Butchart et al., 2010; Garcia and Randel, 2008]. So far, however, this expected speeding up of the BDC has not been confirmed by observations. Engel et al. [2009] provided a 30-year record of mean age of air derived from CO_2 and SF_6 balloon-

borne measurements which showed a slight but insignificant increase of mean age over the years 1975–2005 for northern midlatitudes, which would indicate a decelerated BDC. Bönisch et al. [2011] reported an acceleration of the shallow branch of the BDC for the time period 1979–2009, while they found an unchanged deep branch. Diallo et al. [2012] investigated the age of stratospheric air in the ERA-Interim reanalysis over the period 1989–2010 and stated that the shallow and the deep branch of the BDC may evolve differently. They found a negative and significant age of air trend in the lower stratosphere and a positive but insignificant trend in the middle stratosphere. Stiller et al. [2008, 2012] provided the first global data set on age of air derived from satellite SF_6 measurements. In their paper MIPAS-ENVISAT level 1b spectra of versions 3 and 4 were used to retrieve vertical profiles of SF_6 distributed over the whole globe for the time period September 2002 to January 2010. Monthly zonal means were converted into mean age of air, from which decadal trends were inferred for latitude and altitude bins.

The derived age of air trends by Stiller et al. [2012] were found to be spatially inhomogeneous with regions of increasing mean age of air and regions of decreasing age of air. The non-homogeneity of trends was also reported by Monge-Sanz et al. [2013], who also found a significant increasing trend in the mean age of air over northern midlatitudes in a multiannual chemistry transport model (CTM) simulation driven by ERA-Interim winds over the period 1990–2009 and confirmed the measurements by Stiller et al. [2012] and Engel et al. [2009]. In their model study they already noticed a hemispheric asymmetry, which was also later found by Mahieu et al. [2014] with SLIMCAT model calculations. Ploeger et al. [2015b] confirmed this hemispheric asymmetry with calculations of the CLaMS model, which is also a CTM driven by ERA-Interim data, and found positive trends in the Northern Hemisphere and negative trends in the Southern Hemisphere for the time period 2002–2012.

The work presented here is a continuation of the work of Stiller et al. [2012]. An extended and improved SF_6 data set is provided on the basis of a newly calibrated version of MIPAS-ENVISAT level 1b spectra (version 5, ESA data version 5.02/5.06). This new global SF_6 data set for the first time covers the total MIPAS period from July 2002 to April 2012 and provides a global satellite-based study of AoA over approximately the first decade of this century.

This thesis is organised as follows: First the basics of stratospheric transport are introduced in Chapter 2. The characteristics of the MIPAS instrument are presented in Chapter 3. Chapter 4 describes the fundamentals of remote sensing in the atmosphere and retrieving trace gases. The improvements on the retrieval setup are discussed in

Chapter 5. The characteristics and morphology of the new global SF_6 data set and the resulting new age of air data set are assessed in Chapter 6. Subsequently in Chapter 7 the new MIPAS SF_6 data were validated with balloon-borne in-situ measurements and measurements from the Atmospheric Chemistry Experiment (ACE-FTS), which is another renowned satellite instrument, and the new AoA data are compared with earlier airborne AoA measurements from the 1990s. Then, in Chapter 8, the temporal analysis of AoA is carried out and the calculated decadal MIPAS AoA trends are presented, which reflect the main part of this thesis, and are compared with previous findings. Applying the same methods as in the case of MIPAS data, it was tried to infer AoA trends also from ACE-FTS SF_6 data and from simulated SF_6 values by the Karlsruhe Simulation Model of the Middle Atmosphere (KASIMA). These results as well as AoA trends calculated with the CLaMS model are presented in Chapter 9 and compared to MIPAS AoA trends. Finally, in Chapter 10, results of this thesis are summarised and lessons learned about the variability of AoA are presented. Conclusions towards possible changes of the BDC are drawn.

Parts of the results of this investigation have been already published in Haenel et al. [2015]. Several parts of this article are included in different sections of this thesis.

Chapter 2

The Brewer-Dobson Circulation

2.1 Stratospheric winds and quasi-biennial oscillation

In the stratosphere and mesosphere the dominating mean zonal winds in most parts above 20 km are eastward winds (westerlies) in winter and westward winds (easterlies) in summer. They reach maximum wind speeds of 60-75 m/s at about 70 km altitude [Brasseur and Solomon, 2005]. The zonal stratospheric winds are described as thermal winds: In the summer hemisphere the polar stratosphere is relatively warm compared to the cold tropical tropopause and lower tropical stratosphere. This temperature gradient leads to a strong westward flow (easterly wind). Contrary to that, in the winter hemisphere the meridional temperature gradient is reversed (the polar stratosphere is colder than the tropics) resulting in westerlies [Roedel, 2000].

In the lower stratosphere two jet streams, called subtropical jets, are centered at 30°-40° N/S latitude and are particularly strong in winter and weak in summer.

The polar vortex is a strong westerly wind regime in the winter polar stratosphere and leads to isolation of the polar stratosphere from lower latitudes during winter, which is most pronounced in the Southern Hemisphere.

Alternating lower stratospheric equatorial zonal winds (between westerlies and easterlies) with a period of varying from 22 to 34 months (28 months on average) are referred to as the quasi-biennial oscillation (QBO). The QBO induces a secondary meridional oscillation which modulates the strengths of the BDC and also a shift of the subtropical mixing barriers [Baldwin et al., 2001].

2.2 Atmospheric waves

Atmospheric waves can be classified according to their different restoring forces, which are necessary for the existence of the waves: Rossby or planetary waves experience their restoring force via the Coriolis force, which varies with latitude, and therefore resist horizontal displacements.

Waves which exhibit their restoring mechanism by the buoyancy force in a stable atmosphere are called gravity waves.

Quasi-stationary Rossby waves that propagate vertically are the predominant eddy motions (departure from zonal means) in the stratosphere [Holton, 2004]. However, a requirement of vertical propagation of these stationary waves in the stratosphere, is the presence of westerly winds weaker than a critical value depending on the horizontal scale of the waves [Holton, 2004]. This criterion is also called Charney-Drazin criterion. Therefore, upward propagation of waves in the stratosphere is mainly confined to the winter hemisphere.

Wave breaking can occur, when waves reach altitudes where non-linear effects become important. This leads to smaller scale motions and to irreversible mixing.

2.3 General description

A state-of-the-art schematic picture of the BDC in the latitude-altitude plane is shown in Figure 2.1 taken from Bönisch et al. [2011] and reflects the 3 different branches of the BDC: Air enters the stratosphere through the tropical tropopause (blue line) and is transported to higher latitudes by the shallow branch. The other part of the air rises in the tropics in the so-called "tropical pipe" [Plumb, 1996] and is transported to higher latitudes by the deep branch. The circulation in the mesosphere transports air from the summer to the winter pole. The BDC includes both net mass transport, also referred to as residual circulation (depicted as the thick white arrows), and two-way mixing (indicated by the wavy orange arrows). Transport and mixing barriers are marked by the thick green lines and represent the subtropical mixing barrier, the tropical pipe, and the edge of the polar vortex.

Both residual circulation and mixing are induced by breaking of atmospheric waves. The mechanism for the driving of the meridional circulation can be qualitatively understood as follows [Holton et al., 1995]:

Rossby waves always propagate with a smaller velocity than the mean flow, so in the reference frame of the mean flow they propagate westward. If the wave dissipates

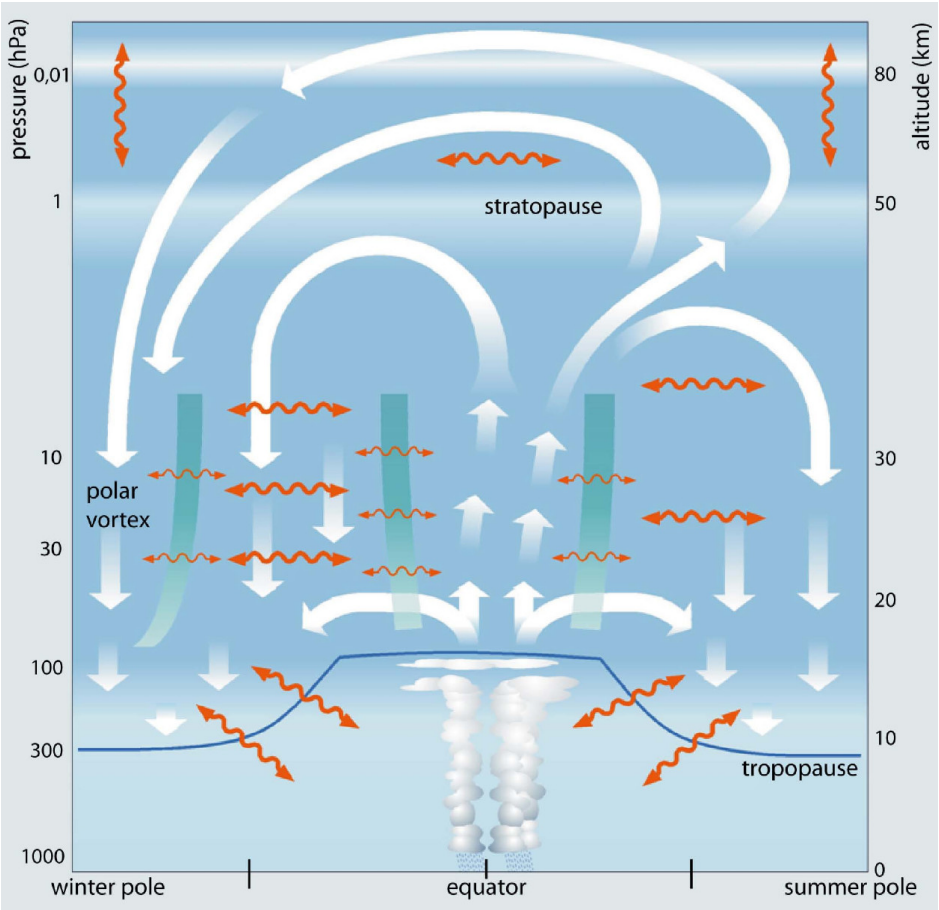

Figure 2.1: Schematic picture of the Brewer-Dobson circulation (BDC) taken from Bönisch et al. [2011] (CC BY 3.0 License): White thick arrows represent the different branches of the BDC. Mixing processes are indicated as wavy orange arrows, while mixing and transport barriers are marked as thick green lines.

due to non-linear processes it exerts a westward zonal force on the mean flow. This westward zonal force is balanced in geostrophic approximation by an eastward Coriolis force, resulting in a poleward flow [Roedel, 2000]. Conserving continuity, air rises in the tropics and descends back at higher latitudes. The up- and downward-branches of the residual circulation cross isentropes which means that the motion is diabatic with supply or removal of radiation energy [Roedel, 2000]. This results in departure of stratospheric temperatures from radiative equilibrium. The dissipating waves deposit the momentum required to conserve angular momentum of a poleward flow. The discovery of this mechanism reconciled the original concerns of Brewer and Dobson that a poleward flow would violate the conservation of angular momentum.

The subtropical jets inhibit wave propagation into the tropical pipe, and therefore mixing, which is also induced by the wave breaking, is strongly suppressed in this

region. Contrary to that, stirring by planetary waves occurs mainly in midlatitudes during wintertime, also called the "surf zone".

The mesospheric branch of the BDC is driven by the same mechanism, but the wave drag on the mean flow is primarily caused by buoyancy or gravity waves and can be eastward and westward. In the summer hemisphere easterlies filter out the upward propagating gravity waves, such that an eastward drag remains resulting in an equatorward flow, while in the winter hemisphere westerlies favor a westward drag leading to a poleward flow. The resulting overall transport in the mesosphere is therefore from the summer to the winter pole [Butchart, 2014].

The meridional velocity of the BDC is about 10 km/day, the vertical is about 100 m/day [Rosenlof, 1995] which is in the order of 1 mm/s. The BDC is 3 times stronger in the Northern Hemisphere according to Rosenlof [1995] and is weak in the summer hemisphere. Model studies suggest, that the two branches of the BDC transport almost the same mass, but have different seasonalities [e.g. Konopka et al., 2015].

2.4 The Age of Air concept

Stratospheric air originates from the troposphere and enters the stratosphere through the tropical tropopause [e.g. see Holton, 1990]. One can therefore define the "age" of a stratospheric air parcel as the time lag since it has left the tropical tropopause. The "age of stratospheric air" thus is a quantity to characterise the intensity of the Brewer-Dobson circulation. Because of mixing an air parcel does not conserve its composition along its way. It is rather composed of an infinitesimal number of irreducible fluid elements with each having their individual transport paths and transit times [Hall and Plumb, 1994]. Instead of a single age of an air parcel there exists only a statistical distribution G over transit times, which is called the "age spectrum" [Hall and Plumb, 1994; Kida, 1983]. So when speaking of the age of an air parcel, only the mean age Γ, the first moment of the age spectrum, is a reasonable measurable quantity:

$$\Gamma(r, \Omega) = \int_0^\infty t \cdot G(r, \Omega, t) dt \tag{2.1}$$

with

$$\int_0^\infty G(r, \Omega, t) dt = 1 \tag{2.2}$$

and Ω being the region of the tropical tropopause.

The time lag of an air parcel can be unambiguously inferred by measuring tracers with negligible stratospheric sources and sinks and whose tropospheric mixing ratios are increasing or decreasing monotonically with time. The time lag between the time associated with the mixing ratio observed in the stratosphere and the time when the observed mixing ratio was observed at the tropical tropopause can approximate the age. It will be shown later that only in the case of trace gases with a linear tropospheric growth, the measured time lag is precisely equal to the mean age of the observed air parcel. Such tracers are also called "chronological tracers" or "clock tracers". CO_2 and SF_6 meet these requirements fairly well and have been used in various studies (see Waugh and Hall [2002] and references therein). In this work SF_6 measurements are used to infer the mean age of stratospheric air. The tropospheric variation of SF_6 was approximately linear over the considered time scale (see Section 6.2).

In general the mixing ratio η of a conserved tracer has to satisfy the continuity equation:

$$\frac{\partial \eta}{\partial t} + L(\eta) = 0 \tag{2.3}$$

L is the differential operator which governs the transport. The general solution η(r,t) at point r in the stratosphere is [Hall and Plumb, 1994]:

$$\eta(r,t) = \int_0^t \eta(\Omega, t-t')G(r,\Omega,t')dt' \tag{2.4}$$

where $\eta(\Omega, t-t')$ is the mixing ratio of the tracer in region Ω (in our case the tropical tropopause) at time $t-t'$. The integration is carried out over all transit times ranging from 0 to t. The function G is the Green's function, the solution of Equation 2.3 with the boundary condition $\eta(\Omega, t) = \delta(t-t_0)$, where $\delta(t)$ is the Dirac delta function [Hall and Plumb, 1994]. (For $\eta(\Omega,t)$=$\delta(t-t_0)$, Equation 2.4 simply reduces to $\eta(r,t)$=$G(r,\Omega,t-t_0)$). In other words, the function G represents the stratospheric response of a delta pulse in mixing ratio of a tracer at the tropical tropopause. It propagates mixing ratios on Ω at time $t-t'$ to the point r at time t [Waugh and Hall, 2002].

By having a closer look at Equation 2.4, one can identify the Green's function G of differential operator L with the age spectrum in Equation 2.1: In Equation 2.4 all former mixing ratios at the tropical tropopause with transit time t' weighted with the age distribution G add up to the mixing ratio at point r in the stratosphere at time t. Identifying the age spectrum with the response of the system to an initial delta pulse in terms of the Green's function G provides a possibility to assess the age spectrum,

which is not directly observable, by simulations (see Section 2.4.1). Given the age spectra and the time history of a conserved tracer on Ω, one can compute the tracer distribution and evolution throughout the stratosphere. Conversely, information of the age spectrum can be obtained from tracer observations [Waugh and Hall, 2002].

In case of G being the delta function $G = \delta(t - t_0)$ the mean age Γ is t_0 and Equation 2.4 yields $\eta(r,t) = \eta(\Omega, t - t_0)$. So the mean age is equal to the time lag and we have simple advection without any kind of mixing. To show that this relationship also holds for linearly growing tracers and any kind of age spectrum one can examine Equation 2.4 in the long-time limit. Inserting

$$\eta(\Omega, t) = \gamma t \text{ for } t > 0 \text{ and } 0 \text{ otherwise} \tag{2.5}$$

into Equation 2.4 gives [Hall and Plumb, 1994]:

$$\eta(r,t) = \int_0^t \gamma(t - t')G(r, \Omega, t')dt' \tag{2.6}$$

$$= \eta(\Omega, t) \int_0^t G(r, \Omega, t')dt' \tag{2.7}$$

$$-\gamma \int_0^t t'G(r, \Omega, t')dt' \tag{2.8}$$

As t approaches infinity the two integrals in Equation 2.7 and 2.8 reduce to 2.2 and 2.1 and the mixing ratio of a linear growing tracer at point r and time t simplifies to:

$$\eta(r,t) = \eta(\Omega, t) - \gamma\Gamma = \eta(\Omega, t - \Gamma) \tag{2.9}$$

Such a limit is valid for t greater than the width of the age spectrum or more precisely greater than the time where the age spectrum asymptotically approaches zero [Hall and Plumb, 1994].

To illustrate the discussed formalism with a simple model and to provide an explicit Green's function, Hall and Plumb [1994] selected a continuity equation with a differential operator which describes one-dimensional mass-weighted diffusion with uniform and constant coefficients:

$$\rho\frac{\partial\eta(z,t)}{\partial t} = K\frac{\partial}{\partial z}(\rho\frac{\partial\eta(z,t)}{\partial z}) \tag{2.10}$$

where $\rho = \rho_0 e^{-z/H}$ is the density of air (with scale height H) and K a constant diffusion coefficient.

The age spectrum is the Green's function of this system, which can be solved analytically [Hall and Plumb, 1994]:

$$G(z,t) = \frac{z}{2\sqrt{\pi K t^3}} \exp\left[\frac{z}{2H} - \frac{Kt}{4H^2} - \frac{z^2}{4Kt}\right] \tag{2.11}$$

The mean age of this system is given by Equation 2.1, and the integration yields:

$$\Gamma = \frac{H}{K} z \tag{2.12}$$

This means the mean age increases linearly with distance from the source. Even though this is just a simple model, studies of Hall and Plumb [1994] have shown, that simulating the age spectrum using an initial pulse at the source region with a General Circulation Model (GCM) leads to results which are qualitatively similar to the age spectra described by Equation 2.11 for the one-dimensional mass-weighted diffusive system.

In general the shape of the age spectrum depends on the relative rates of advection and mixing. Waugh and Hall [2002] upgraded this one-dimensional model by adding additional advective motion with velocity u. The resulting Green's function is:

$$G(\Gamma, \Delta, t) = \frac{1}{2\Delta\sqrt{\pi t'^3}} \exp\left[\frac{-\Gamma^2(t'-1)^2}{4\Delta^2 t'}\right] \tag{2.13}$$

where $\Gamma = z/u$, $\Delta = \sqrt{Kz/u^3}$ and $t' = t/\Gamma$. Distribution of such a form are known as inverse Gaussian distributions or Wald functions. For small width Δ transport is dominated by advection and the age spectrum is narrow, while for increasing Δ the spectrum broadens because of accumulated diffusion [Waugh and Hall, 2002]. By comparing the Green's functions 2.11 and 2.13 it can be seen that the time dependence is similar due to one-dimensional diffusion in both models, but the z dependence varies with additional terms of the ratio of diffusion to advection. With the substitution $u = K/H$ in Equation 2.13 Equation 2.11 can be obtained returning to one-dimensional mass-weighted diffusion without advection. However, as stated in Waugh and Hall [2002], the global stratosphere is poorly represented by a one-dimensional model. Nevertheless the age spectra calculated from two-dimensional and three-dimensional models exhibit similar characteristics as the one-dimensional age spectra represented by Equations 2.11 and 2.13 as shown in Waugh and Hall [2002]. The spectra are asymmetric with a peak of

varying width and a long tail towards older ages. In the lower tropical stratosphere the spectra are most narrow and peaked at earliest transit times, while they become broad and shifted to longer transit times elsewhere in the stratosphere.

A one-dimensional age spectrum described by Equation 2.13 can be fitted to experimental results as done by Andrews et al. [1999] in the case of CO_2 measurements. In a later study, Andrews et al. [2001b] used a bimodal age spectrum for better fitting CO_2 data in midlatitudes, where the younger, narrow peak was identified with quasi-horizontal wave mixing and the older, broader peak with "up-and-over" transport via the mean meridional circulation.

Also periodic and exponentially growing tracers can be used to infer the age of air [see Hall and Plumb, 1994; Waugh and Hall, 2002]. The described methodology can be extended to tracers which are not stable, too. Even though SF_6 is stable within the stratosphere it is depleted in the mesosphere. This mesospheric loss can cause an overestimation of the mean age in the polar stratosphere where intrusion of mesospheric air is observed (see Section 6.3).

2.4.1 Assessment of age spectra

This study focuses on the analysis of the mean age of air to study the variation of stratospheric transport. However, the full information of stratospheric transport is contained in the age spectrum, which can only be constrained by observations, assuming an analytical function as the age spectrum, such as the Wald function [see e.g. Bönisch et al., 2009; Schoeberl et al., 2005].

The "real" shape of the age spectrum cannot be derived directly from measurements, but it can be simulated in models. As stated above the age spectrum can be identified with the Green's function and is therefore equal to the stratospheric response to a delta pulse at the tropical tropopause. The "pulse tracer" method uses this principle by releasing a pulse of a conserved tracer at the entry region of the stratosphere or in the boundary layer in the model and recording the time evolution of the tracer's mixing ratio at some point in the stratosphere. This product is called the "boundary impulse response" (BIR) [Haine et al., 2008] and is only equivalent to the age spectrum if the atmospheric flow is stationary. However, to study the seasonal and interannual variation of stratospheric transport this assumption cannot be used. In general G is not only a function of the transit time τ, but a function of the so-called "field time" when the tracer mixing ratio is measured in the stratosphere, and the so-called "source time" $t' = t - \tau$ when the tracer had last contact with the source region Ω:

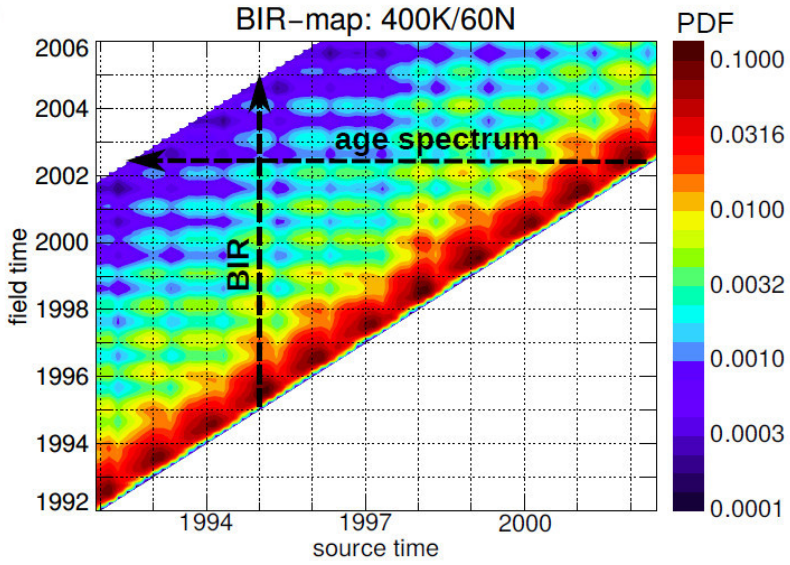

Figure 2.2: Example of a boundary propagator map from the CLaMS model at a potential temperature of 400 K and at 60° N (figure from Ploeger and Birner [2016], CC BY 3.0 License).

$$\eta(r,t) = \int_0^\infty \eta(\Omega, t-\tau) G(r,t|\Omega,t-\tau) d\tau \tag{2.14}$$

If a tracer is now released in Ω at source time $t' = t'_0$ then $\eta(\Omega, t') = \delta(t' - t'_0)$ and Equation 2.14 yields (with $t' = t - \tau$; [Ploeger and Birner, 2016]):

$$\eta(r, \tau + t') = \int_{-\infty}^{t} \delta(t' - t'_0) G(r, \tau + t'|\Omega, t') dt' \tag{2.15}$$

$$\Rightarrow \eta(r, \tau + t'_0) = G(r, \tau + t'_0|\Omega, t'_0) \tag{2.16}$$

$G(r, \tau + t'_0|\Omega, t'_0)$ is now the above mentioned BIR as a function of the transit time τ and is in general not equal to the age spectrum $G(r,t|\Omega,t-\tau)$, because even though both are functions of τ, the BIR varies in the "field time" while the age spectrum varies in the "source time" at fixed field time t. However, if the flow is steady, G, which is also called "boundary propagator", becomes time translation invariant and only a function of the transit time τ [Haine et al., 2008].

The first study found in literature which analysed the variability and seasonality of stratospheric transport by means of age spectra not relying on explicit trajectory

calculations was Li et al. [2012], who applied the method developed by Haine et al. [2008] using a set of N pulse tracers to construct the age spectra from the corresponding BIRs in the case of non-stationary flow. Figure 2.2 shows an example of the so-called "boundary propagator map" (figure taken from Ploeger and Birner [2016]), which schematically illustrates the relationship between the BIRs and the age spectra: While the BIRs are vertical slices as function of the field time, the age spectrum at a given field time is gained by a horizontal cut through the set of different BIRs [Haine et al., 2008; Li et al., 2012]. This way age spectra can be constructed, however, various pulse tracers initiated at different source times are necessary.

Ploeger and Birner [2016] further developed the construction of age spectra using a set of 60 BIRs and studied the seasonal and interannual variations in the spectra. In Section 8.2 their age spectra are used to correct the derived mean ages for the slight non-linearity of the SF_6 reference curve (see Section 6.2). Typical CLaMS age spectra in comparison to the 1-D Wald functions are shown in Figures 8.13 and 8.14.

2.4.2 Aging by mixing

As stated above, AoA comprises the combined effect of a slow residual circulation and fast quasi-horizontal mixing. Using models, the effect of both contributions on AoA can be separated. According to Ploeger et al. [2015a], using the CLaMS model, mixing locally increases AoA at low latitudes equatorwards of about 40° N/S and decreases AoA at higher latitudes, as mixing is an exchange of young air from low latitudes with old air from high latitudes.

The term "aging by mixing" has been introduced by Garny et al. [2014] and means the integrated effect of local mixing along the hypothetical transport path of the residual circulation on AoA. This contribution to AoA can be approximated by the difference between AoA and the residual circulation transit time (RCTT). The RCTT can be calculated in a model following the method of Birner and Bönisch [2011] and consists of calculating backward trajectories driven by residual mean meridional and vertical winds (v*, w*)

Garny et al. [2014] found the additional aging due to mixing to be positive almost throughout the entire stratosphere, only in the lowermost extratropical stratosphere close to the poles AoA is reduced by the integrated effect of mixing and is younger than the RCTT. These findings have been confirmed by Ploeger et al. [2015a] who carried out an exact calculation of the additional mixing term by using the integrated tracer continuity equation for AoA,

$$\Gamma(r,t) = \tau_{RCTT}(r,t) + \int_{t_0}^{t} M(r,t')dt' \tag{2.17}$$

where $\tau_{RCTT}(r,t)$ is the residual circulation transit time and M is the local mixing tendency for AoA, describing the local effects of mixing on AoA [Ploeger et al., 2015a].

In their study, Garny et al. [2014] also found changes in the "aging by mixing" to be strongly coupled to changes in the residual circulation, which means that AoA used as a diagnostics for the strength of the circulation exhibits an even amplified effect.

In the Conclusions of this thesis the effect of "aging by mixing" on the observed AoA trends will be discussed.

2.5 The tracer SF_6

Sulphur hexafluoride (SF_6) is mainly produced anthropogenically and used as an insulation gas in electrical power production. Due to the larger industrial activity the SF_6 abundance is higher in the Northern Hemisphere [Ko et al., 1993; Maiss and Levin, 1994]. SF_6 is stable in the troposphere and stratosphere and its mixing ratios are increasing almost linearly in the atmosphere. Thus, this gas meets the requirements of an ideal age tracer almost perfectly (see Section 2.4). However, SF_6 has a sink in the mesosphere. The most important removal processes are electron attachment and UV-photolysis. The electron attachment can be dissociative forming the SF_5^- anion fragment or non-dissociative forming the SF_6^- anion, which in turn reacts with H, O, O_3 and HCl [Kovács et al., 2016].

Ravishankara et al. [1993] reported an atmospheric lifetime of SF_6 of 3200 years. Reddmann et al. [2001] found a lifetime of 400 to 10000 years with the Karlsruhe Simulation Model of the Middle Atmosphere (KASIMA), depending on the assumed loss reactions and electron density. A recent model study with the Whole Atmospheric Community Climate Model (WACCM) by Kovács et al. [2016] reported a mean lifetime over a 11-year solar cycle of 1278 years, which is considerably shorter than the one derived by Ravishankara et al. [1993]. According to the formers' paper the SF_6 removal is dominated by electron attachment.

Chapter 3

MIPAS

3.1 MIPAS on ENVISAT

MIPAS (Michelson Interferometer of Passive Atmospheric Sounding) was a Fourier Transform infrared (FTIR) spectrometer aboard ENVISAT (Environmental Satellite, Fischer et al. [2000], Figure 1), which was launched in March 2002 by the European Space Agency (ESA). ENVISAT was a polar orbiting sun-synchronous satellite in an orbit of about 800 km with an inclination of the orbit of 98°. ENVISAT's task was the permanent survey of the Earth's climate, the ocean, the land surfaces and the Earth's ecosystem in general. The mission of ENVISAT was planned with a lifetime of 5 years, but ENVISAT kept on sending data until April 2012, when ESA lost contact to the satellite.

MIPAS was designed for the detection of mid-infrared limb emission spectra in the middle and upper atmosphere. It observed a wide spectral interval ranging from 4.15 μm to 14.6 μm (685-2410 cm^{-1}) with high spectral resolution [Fischer et al., 2008]. In this part of the atmospheric spectrum a wide variety of trace gases have absorption lines and atmospheric signals are generally higher than in other parts of the spectrum because the Planck function maximises at about 10 μm for atmospheric temperatures. The MIPAS instrument made use of the principle, that trace gases have characteristic emission and absorption lines, represented by their absorption coefficients (see Section 4.1.1), which are unambiguous "fingerprints" of the particular trace gases. The atmospheric spectra were inverted into vertical profiles of atmospheric pressure, temperature and volume mixing ratios (vmrs) of at least 30 trace constituents. This allows studies of stratospheric chemistry and dynamics, stratosphere-troposphere exchange, chemistry and physics of the upper troposphere, chemistry and physics of the upper atmosphere, as well as climatologies and improvement of weather forecasting. A par-

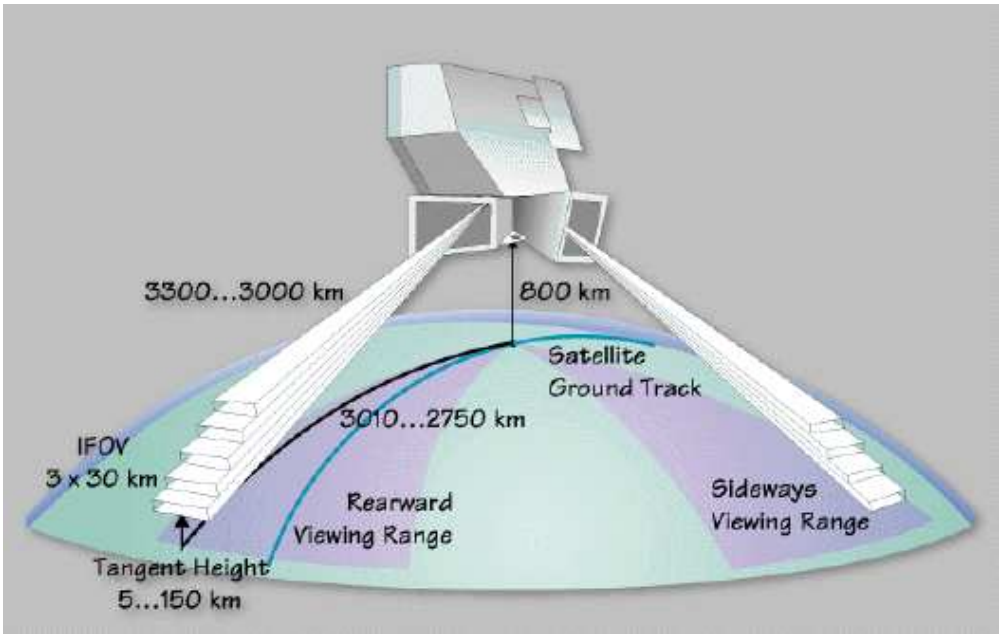

Figure 3.1: Geometry of MIPAS (source: ESA)

ticular advantage of MIPAS was that, as a limb emission instrument as opposed to a solar occultation instrument, it could measure globally and during day and night at a local time of 10 am and 10 pm, due to the sun-synchronous orbit of ENVISAT.

3.2 Viewing geometry of MIPAS

MIPAS was a limb sounder, i.e. it scanned across the horizon. The line of sight penetrated the atmosphere tangentially to the Earth surface down to a minimum altitude, called tangent altitude, and then due to the Earth curvature rises again towards space [Fischer et al., 2008]. MIPAS could measure trace gas emissions along the line of sight. Because of the long optical path through the atmospheric layers, MIPAS was able to detect trace gases with very low mixing ratios. The layer directly above the tangent altitude is the layer in which the line of sight covers the longest distance. The spectrum of radiation along the line of sight therefore contains most information of this layer, but also information of the layers above.

MIPAS was capable of looking in two directions (see Figure 3.1): To the rear, opposite to the flight direction (the normal case, used in this study), and sideways orthogonal to the flight direction to observe special events, like volcanic eruptions. MIPAS scanned the atmosphere at different elevation angles with different tangent

altitudes, with which vertical information is gained. MIPAS could observe the atmosphere in the altitude range from 5 to 160 km with minimum and maximum tangent altitude increments of 1 and 8 km, respectively [Fischer et al., 2008]. The MIPAS instrument had a specific angle of aperture, i.e. it did not only collect radiation along the line of sight, but from a certain solid angle. This led to an instantaneous field of view (IFOV), which covered 3 km in the vertical and 30 km in the horizontal at the tangent altitude. The horizontal sampling was about 510 km along track in the full-resolution period (see Section 3.3) and about 410 km in the reduced-resolution period (see Section 3.3). The tangent point projected at the surface of the Earth is called geolocation.

3.3 Instrument

The incoming atmospheric limb radiation was reflected at an azimuth and an elevation scan mirror and then conducted via a telescope into a Michelson-type Interferometer with two input and two output ports (see Figure 3.2). The azimuth scan mirror allowed to select the line of sight within the two field-of-view regions, to correct for the inclination of the orbit so that a pole to pole coverage was possible, and also to direct radiation from an internal blackbody into the interferometer for calibration purposes. The elevation scan mirror determined the actual limb height, i.e. the tangent height of the measurement. The interferometer worked as follows: The input signal was divided by the beamsplitter and directed to two movable cube corner mirrors from where they were reflected back to the recombiner and directed to the two output ports where the signal contained the interferogram of both beams. The output signals were fed into a detector unit which was cooled down to 70 K for maximum sensitivity of the detectors and to reduce their thermal emission. At each output port the output signal was separated into four spectral channels by optical filtering and analysed by four dedicated MCT (Mercury Cadmium Telluride) detectors, each optimised for highest sensitivity in the respective spectral band [Fischer et al., 2008].

As part of the ground processing, the recorded interferograms as a function of optical path difference of the two beams were converted into spectra by a Fourier Transformation. This process, along with other steps as spectral and radiance calibration, is usually called level-1 processing.

The MIPAS instrument was able to measure in different modes dedicated to the respective interest of research, like the nominal mode, polar winter chemistry mode, upper atmosphere mode, UTLS (Upper Troposphere Lower Stratosphere) mode and

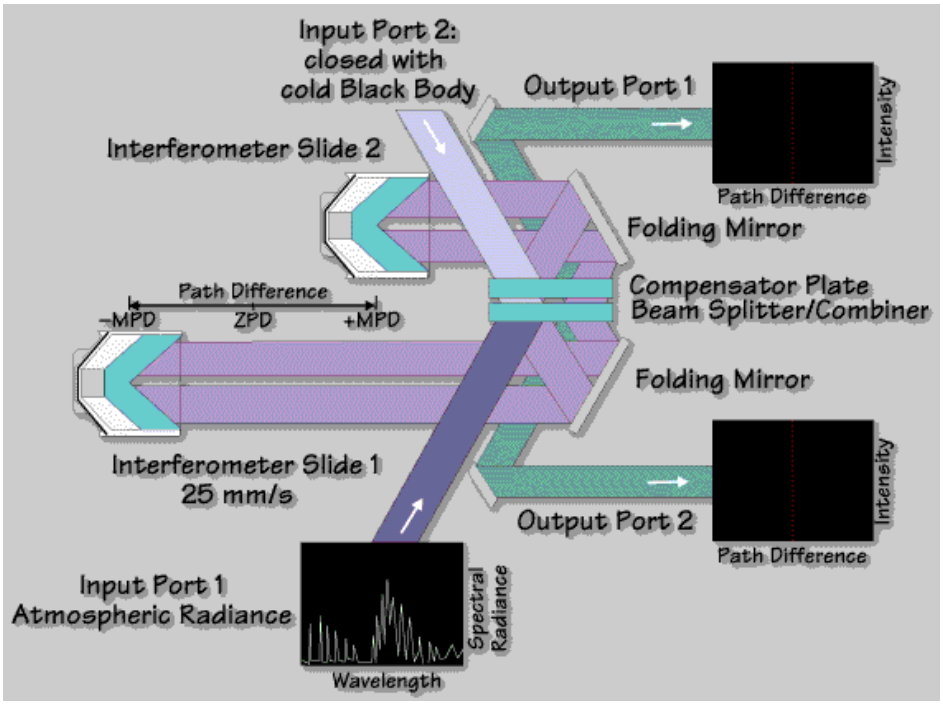

Figure 3.2: Michelson Interferometer (source: ESA)

others. For the study of this thesis, measurements of the nominal mode were used, which cover about 80% of the total measurements. Vertical coverage in this standard mode was 6 to 68 km.

In 2004 the operation of the MIPAS instrument was interrupted due to a problem with the interferometer slide. The maximum optical path difference was then reduced, implying a deterioration of the spectral resolution from 0.025 to 0.0625 cm^{-1}. The first phase of the mission (2002–2004) is usually referred to as the MIPAS full-resolution (FR) period, while the second phase (2005–2012) is called the reduced-resolution (RR) period.

At each tangent altitude one interferogram was recorded as a function of the optical path difference, which took about 4.5 s for one full-resolution spectrum. A limb scan sequence in the FR-period acquired 17 spectra at tangent altitudes between 6 and 68 km with a vertical spacing of 3 km in the lower atmosphere and a larger interval above. The total time for one limb scan was therefore about 76 s. One orbit consisted of about 72 limb scans, and with ENVISAT orbiting the Earth about 14 times per day, this resulted in about 1000 limb sequences per day.

In the RR-period the maximum optical path difference in the interferometer was reduced, which in turn reduced also the time to record one spectrum. This allowed to measure at more tangent altitudes (27 in total) with refined vertical spacing (1.5 km

up to 22 km) and also improved the along track sampling (≈410 km instead of 510 km).

3.3.1 Apodisation

A Fourier Transform spectrometer has a maximum optical path difference (max OPD). However, to resolve an ideal spectral line a considerably longer maximum OPD would be needed. Because of the limited maximum OPD of a real spectrometer, the spectral resolution is also limited to:

$$\Delta\nu = \frac{1}{2 \cdot (\text{max OPD})} \tag{3.1}$$

In the case of the MIPAS instrument, the maximum OPD amounted to 20 cm in the full resolution case, therefore the spectral resolution was $0.025\,\text{cm}^{-1}$. The finite maximum OPD of the spectrometer has also another effect: The truncation of the interferogram at the maximum OPD corresponds to a multiplication of the infinite interferogram with a rectangular function. In the wavenumber space this corresponds to a convolution of the spectrum with the sinc-function ($\frac{\sin(x)}{x}$), the Fourier Transform of a rectangular function. Thus, a spectral line appears to be broadened and exhibits several additional side maxima. In order to reduce these undesired maxima, the interferogram is multiplied with an apodisation function, which continuously fades out the interferogram towards the maximum OPD. In the case of MIPAS, the apodisation of Norton and Beer [1976] has been proved of value. This multiplication is, in turn, equivalent to a convolution with the Fourier Transform of the apodisation function in the spectral space. The spectral resolution is therefore further reduced and the spectral radiances are not independent anymore, which needs to be considered in the level-2 processing [von Clarmann, 2003] (see Section 4.2).

3.4 MIPAS processors

The MIPAS atmospheric calibrated spectra (which are called level-1b data) are provided by ESA, but need to be converted into altitude profiles of temperature, pressure and vmrs of trace gases. This procedure is called level-2 processing. ESA has installed its own level-2 processor for selected key species. However, for a more sophisticated analysis dedicated to specific research questions and in particular for the analysis of further trace gases several additional MIPAS level-2 processors have been developed. For the analysis of MIPAS SF_6 in this thesis, the MIPAS data processor developed at IMK was used [von Clarmann et al., 2003].

The Retrieval Control Program (RCP) constitutes the main part of the IMK MIPAS processor. It consists of the Radiative Transfer Model KOPRA [Stiller, 2000] and the inversion algorithm INVERS. The physical and mathematical fundamentals of these algorithms are presented in the next chapter. The application and the setup of the IMK MIPAS processor are described in Chapter 5.

Chapter 4

The retrieval scheme

4.1 Radiative transfer in the atmosphere

The irradiance or flux density is defined as the energy dE transport per time dt perpendicular through area dA in the wavenumber[1] interval ν to $\nu + d\nu$:

$$F_\nu = \frac{dE}{d\nu\, dt\, dA} \tag{4.1}$$

One can therefore define the spectral radiance I_ν as the energy dE transported per time dt through area dA in directions confined to a differential solid angle $d\Omega$ oriented at an angle Θ to the normal of dA, so that

$$F_\nu = \int_\Omega I_\nu \cos\Theta\, d\Omega \tag{4.2}$$

It follows then, that the spectral radiance or intensity I_ν is defined [Liou, 1980]:

$$I_\nu = \frac{dE}{\cos\Theta\, d\Omega\, d\nu\, dt\, dA} \tag{4.3}$$

The spectral radiance is the essential quantity measured by the MIPAS instrument and is usually specified in the units $[\frac{nW}{cm^2\, sr\, cm^{-1}}]$.

As radiation travels through the atmosphere of a distance ds, its intensity is decreased by absorption and scattering of matter

$$dI_\nu = -(k_{\nu,a} + k_{\nu,s})\rho I_\nu ds \tag{4.4}$$

[1]The wavenumber is defined as $1/\lambda$ and is usually used instead of the frequency in infrared spectroscopy.

where ρ is the number density of matter and $k_{\nu,a}$ and $k_{\nu,s}$ describe the absorption and scattering cross sections, respectively [Liou, 1980]. On the other hand, radiation is strengthened by emission by matter and by scattering of radiation into the direction of the beam.

$$dI_\nu = (j_\nu + j_{\nu,s})\rho ds \tag{4.5}$$

The emission coefficient j_ν is, by applying Kirchhoff's law and assuming local thermal thermodynamic equilibrium (LTE),

$$j_\nu = k_{\nu,a}\, B_\nu(T) \tag{4.6}$$

where

$$B_\nu(T) = \frac{2hc^2\nu^3}{exp(\frac{hc\nu}{kT}) - 1} \tag{4.7}$$

represents the Planck function. The source function coefficient due to scattering $j_{\nu,s}$ is given by [Petty, 2004]

$$j_{\nu,s} = k_{\nu,s}\frac{1}{4\pi}\int\limits_{\Omega} p(\theta,\phi,\theta',\phi')\, I_\nu(\theta',\phi')d\Omega' \tag{4.8}$$

with p being the phase function.

Thus, combining these equations, the equation of radiative transfer can be formulated:

$$\frac{dI_\nu}{ds} = -(k_{\nu,a} + k_{\nu,s})\rho I_\nu + k_{\nu,a}\,\rho B_\nu(T) + k_{\nu,s}\rho\frac{1}{4\pi}\int\limits_{\Omega} p(\Omega,\Omega')\, I_\nu(\Omega')d\Omega' \tag{4.9}$$

In the thermal infrared for $\lambda > 4\mu m$ the scattering terms can be neglected for aerosol/cloud-free situations because the Raleigh scattering cross section is proportional to $1/\lambda^4$ and the equation of radiative transfer reduces to:

$$\frac{dI_\nu}{k_{\nu,a}\rho\, ds} = -I_\nu + B_\nu(T) \tag{4.10}$$

This equation is also called Schwarzschild-Equation. By introducing the optical thickness τ

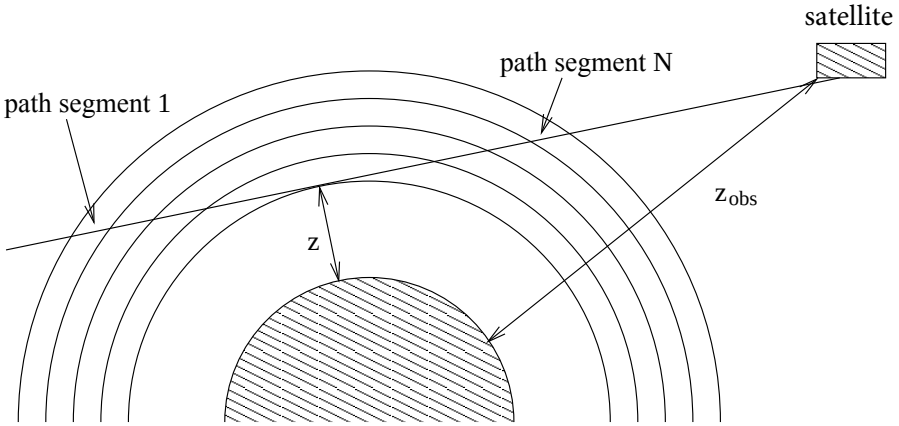

Figure 4.1: Limb geometry of MIPAS (figure adapted from Steck [2000]).

$$\tau_\nu(s_1, s) = \int_s^{s_1} k_\nu \rho ds' \tag{4.11}$$

and applying a variable transformation, the Schwarzschild-Equation can be integrated from s_0 to s_1 [Liou, 1980]:

$$I_\nu(s_1) = I_\nu(s_0)\exp(-\tau_\nu(s_1, s_0)) + \int_{s_0}^{s_1} B_\nu(T(s))\exp(-\tau_\nu(s_1, s))k_\nu\rho ds \tag{4.12}$$

$$= I_\nu(s_0)\mathfrak{T}_\nu(s_0, s_1) + \int_{s_0}^{s_1} B_\nu(T(s))\mathfrak{T}(s, s_1)k_\nu\rho ds \tag{4.13}$$

with the transmission $\mathfrak{T}$ between s and s_1

$$\mathfrak{T}_\nu(s, s_1) = e^{-\tau_\nu(s_1, s)} \tag{4.14}$$

These basic equations of infrared radiative transfer in the atmosphere are applied to the MIPAS measurement geometry (Figure 4.1). Doing so, the continuous representations need to be replaced by discrete ones. MIPAS is a limb sounder, i.e. the observed radiation beam (line of sight) traverses the atmosphere tangentially to the Earth's surface (see Figure 4.1). The atmosphere is divided into N approximately spherical symmetric layers which are assumed to be homogeneous. The radiation detected by MIPAS at a specific tangent height z can be described as [Höpfner, 2000]:

$$I(\nu) = \sum_{i=1}^{N}[(1 - \mathfrak{T}_i(\nu))B(T_i, \nu) \prod_{k=i+1}^{N} \mathfrak{T}_k] \tag{4.15}$$

The index i denotes the path segment and $\mathfrak{T}_i(\nu)$ is the corresponding transmission of the path segment i:

$$\mathfrak{T}_i(\nu) = exp(-\sum_{g=1}^{G} k_{ig}(\nu)u_{ig}) \tag{4.16}$$

with k_{ig} being the absorption cross section and u_{ig} the column density of gas g in path segment i.

In the case where the LTE breaks down, the source term $B(T_i, \nu)$ needs to be replaced by $S(T_i, \nu)$:

$$S_\nu(T) = \frac{2hc^2\nu^3}{exp(\frac{r_1 hc\nu}{r_2 kT}) - 1} \tag{4.17}$$

where r_1 and r_2 represent the ratios of the real population to the population assuming LTE in the lower (1) and upper (2) states of the transition of the molecule. r_m can be calculated if the vibrational temperature is known [Zorn et al., 2000]

$$r_m = f_Q \exp\left(-\frac{E_{vib,m}}{k}\left(\frac{1}{T_{vib,m}} - \frac{1}{T_{kin}}\right)\right) \tag{4.18}$$

with f_Q being a correction factor (for more details see Funke and Höpfner [2000]).

Using Equations 4.15 and 4.16 the expected radiation reaching the detector of the MIPAS instrument can be calculated, if vertical profiles of gases g are known. This is called a forward model. But in case of remote sensing with the MIPAS satellite instrument, the radiances of a specific tangent height are measured, while the vertical profiles of the gases are unknown. The aim of a MIPAS measurement is to retrieve vertical profiles from measured radiances at different tangent heights and is therefore an inverse problem. The forward model described here needs to be inverted and the respective techniques are described in Section 4.2.

The forward model KOPRA [Stiller, 2000] used with the IMK MIPAS processor is by far more complex then its fundamental principles described here, e.g. it further includes also refraction and optionally also scattering in the atmosphere. The radiance recorded by the instrument, which is the integral of radiances over the field of view (see Section 3.2), is numerically approximated by a weighted sum over a number of infinitesimally narrow ray paths, so-called "pencil beams" in the forward model.

4.1.1 Absorption cross sections and pseudolines

The forward calculation requires the knowledge of the absorption cross sections of all relevant gases, which reflect the specific emission spectra of the analysed trace gases, the specific "signature" of the gases. The spectra are composed of emission lines of molecular transitions. In the case of mid-infrared spectroscopy, these transitions are transitions between different vibrational-rotational states of the molecules. The energy levels and probabilities of such transitions are governed by Quantum Mechanics. However, for complex molecules, it is not possible to calculate the exact energy levels and probabilities and therefore the emission lines. Thus, the positions, relative intensities and widths of these lines are determined by highly resolved laboratory spectra [von Clarmann, 2003], which were measured at a particular temperature and pressure. These spectra are adapted to the actual atmospheric conditions (temperature and pressure), i.e. the intensity is adjusted to the atmospheric temperature and the line shape is calculated for the respective temperature and pressure using models. The line shape, for instance, is approximated by the Voigt function, which considers both, pressure and Doppler-broadening of the emission line.

For heavy and complex molecules like SF_6 it is often not possible to resolve individual lines by the spectrometer and only the coarse structure of the bands can be observed. Therefore a line-by-line consideration in the forward model is not possible. Instead, the forward model uses absorption cross sections measured in the laboratory at particular pressures and temperatures, which only reflect the coarse shape of the superposition of the not resolvable emission lines. These coarse cross sections are interpolated to the respective atmospheric condition [von Clarmann, 2003]. For the analysis of this thesis the cross sections of SF_6 from the spectroscopic database HITRAN2000 [Rothman et al., 2003] were used (shown in Figure 5.1), which relies on spectroscopic laboratory measurements of Varanasi et al. [1994].

Another approach to model the emission of heavy molecules is the application of "pseudolines". These artificial lines at arbitrary positions do not represent transitions of molecules. Instead, their line-widths and intensities are fitted to the laboratory spectra such that the pseudoline list allows to simulate the measured spectra. However, a trial to use pseudolines instead of cross sections did not lead to a better description of SF_6 (Section 5.7).

4.2 Retrieval theory

If the n-dimensional vector $\mathbf{x}$ denotes the atmospheric state, which should be retrieved from measurements contained in the m-dimensional vector $\mathbf{y}$ and using a forward model (see last section) $\mathbf{f}$, then, in absence of systematic measurement errors, the relation between these quantities can be described as

$$\mathbf{y} = \mathbf{f}(\mathbf{x}, \mathbf{b}) + \boldsymbol{\epsilon} \tag{4.19}$$

where the vector $\mathbf{b}$ denotes additional parameters, which are kept constant during the inversion and $\boldsymbol{\epsilon}$ contains the noise of the measurements $\mathbf{y}$. In the case of the MIPAS instrument, the measurement vector $\mathbf{y}$ consists of a sequence of infrared radiance spectra measured at different tangent heights which in turn consist of measured radiances at different wavenumber sampling points. The unknown quantity to be determined, is the atmospheric profile consisting of volume mixing ratios (vmrs) at different altitudes of the explored trace gas (in this case SF_6). The additional parameters condensed in the vector $\mathbf{b}$ are, among others, atmospheric profiles of additional gases contributing to the measured spectra, which are kept constant during the inversion, but have to be considered by the forward calculation in order to reproduce fairly well the measured spectra.

The forward model $\mathbf{f}$ is usually non-linear, but can be linearised

$$\mathbf{y} \approx \mathbf{f}(\mathbf{x_0}, \mathbf{b}) + \mathbf{K}(\mathbf{x} - \mathbf{x_0}) + \boldsymbol{\epsilon} \tag{4.20}$$

where $\mathbf{K}$ represents the Jacobian matrix $\mathbf{K} = \frac{\partial \mathbf{f}}{\partial \mathbf{x}}$.

In order to solve Equation 4.20 for the atmospheric state $\mathbf{x}$, $\mathbf{K}$ needs to be inverted, which is, however, only possible if $\mathbf{K}$ is quadratic (m=n) and not singular. In general m is greater than n, and the inverse problem is overdetermined. Therefore the least squares fit method is applied, which minimises the quadratic norm of the residual $\mathbf{y} - \mathbf{f}(\mathbf{x})$ weighted with the inverse covariance matrix $\mathbf{S_y^{-1}}$:

$$(\mathbf{y} - \mathbf{f}(\mathbf{x}))^{\mathbf{T}} \mathbf{S_y^{-1}} (\mathbf{y} - \mathbf{f}(\mathbf{x})) = \mathbf{minimum} \approx \tag{4.21}$$

$$(\mathbf{y} - \mathbf{f}(\mathbf{x_0}) - \mathbf{K}(\mathbf{x} - \mathbf{x_0}))^{\mathbf{T}} \mathbf{S_y^{-1}} (\mathbf{y} - \mathbf{f}(\mathbf{x_0}) - \mathbf{K}(\mathbf{x} - \mathbf{x_0})) = \mathbf{minimum} \tag{4.22}$$

This implies that the derivative with respect to $\mathbf{x}$ must vanish,

$$\frac{d}{d\mathbf{x}}\left((\mathbf{y}-\mathbf{f}(\mathbf{x_0})-\mathbf{K}(\mathbf{x}-\mathbf{x_0}))^{\mathbf{T}}\mathbf{S_y^{-1}}(\mathbf{y}-\mathbf{f}(\mathbf{x_0})-\mathbf{K}(\mathbf{x}-\mathbf{x_0}))\right)=0 \tag{4.23}$$

which leads to

$$\mathbf{x}=\mathbf{x_0}+(\mathbf{K^T S_y^{-1} K})^{-1}\mathbf{K^T S_y^{-1}}(\mathbf{y}-\mathbf{f}(\mathbf{x_0})) \tag{4.24}$$

However, Equation 4.24 was derived under the assumption that the forward model $\mathbf{f}$ is approximately linear. In order to reduce uncertainties, the same derivation can be done without the linearisation of the forward model, i.e. the derivative of the term $(\mathbf{y}-\mathbf{f}(\mathbf{x}))^{\mathbf{T}}\mathbf{S_y^{-1}}(\mathbf{y}-\mathbf{f}(\mathbf{x}))$ must be zero, which can be transformed to the condition:

$$\left(\frac{\partial \mathbf{f}}{\partial \mathbf{x}}\right)^{T}\mathbf{S_y^{-1}}(\mathbf{y}-\mathbf{f}(\mathbf{x}))=\mathbf{0}=\mathbf{g}(\mathbf{x}) \tag{4.25}$$

The roots of the non-linear function $\mathbf{g}(\mathbf{x})$ can be found via a Newtonian iteration:

$$\mathbf{x}_{i+1}=\mathbf{x_i}-\left(\frac{\partial \mathbf{g}}{\partial \mathbf{x}}(\mathbf{x_i})\right)^{-1}\mathbf{g}(\mathbf{x_i}) \tag{4.26}$$

$$=\mathbf{x_i}-\left[\frac{\partial^2 \mathbf{f}}{\partial \mathbf{x^2}}(\mathbf{x_i})\mathbf{S_y^{-1}}(\mathbf{y}-\mathbf{f}(\mathbf{x_i}))-\left(\frac{\partial \mathbf{f}}{\partial \mathbf{x}}(\mathbf{x_i})\right)^{\mathbf{T}}\mathbf{S_y^{-1}}\left(\frac{\partial \mathbf{f}}{\partial \mathbf{x}}(\mathbf{x_i})\right)\right]^{-1}\mathbf{g}(\mathbf{x_i}) \tag{4.27}$$

According to Rodgers [2000] the term $\frac{\partial^2 \mathbf{f}}{\partial \mathbf{x^2}}(\mathbf{x_i})\mathbf{S_y^{-1}}(\mathbf{y}-\mathbf{f}(\mathbf{x_i}))$ is small in the moderately linear case and becomes even smaller as the iteration converges, so it is neglected here,

$$\mathbf{x}_{i+1}\approx\mathbf{x_i}+\left(\mathbf{K_i^T S_y^{-1} K_i}\right)^{-1}\mathbf{K_i^T S_y^{-1}}(\mathbf{y}-\mathbf{f}(\mathbf{x_i})) \tag{4.28}$$

4.2.1 Optimal estimation

Even though for spectroscopic measurements in the atmosphere the inverse problem is usually overdetermined, the inverse problem can still be ill-posed, when e.g. measurements are not independent from each other. In this case the information contained in the measurements is not sufficient to unambiguously solve the inverse problem according to Equations 4.24 and 4.28. Thus, additional information on the atmospheric state $\mathbf{x}$ is needed, which is called a priori information.

Using the Theorem of Bayes both measurements and a priori information can be

combined to retrieve the atmospheric state as: If $P(\mathbf{x}|\mathbf{y})$ denotes the probability that the atmospheric state $\mathbf{x}$ exists, under the condition that $\mathbf{y}$ is measured, than

$$P(\mathbf{x}|\mathbf{y}) = \frac{\mathbf{P}(\mathbf{y}|\mathbf{x}) \cdot \mathbf{P}(\mathbf{x})}{\mathbf{P}(\mathbf{y})} \tag{4.29}$$

where $P(\mathbf{y}|\mathbf{x})$ denotes the probability that y is measured under the condition that the atmospheric state $\mathbf{x}$ is given by the multivariate Gaussian distribution, which is the same as in the case of the least squares method

$$P(\mathbf{y}|\mathbf{x}) = \frac{\mathbf{1}}{\sqrt{\mathbf{2}\pi^{\mathbf{m}}|\mathbf{S_y}|^{\mathbf{-1}}}} \exp(-\frac{\mathbf{1}}{\mathbf{2}}(\mathbf{y}-\mathbf{f}(\mathbf{x}))^{\mathbf{T}}\mathbf{S_y^{-1}}(\mathbf{y}-\mathbf{f}(\mathbf{x}))) \tag{4.30}$$

and $P(\mathbf{x})$ describes the distribution of the a priori information which is assumed to be Gaussian around the "a priori state" $\mathbf{x_a}$ with uncertainties condensed in the a priori covariance matrix $\mathbf{S_a}$.

$$P(\mathbf{x}) = \frac{\mathbf{1}}{\sqrt{\mathbf{2}\pi^{\mathbf{n}}|\mathbf{S_x}|^{\mathbf{-1}}}} \exp(-\frac{\mathbf{1}}{\mathbf{2}}(\mathbf{x}-\mathbf{x_a})^{\mathbf{T}}\mathbf{S_a^{-1}}(\mathbf{x}-\mathbf{x_a})) \tag{4.31}$$

Therefore Bayes' Theorem (Equation 4.29) yields:

$$P(\mathbf{x}|\mathbf{y}) \propto \exp(-\frac{\mathbf{1}}{\mathbf{2}}\left[(\mathbf{y}-\mathbf{f}(\mathbf{x}))^{\mathbf{T}}\mathbf{S_y^{-1}}(\mathbf{y}-\mathbf{f}(\mathbf{x})) + (\mathbf{x}-\mathbf{x_a})^{\mathbf{T}}\mathbf{S_a^{-1}}(\mathbf{x}-\mathbf{x_a})\right]) \tag{4.32}$$

This probability maximises for atmospheric state $\mathbf{x}$ where the cost function term minimises,

$$(\mathbf{y}-\mathbf{f}(\mathbf{x}))^{\mathbf{T}}\mathbf{S_y^{-1}}(\mathbf{y}-\mathbf{f}(\mathbf{x})) + (\mathbf{x}-\mathbf{x_a})^{\mathbf{T}}\mathbf{S_a^{-1}}(\mathbf{x}-\mathbf{x_a}) = \mathbf{minimum} \tag{4.33}$$

The respective state $\mathbf{x}$ can be retrieved by performing the same procedure as described for the least squares fit method above:

$$\mathbf{x} = \mathbf{x_a} + (\mathbf{K}^{\mathbf{T}}\mathbf{S_y^{-1}}\mathbf{K} + \mathbf{S_a}^{\mathbf{-1}})^{\mathbf{-1}}\mathbf{K}^{\mathbf{T}}\mathbf{S_y^{-1}}(\mathbf{y}-\mathbf{f}(\mathbf{x_0})) \tag{4.34}$$

where the a priori $\mathbf{x_a}$ was chosen as $\mathbf{x_0}$.

In the case of a non-linear forward model, the solution can be found again by Newtonian iteration:

$$\mathbf{x_{i+1}} = \mathbf{x_i} + (\mathbf{K_i}^{\mathbf{T}}\mathbf{S_y^{-1}}\mathbf{K_i} + \mathbf{S_a}^{\mathbf{-1}})^{\mathbf{-1}}\left[\mathbf{K_i}^{\mathbf{T}}\mathbf{S_y^{-1}}(\mathbf{y}-\mathbf{f}(\mathbf{x_i})) - \mathbf{S_a}^{\mathbf{-1}}(\mathbf{x_i}-\mathbf{x_a})\right] \tag{4.35}$$

This approach is called "optimal estimation" because it yields the best fit between measurements and an a priori state $\mathbf{x_a}$. In the case of retrieving trace gas profiles from atmospheric radiance spectra the a priori state $\mathbf{x_a}$ can be an expected trace gas profile, like a climatological profile. If there is not sufficient information contained in the measurements at a specific altitude, than the trace gas profile is forced towards the a priori profile.

4.2.2 The Tikhonov approach

The disadvantage of the optimal estimation approach is the dependence of the solution on the prescribed a priori state $\mathbf{x_a}$. If a climatological profile is used, then a strong deviation of the actual profile from such a mean profile might be not discovered by this technique. In addition, $\mathbf{x_a}$ and its covariance matrix $\mathbf{S_a}$ are often not known. However, in most cases additional information is needed to solve the inverse problem.

Therefore the MIPAS processor uses an approach developed by Tikhonov [1963]. Instead of forcing the profile towards an a priori state $\mathbf{x_a}$, the slope of the profile is constrained. The cost function which is minimised in this case is

$$(\mathbf{y}-\mathbf{f}(\mathbf{x}))^{\mathbf{T}}\mathbf{S_y^{-1}}(\mathbf{y}-\mathbf{f}(\mathbf{x}))+(\mathbf{x}-\mathbf{x_a})^{\mathbf{T}}\mathbf{L}^{\mathbf{T}}\gamma\mathbf{L}(\mathbf{x}-\mathbf{x_a})=\mathbf{minimum} \tag{4.36}$$

where L is defined such that

$$\mathbf{Lx}=\begin{pmatrix}1 & -1 & 0 & \cdots & 0 & 0\\ 0 & 1 & -1 & \cdots & 0 & 0\\ \vdots & \vdots & \vdots & \ddots & \vdots & \vdots\\ 0 & 0 & 0 & \cdots & 1 & -1\end{pmatrix}\begin{pmatrix}x_1\\ x_2\\ \vdots\\ x_n\end{pmatrix}=\begin{pmatrix}x_1-x_2\\ x_2-x_3\\ \vdots\\ x_{n-1}-x_n\end{pmatrix} \tag{4.37}$$

If a priori state $\mathbf{x_a}$ is chosen to be zero the additional constraint in the cost function minimises the quadratic norm of differences of adjacent components of the vector $\mathbf{x}$. This way the slope of the retrieved profile is forced towards zero and the resulting profile is smoothed. Applying this method the solution of the inverse problem is stabilised without taken additional a priori information of the absolute values of the profile into account. The assumption that the atmospheric profile is varying "smoothly" with altitude can be considered as adequate. This constraint implies that the profile remains constant if no information from the measurements is available, rather than being forced towards the absolute values of the a priori profile as with the optimal estimation method. In special cases the a priori profile $\mathbf{x_a}$ in Equation 4.36 can be

also chosen distinctly different from zero, which results in a forcing of the retrieved profile $\mathbf{x}$ towards the shape of the a priori profile $\mathbf{x_a}$. With the parameter γ the strength of the constraint can be chosen. Suchlike application of constraints is often called regularisation, because the additional term makes the involved matrix regular and therefore invertible.

The Tikhonov approach is equivalent to the optimal estimation approach with matrix $\mathbf{S_a}^{-1}$ set to $\gamma\mathbf{B}$, where $\mathbf{B} = \mathbf{L^T L}$. Therefore the solution can be found according to Equation 4.35:

$$\mathbf{x_{i+1}} = \mathbf{x_i} + (\mathbf{K_i}^\mathbf{T}\mathbf{S_y^{-1}}\mathbf{K_i} + \gamma\mathbf{B})^{-1}\left[\mathbf{K_i}^\mathbf{T}\mathbf{S_y^{-1}}(\mathbf{y} - \mathbf{f}(\mathbf{x_i})) - \gamma\mathbf{B}(\mathbf{x_i} - \mathbf{x_a})\right] \tag{4.38}$$

Using the Tikhonov constraint has also the advantage that no information on the covariance matrix $\mathbf{S_a}$ is needed, which contains the full set of uncertainties and its correlations of the a priori state $\mathbf{x_a}$, which is usually not accessible.

The strength of the regularisation (factor γ) can also be chosen to be altitude-dependent. In this case the factor γ in Equation 4.36 is replaced by a diagonal (n-1)×(n-1)-matrix with the specific γ-factors at the diagonal.

4.2.3 Error estimation

In general the retrieved state $\hat{\mathbf{x}}$ is the result of a retrieval method $\mathbf{R}$ applied to the measurements $\mathbf{y}$ [Rodgers, 2000]:

$$\hat{\mathbf{x}} = \mathbf{R}(\mathbf{y}, \hat{\mathbf{b}}, \mathbf{x_a}, \mathbf{c}) = \mathbf{R}(\mathbf{f}(\mathbf{x}, \mathbf{b}) + \boldsymbol{\epsilon}, \hat{\mathbf{b}}, \mathbf{x_a}, \mathbf{c}) \tag{4.39}$$

where $\hat{\mathbf{b}}$ is the best estimate of the forward function parameters, and $\mathbf{x_a}$ are the a priori state and $\mathbf{c}$ additional parameters of the retrieval.

The forward model $\mathbf{f}$ introduced in Equation 4.19 is an ideal model which represents the full physics of the radiative transfer in the atmosphere and the full description of the instrument. However, in reality, the forward model can always only be an approximation of such an idealised model. Therefore the ideal model $\mathbf{f}$ is replaced by the real model $\mathbf{F}$ which will always exhibit a model error $\boldsymbol{\Delta}\mathbf{f}$:

$$\hat{\mathbf{x}} = \mathbf{R}(\mathbf{F}(\mathbf{x}, \mathbf{b}) + \boldsymbol{\Delta}\mathbf{f}(\mathbf{x}, \mathbf{b}) + \boldsymbol{\epsilon}, \hat{\mathbf{b}}, \mathbf{x_a}, \mathbf{c}) \tag{4.40}$$

Linearising the forward model about $\mathbf{x} = \mathbf{x_a}$ and $\mathbf{b} = \hat{\mathbf{b}}$ yields:

$$\hat{\mathbf{x}} = \mathbf{R}(\mathbf{F}(\mathbf{x_a}, \hat{\mathbf{b}}) + \mathbf{K}(\mathbf{x} - \mathbf{x_a}) + \mathbf{K_b}(\mathbf{b} - \hat{\mathbf{b}}) + \boldsymbol{\Delta}\mathbf{f}(\mathbf{x}, \mathbf{b}) + \boldsymbol{\epsilon}, \hat{\mathbf{b}}, \mathbf{x_a}, \mathbf{c}) \tag{4.41}$$

Next, the inverse method $\mathbf{R}$ is linearised with respect to $\mathbf{y}$

$$\hat{\mathbf{x}} = \mathbf{R}(\mathbf{F}(\mathbf{x_a}, \hat{\mathbf{b}}), \hat{\mathbf{b}}, \mathbf{x_a}, \mathbf{c}) + \mathbf{G}[\mathbf{K}(\mathbf{x} - \mathbf{x_a}) + \mathbf{K_b}(\mathbf{b} - \hat{\mathbf{b}}) + \boldsymbol{\Delta}\mathbf{f}(\mathbf{x}, \mathbf{b}) + \boldsymbol{\epsilon}] \tag{4.42}$$

with $\mathbf{G}$ being the derivative $\frac{\partial \mathbf{R}}{\partial \mathbf{y}}$.

$$\hat{\mathbf{x}} - \mathbf{x_a} = \mathbf{R}(\mathbf{F}(\mathbf{x_a}, \hat{\mathbf{b}}), \hat{\mathbf{b}}, \mathbf{x_a}, \mathbf{c}) - \mathbf{x_a} + \mathbf{A}(\mathbf{x} - \mathbf{x_a}) + \mathbf{G}\boldsymbol{\epsilon_y} \tag{4.43}$$

Here $\mathbf{A}$ denotes the averaging kernel matrix, which is the derivative of the retrieved state $\hat{\mathbf{x}}$ to the true state $\mathbf{x}$:

$$\mathbf{A} = \mathbf{GK} = \frac{\partial \hat{\mathbf{x}}}{\partial \mathbf{x}} \tag{4.44}$$

and

$$\boldsymbol{\epsilon_y} = \mathbf{K_b}(\mathbf{b} - \hat{\mathbf{b}}) + \boldsymbol{\Delta}\mathbf{f}(\mathbf{x}, \mathbf{b}) + \boldsymbol{\epsilon} \tag{4.45}$$

The term $\mathbf{R}(\mathbf{F}(\mathbf{x_a}, \hat{\mathbf{b}}), \hat{\mathbf{b}}, \mathbf{x_a}, \mathbf{c}) - \mathbf{x_a}$ should be zero for any reasonable retrieval $\mathbf{R}$. Therefore, Equation 4.43 yields:

$$\hat{\mathbf{x}} = \mathbf{x_a} + \mathbf{A}(\mathbf{x} - \mathbf{x_a}) + \mathbf{G}\boldsymbol{\epsilon_y} = (\mathbf{I} - \mathbf{A})\mathbf{x_a} + \mathbf{Ax} + \mathbf{G}\boldsymbol{\epsilon_y} \tag{4.46}$$

Most interesting for the error consideration is the difference of the retrieved state $\hat{\mathbf{x}}$ to the true state $\mathbf{x}$:

$$\hat{\mathbf{x}} - \mathbf{x} = (\mathbf{A} - \mathbf{I})(\mathbf{x} - \mathbf{x_a}) + \mathbf{G}\boldsymbol{\epsilon_y} \tag{4.47}$$

$$= \underbrace{(\mathbf{A} - \mathbf{I})(\mathbf{x} - \mathbf{x_a})}_{\text{smoothing error}} + \underbrace{\mathbf{GK_b}(\mathbf{b} - \hat{\mathbf{b}})}_{\text{model parameter error}} + \underbrace{\mathbf{G}\boldsymbol{\Delta}\mathbf{f}(\mathbf{x}, \mathbf{b})}_{\text{forward model error}} + \underbrace{\mathbf{G}\boldsymbol{\epsilon}}_{\text{noise error}} \tag{4.48}$$

All these errors and the true state $\mathbf{x}$ are generally not known, but statistical information in terms of the uncertainties may be available. The deviation of the a priori state $\mathbf{x_a}$ from the true state $\mathbf{x}$ is not known, for instance, however, its uncertainties and their correlations are represented by the covariance matrix $\mathbf{S_a}$. The covariance matrix of the retrieved state $\hat{\mathbf{x}}$ can be found via generalised Gaussian error propagation:

$$\mathbf{S_x} = (\mathbf{A} - \mathbf{I})\mathbf{S_a}(\mathbf{A} - \mathbf{I})^{\mathbf{T}} + \mathbf{G}\mathbf{K_b}\mathbf{S_b}\mathbf{K_b}^{\mathbf{T}}\mathbf{G}^{\mathbf{T}} + \mathbf{G}\mathbf{S_f}\mathbf{G}^{\mathbf{T}} + \mathbf{G}\mathbf{S_y}\mathbf{G}^{\mathbf{T}} \tag{4.49}$$

where $\mathbf{S_b}$, $\mathbf{S_f}$ and $\mathbf{S_y}$ are the covariance matrices of forward model parameter errors, the forward model errors and the noise errors, respectively.

In the case of the Tikhonov approach the matrix $\mathbf{G}$, which is called Gain-Matrix is given by:

$$\mathbf{G} = (\mathbf{K}^{\mathbf{T}}\mathbf{S}_{\mathbf{y}}^{-\mathbf{1}}\mathbf{K} + \gamma\mathbf{B})^{-\mathbf{1}}\mathbf{K}^{\mathbf{T}}\mathbf{S}_{\mathbf{y}}^{-\mathbf{1}} \tag{4.50}$$

Because $\mathbf{S_b}$ and $\mathbf{S_f}$ are often hard to estimate, only the noise and the smoothing errors are considered in a lot of cases:

$$\mathbf{S_x} = (\mathbf{A} - \mathbf{I})\mathbf{S_a}(\mathbf{A} - \mathbf{I})^{\mathbf{T}} + \mathbf{G}\mathbf{S_y}\mathbf{G}^{\mathbf{T}} = (\mathbf{K}^{\mathbf{T}}\mathbf{S}_{\mathbf{y}}^{-\mathbf{1}}\mathbf{K} + \mathbf{S_a}^{-\mathbf{1}})^{-\mathbf{1}} \tag{4.51}$$

It has, however, been challenged that the smoothing effect is adequately characterised by the smoothing error term $(\mathbf{A} - \mathbf{I})\mathbf{S_a}(\mathbf{A} - \mathbf{I})^{\mathbf{T}}$ [von Clarmann, 2014].

4.2.4 Averaging kernels, altitude resolution and degrees of freedom

The averaging kernel matrix $\mathbf{A}$ can be calculated using Equation 4.44 and determines the amount of a priori information contained in the measurement, which is reflected by Equation 4.46. In the ideal case the averaging kernel matrix is equal to the unit matrix and no a priori knowledge is used. The i-th row of $\mathbf{A}$ is defined as $\frac{\partial \hat{x}_i}{\partial \mathbf{x}}$ and therefore the dependence of the profile value of the retrieved state at altitude i on all other altitudes of the true state $\mathbf{x}$. In general the component i of the retrieved state $\hat{\mathbf{x}}$ will not only depend on x_i, but also on adjacent altitudes. Thus, the retrieved profile will be smoothed and the corresponding error $(\mathbf{A} - \mathbf{I})(\mathbf{x} - \mathbf{x_a})$ is referred to as smoothing error. The half-width of the i-th row of the averaging kernel matrix is usually used as a measure for the altitude resolution of the retrieved state at altitude i.

The j-th column of $\mathbf{A}$ is defined as $\frac{\partial \hat{\mathbf{x}}}{\partial x_j}$ and reflects the response of a δ-pulse perturbation in the j-th component of the true state vector on the whole retrieved state.

The degrees of freedom of the retrieved profile, which is defined as the number of independent components $\hat{x_i}$, is equal to the trace of the averaging kernel matrix:

$$dgf = tr(\mathbf{A}) \tag{4.52}$$

The maximum value of the degrees of freedom is n. Using the Tikhonov approach this is the case if γ is set to zero, i.e. if no regularisation is applied. Regularisation reduces the degrees of freedom.

4.3 The sequence of operations

The IMK MIPAS processor is designed to retrieve atmospheric trace gases either sequentially or simultaneously. The retrieval of all atmospheric parameters, like pressure, temperature, line of sight (LOS) and the total set of analysed trace gases is subdivided into subsequent retrieval steps. At first atmospheric parameters are determined which are required for later retrieval steps. In particular, prominent trace gases are retrieved first, which exhibit well separated and unambiguous spectral "signatures" in dedicated parts of the analysed spectrum, called analysis-windows or "microwindows" [von Clarmann, 2003]. The retrieved abundances of these trace gases, in turn, are used as input for further retrievals of trace gases, whose spectral signatures are superimposed by emission spectra of the formers. This means that the results of preceding retrieval steps are considered in the forward calculation of the subsequent retrievals, but kept constant. In terms of the mathematical description of the retrieval procedure (see Section 4.2), the vector $\mathbf{x}$ does not include the full state of the atmosphere but only the variables retrieved in the current step. Results from preceding retrieval steps are compiled in the forward model parameter vector $\mathbf{b}$ (introduced in Section 4.2) in the current retrieval step. Such-like quantities are also referred to as "prefit parameters". Some trace gases analysed with the IMK MIPAS processor interfere with emission lines of other species for which no prefits were available, because they are not a part of the operational IMK MIPAS "retrieval chain". Thus, these trace gases are usually simultaneously fitted along with the target gas and are therefore referred to as "joint-fit gases". This means the vertical profiles of their mixing ratios are now part of the state vector $\mathbf{x}$ to be retrieved. For other interferents, even though their prefits are provided, it is occasionally adequate to jointly fit these gases along with the target gas, too, because spectroscopic inconsistencies in the target analysis-window and the interferents' dedicated analysis-window can cause artefacts, when the known abundances (in terms of prefits) are used to model the spectral contributions of these gases in the target analysis-window. In this case the prefit parameters can be used as a priori (see Section

4.2) for the current retrieval.

The first step in the MIPAS level-2 processing with the IMK processor is the retrieval of spectral shift, pressure, temperature and line of sight (LOS) (details of this procedure can be found e.g. in von Clarmann et al. [2003]), followed by the retrievals of water vapour and O_3 being the most prominent trace gases. Subsequently, HNO_3, CH_4 and N_2O are retrieved, followed by minor trace species, and eventually SF_6, the target gas analysed in this thesis, until the complete set of gases detectable with MIPAS is processed. The specific configuration of the retrieval of SF_6 used in this thesis is presented in the next chapter.

Chapter 5

Inversion of the radiative transfer equation

For the inversion of the radiative transfer equation the MIPAS data processor (details can be found e.g. in von Clarmann et al. [2003, 2009]) developed at IMK/IAA was used.

The SF_6 retrieval setup is based on the setup developed by Stiller et al. [2008, 2012] for SF_6. One scope of this work was to improve this setup to obtain a better SF_6 data set. For instance, known deficits of the original setup were a local SF_6 maximum in the tropical stratosphere at approximately 36 km altitude, which seemed to have no physical explanation (see Section 5.2 and 5.9.1), as well as low SF_6 values in higher altitudes leading to very unrealistically high ages of air there. Numerous sensitivity studies have been carried out trying to optimise the setup of the retrieval algorithm. In the beginning, these studies were performed mainly on the basis of data version V4O spectra (ESA version 4.67) in reduced resolution. Later, spectra from version V5R (ESA version 5.06), which appeared to be of higher quality, became available and were used. The main aim was to minimise the residual of the measured atmospheric spectra and the best fitting modelled spectra, which have been calculated by the Karlsruhe Optimized and Precise Radiative Transfer Algorithm (KOPRA, Funke and Höpfner [2000]; Stiller [2000]; Stiller et al. [2002]) as part of the IMK retrieval processor. In the ideal case the residual $\mathbf{y} - \mathbf{f}(\mathbf{x}, \mathbf{b})$ consists only of the measurement noise $\boldsymbol{\epsilon}$ (see Equation 4.19). However, in reality residuals are considerably larger and show more structure for several reasons: First the ideal forward model $\mathbf{f}$ is represented by a real model $\mathbf{F}$ which is always an approximation and can never cover the whole physics of the ideal model $\mathbf{f}$. The real residuals will therefore contain the additional forward model error $\boldsymbol{\Delta}\mathbf{f}$ (see Section 4.2.3). Secondly, the ideal model parameter vector $\mathbf{b}$ is

unknown and can only be represented by its best estimate $\hat{\mathbf{b}}$. Thus, the residuals also contain the term $\mathbf{K_b}(\mathbf{b}-\hat{\mathbf{b}})$ (see Section 4.2.3) which results from the less-than-perfect estimation of the forward model parameters. The forward model $\mathbf{F}$ was available and had been proven to be of high accuracy. Thus the related forward model error $\mathbf{\Delta f}$ was considered to be sufficiently small. Instead, the focus of this thesis was to minimise the residuals by finding optimised settings of the forward model parameters and other retrieval settings. Reduced residuals by means of optimised parameters imply a better estimate of the retrieved atmospheric state $\hat{\mathbf{x}}$ (see Equation 4.49), in this case a better estimate of the SF_6 atmospheric profile.

In order to investigate the residuals, spectra of one selected day (about 1300 spectra) at tangent altitude 12 ($\approx$ 24 km) have been coadded to reduce the noise in the spectra. Otherwise possible systematic structures in the residuals would be masked by the dominating noise. Then the difference between modelled and measured coadded spectra was evaluated. In addition, the value of χ^2, which is a measure of the total quality of the fit, was analysed.

Besides minimisation of the residuals due to more adequate settings, also the different level-1 data versions caused considerably different residuals. Residuals looked totally different in version V5R then in V4O and were much smaller. Especially the CO_2 lines were fitted better. This is attributed to better calibration by ESA.

5.1 Analysis-window and contributing gases

SF_6 was retrieved in the same analysis-window called "microwindow" that has also been used by Stiller et al. [2008, 2012] in the wavenumber range 941-952 cm^{-1}. Figure 5.1 shows the expected major spectral contributions of trace gases in this microwindow based on climatologies [Remedios et al., 2007] as observed by the MIPAS instrument in reduced resolution in July in the tropics at 20 km altitude. Most of the radiation in this microwindow is emitted by CO_2 (in blue) via the laser band (large peaks, 00011 $\rightarrow$ 10001) and the hot band (small peaks, 01111 $\rightarrow$ 11101).

The expected SF_6 signal is shown as red line and corresponds to the SF_6 cross section with a peak around 947.9 cm^{-1} (Q-branch of the ν_3 band) and some broadband spectral contributions on the left and right hand side. The SF_6 peak is strongly superimposed by a CO_2 laser line (at 947.74 cm^{-1}) and a hot band line (at 947.94 cm^{-1}), so a very good modelling of the CO_2 lines is needed in order to obtain an accurate value for the SF_6 volume mixing ratio. This is one reason why it is crucial to use a non-LTE modelling of the CO_2 lines. Also other gases are expected to contribute to the total

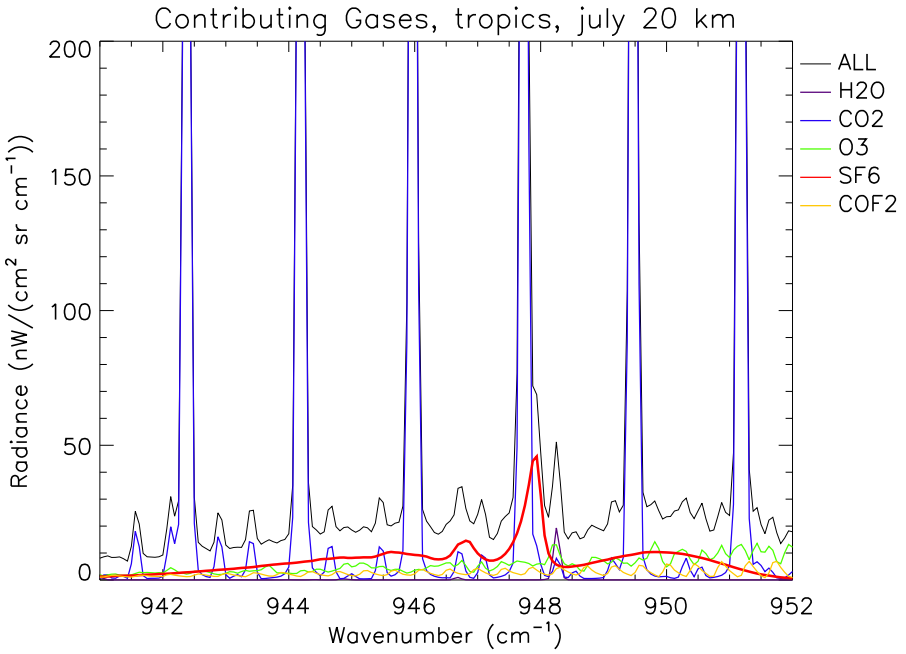

Figure 5.1: Contributing trace gases to a typical spectrum measured in the tropics in July at 20 km (reduced resolution) with the SF_6 signature in red.

spectral signal. Mainly water vapour with a line around 948.26 cm^{-1} but also ozone and COF_2 have spectral features in this microwindow. These gases are therefore included as joint-fit variables (cf. with Section 4.3) in the retrieval (see Section 5.3). The total set of gases considered by the retrieval were H_2O, CO_2, O_3, N_2O, NH_3, COF_2, CFC-12 and SF_6. Gases which were not jointly fitted contributed to the forward calculation in KOPRA either as "prefit" (see Section 4.3) from previous retrievals (if available) or from climatologies. For H_2O and O_3 MIPAS results from the H_2O and O_3 retrieval were used as prefits, as well the spectral shift and TLOS (temperature, pressure and line of sight (LOS)). In addition, the CO_2 vibrational temperatures, which are important for the non-LTE treatment (see Section 5.6), have been incorporated from a preceding CO retrieval.

Several attempts have been made to extend the microwindow to the low and high wavenumber side with some additional lines of the CO_2 laser band in order to stabilise the retrieval with providing more information on CO_2. The CO_2 laser lines appeared to be fitted better while the residual at the water line increased. The effect on the SF_6 mean profile over 1 day (15 orbits, approx. 1200 geolocations) was negligible. The microwindow was also divided into several submicrowindows, one for each CO_2 laser line. But the residual did not get significantly better. So in the end it was decided to return to the original microwindow.

5.2 Continuum and offset

Radiation which is only weakly dependent on wavenumber is called continuum. A continuum signal is produced in the atmosphere by emissions of aerosols and clouds as well as the superimposed effect of far wings of spectrally distant transitions. In order to model the atmospheric spectra well, this continuous radiation (in spectral space) has to be included in the forward model. In the original SF_6 retrieval developed by Stiller et al. [2008, 2012], the continuum was considered up to an altitude of 33 km, because no considerable amount of aerosols above the Junge layer was expected. In addition, a height-independent offset was used to account for a possible shift in intensity between measured and modelled spectra, resulting from a less-than-perfect radiance calibration.

In Stiller et al. [2012], Figure 3 shows an isolated age of air minimum (SF_6 maximum) in the tropical stratosphere at about 36 km altitude. This minimum occurs due to a local maximum in the (daily or monthly) averaged SF_6 profile (see Figure 5.2 for a daily averaged profile). It could be shown that this local maximum vanishes if continuum contributions were allowed up to 50 km altitude or a height-dependent offset was used (see Figure 5.2). This leads to the assumption that this SF_6 maximum might be an artefact by the retrieval and that continuum radiation is falsely assigned to a signal from SF_6 mixing ratio, resulting in a higher SF_6 value. Fitting a height-dependent offset or continuum leads to the same result, as both are accounting for a continuous (constant in the microwindow) radiation in a transparent atmosphere. Continuum uses a constant absorption cross section while offset simply adds a constant term in the radiances. Differences between continuum emission and radiance offset occur only in saturated emission lines, where offset shifts the total radiances while continuum does not increase the radiances in the saturated lines over the Planck function. Both, continuum fitted from the ground to 50 km and height-dependent offset, lead to almost similar mean SF_6 profiles (see Figure 5.2).

Attempts to fit height-dependent offset and continuum in the same altitude range led to smallest residuals, but caused very high offset values on the one side and very negative values of continuum compensating on the other side or vice versa, because the Jacobians of continuum and offset are linearly dependent in wavenumber space (provided that the microwindow is small compared to the Planck function causing the continuum) and therefore lead to a null space. This made the retrievals very unstable.

Usually the offset is not regularised because it is retrieved on the tangent height grid. Several attempts were made to constrain the offset at the altitudes where continuum was fitted while fitting jointly offset and continuum. Doing this, unrealistically high

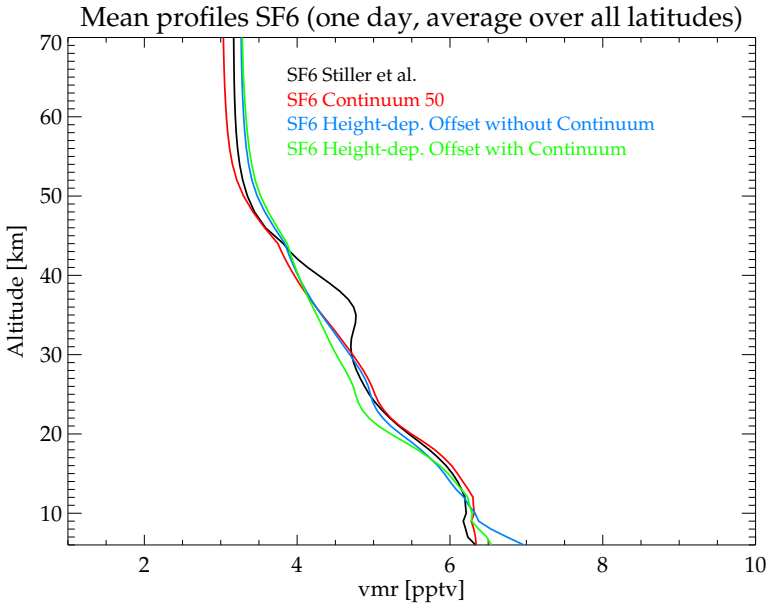

Figure 5.2: Mean profiles for one day for different Continuum/Offset-settings

values of continuum and offset oscillating opposite in phase could be avoided, but no improvement of the residuals were achieved.

In the end it was decided to use continuum up to 50 km with a height-independent (constant) offset rather than using a height-dependent offset which is physically more reasonable. The constant offset had to be constrained in order to avoid unrealistic high values.

The continuum which caused the artefact could be due to stray light. This was investigated in Section 5.9.1. In Neely III et al. [2011] it is discussed that there could be aerosol even above the Junge layer causing additional continuum radiation due to meteoritic dust.

5.3 Jointly fitted gases

In the original retrieval setup developed by Stiller et al. [2008, 2012] only CO_2 and H_2O were used as joint-fit gases. To account for a not implemented non-LTE treatment of CO_2, the laser band and the hot band were treated like two independent gases which both were fitted jointly. In addition continuum and a constant offset were fitted simultaneously with the gases (see section 5.2 continuum and offset). In the new retrieval setup CO_2 was treated with non-LTE so only one gas was needed to model both the CO_2 laser line and the hot band.

It turned out that the residual could be further minimised if additional joint-fit gases

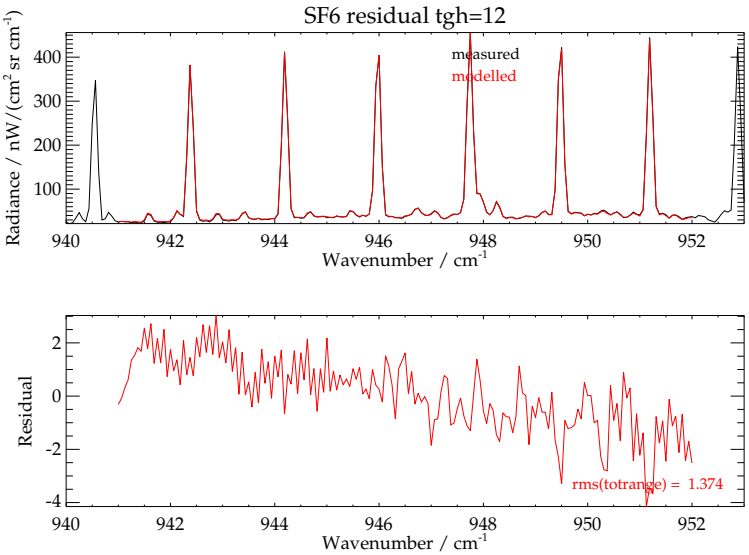

Figure 5.3: Coadded spectra for tangent height 12 (measured and modelled) over one day

are added in the retrieval. Figure 5.3 shows the setup with the joint-fit configuration of the old retrieval setup. The residual appears to be tilted. In Figure 5.1 it can be seen that also other gases are expected to contribute to the measured signal, especially COF_2 and ozone. Both signatures of COF_2 and ozone are also increasing from the left hand side of the microwindow towards the right hand end of the microwindow (see Figure 5.1). This could be one reason, why the residual without COF_2 and ozone seems to be tilted.

Figure 5.4 shows the same picture with COF_2 as additional joint-fit. It can be seen that the root mean square (RMS) of the residual gets slightly smaller while the residual still looks tilted.

If also ozone is added as joint-fit gas, the residual finally becomes straight and its RMS becomes significantly smaller (see Figure 5.5). The regularisation (see Section 5.4) for ozone was chosen to be the standard regularisation vector for the ozone retrieval processed at IMK/IAA divided by a factor of 100.

5.4 A priori profiles, first guess and regularisation

Whereas the original retrieval setup for SF_6 developed by Stiller et al. [2008, 2012] used a variant of the Tikhonov [1963] regularisation scheme developed by Steck [2002], in the new retrieval setup a regularisation scheme, where the altitude dependence of the regularisation was implemented in a more adequate manner, was used.

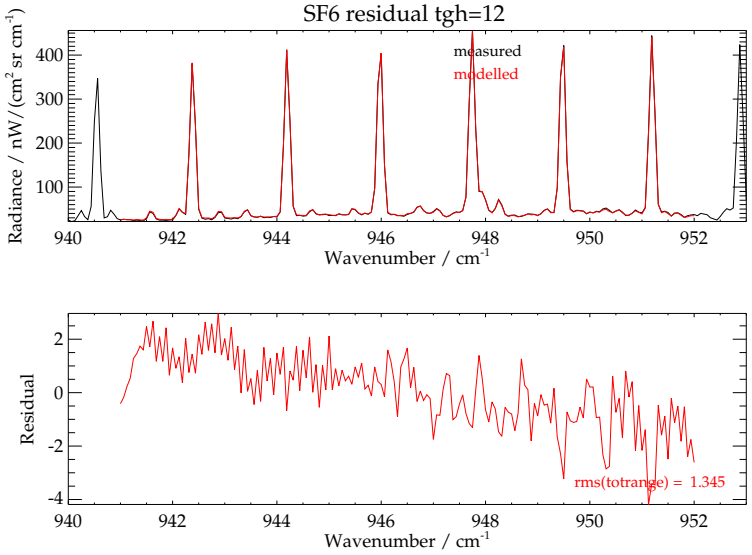

Figure 5.4: Coadded spectra for tangent height 12 (measured and modelled) over one day with COF_2 as joint-fit

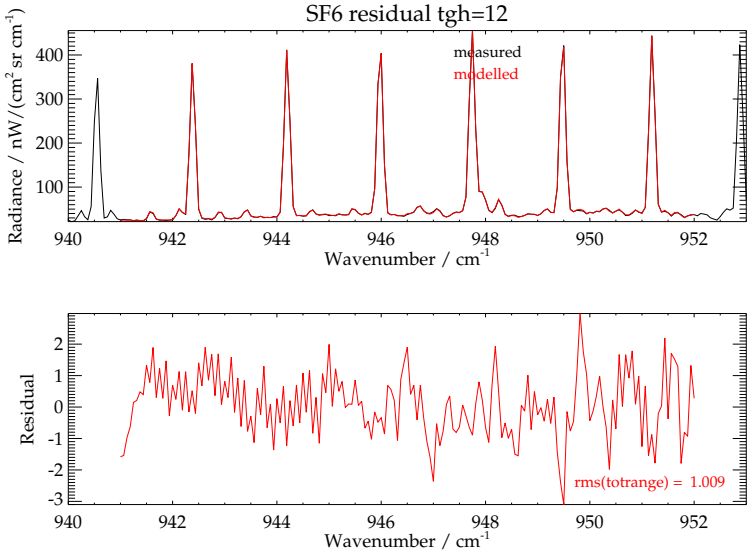

Figure 5.5: Coadded spectra for tangent height 12 (measured and modelled) over one day with COF_2 and O_3 as joint-fit

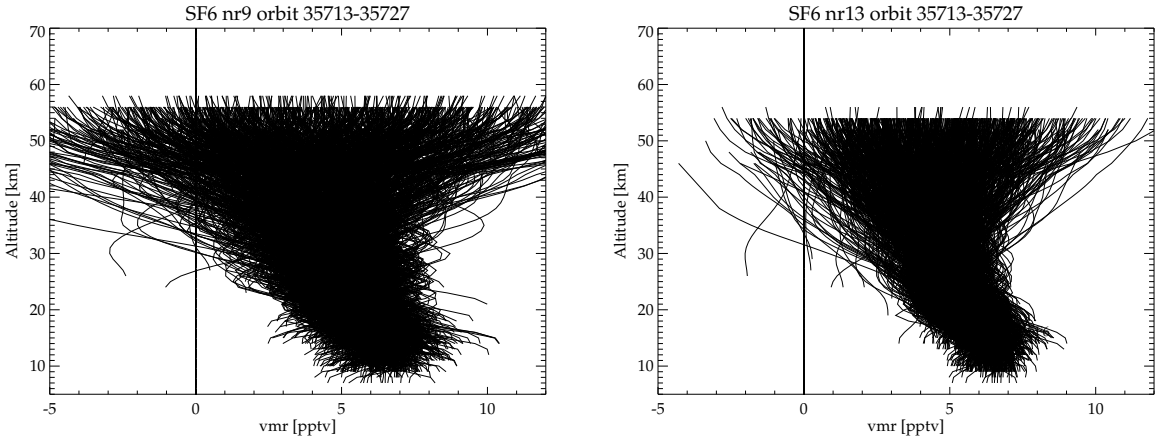

Figure 5.6: All single SF_6 profiles for one day overplotted to illustrate the variability with regularisation strength $5{\times}10^5$ (left) and 10^6 (right)

The target SF_6

For the target gas SF_6 a height-constant regularisation with $\gamma = 10^6$ was used as in the original setup. With this regularisation the SF_6 profiles have typically about 3-6 degrees of freedom. First, it was tested if better altitude resolution could be obtained by lowering the regularisation strength to 0.5×10^6. But the variability of SF_6 profiles was found to be too large (see Figure 5.6, left panel); in particular, too many profiles were getting negative or exceeded the low-altitude values for high altitudes. Figure 5.6 (right panel) shows profiles retrieved with the original regularisation strength, which seem to be more realistic even though some profiles are still getting negative or increasing with high altitudes which is not physical because there are no sources of SF_6 in the stratosphere and mesosphere.

As a priori profile the constant zero profile was applied. Since a Tikhonov-type regularisation is used, the profile is forced towards a constant profile i.e. the profile is smoothed. As first guess profile a profile from a climatology [Remedios et al., 2007] is used.[1]

[1] note that Equation 4.38 does not require that the iteration is started with the a priori profile $\mathbf{x_a}$ but can start from any initial guess $\mathbf{x_0}$.

The consideration of CO_2 (joint-fit)

For the jointly fitted gas CO_2 a height-constant regularisation vector of 0.05 was used while the regularisation constant in the original retrieval was approximately 0.01 for the laser band and approximately 0.46 for the hot band, respectively. With this regularisation factor the resulting CO_2 profile has about 4-10 degrees of freedom. It was tried to relax the regularisation by a factor of 10, but the residuals in several chosen tangent heights did not improve and the mean CO_2 profile looked not physical exhibiting a "nose" around 55 km. The constant zero profile was again used as a priori profile. The first guess profile for the iteration was taken from climatologies [Remedios et al., 2007].

The consideration of H_2O (joint-fit)

The water vapour spectral line is located near the SF_6 spectral maximum, so it is expected that its mixing ratio covariates with negative correlation with the SF_6 mixing ratio (see Figure 5.1). But overall there is too little information on water vapour in this particular microwindow, so using a flat zero a priori profile with a relatively loose regularisation is not a good choice here. Instead, as a priori and first guess profile the water vapour profile from the preceding regular water vapour retrieval was used for every geolocation. The regular water vapour retrieval uses multiple transitions which carry sufficient information for a robust retrieval. The only purpose of the re-consideration of water vapour as a fit parameter in the SF_6 retrieval is to allow compensation of possible inconsistencies of the spectroscopic data of the respective water vapour lines. The regularisation vector is a multiple of the one in the water vapour retrieval which is constant throughout the atmosphere up to 64 km and then increases. This vector was scaled by a factor of 5, so the resulting water vapour profiles have typically 1 to 1.5 degrees of freedom. Basically the profiles have the shape of the a priori profile, while only a shift in mixing ratio is allowed. The residual near the water vapour line did not get better when the regularisation for water vapour was relaxed. Whatever the regularisation for water vapour was or which a priori was used (constant zero or water vapour prefit), it did not have any effect on the SF_6 profile. Water vapour is very important in the troposphere but it decreases over many magnitudes towards the tropopause where it has a minimum (hygropause). In the stratosphere it has a small maximum due to oxidation of methane. The shape of the water vapour profile is crucial in the troposphere but since only stratospheric SF_6 is retrieved, tropospheric water vapour has only minor impact on the SF_6 profiles.

The consideration of COF_2 (joint-fit)

There is not much information contained on COF_2 in the microwindow (see Figure 5.1), so a climatology [Remedios et al., 2007] served as a priori and first guess profile since there was no prefit of COF_2 available. The regularisation was chosen relatively strong so the resulting COF_2 profiles have about 1.5 to 3.5 degrees of freedom.

The consideration of O_3 (joint-fit)

Like COF_2, ozone is not contributing much to the signal in the used microwindow (see Figure 5.1), but prefits from the ozone retrieval existed. So the ozone prefit served as a priori and first guess profile. In the beginning, the new retrieval setup was developed with a regularisation of the original ozone retrieval vector divided by a factor of 100, because RMS and χ^2 became small here, but later it was decided to use the original ozone regularisation reduced by a factor of 10, because again there was too little information on ozone in the retrieval and the retrieved profile was oscillating too much.

The consideration of continuum (joint-fit)

The continuum was regularised in the standard way applied at IMK/IAA, but it was considered up to an altitude of 50 km (see Section 5.2), that means it was regularised Tikhonov-like up to an altitude of 50 km and constrained to zero at higher altitudes by setting the respective entries of the diagonal of the regularisation matrix to large values.

The consideration of constant offset (joint-fit)

The joint-fit constant offset had to be regularised in order to avoid high values interfering with the continuum (see Section 5.2). The first guess was zero. With this regularisation typical offset values were between -10 and 10 $nW/(cm^2\ sr\ cm^{-1})$.

5.5 Number of used tangent heights

In the original retrieval setup developed by Stiller et al. [2012] the first 19 tangent heights out of the 27 tangent heights, covering the altitude range of approximately 5 to 40 km, in MIPAS reduced resolution mode were used. Incorporation of more

tangent heights led to artefacts in the mean retrieved SF_6 profiles exhibiting a strong "nose" at higher altitudes with mixing ratios even greater than the low-altitude ones. By employing continuum as a joint-fit parameter up until 50 km, this artefact could be avoided (see Section 5.2). Therefore it was tried to use more tangent heights and indeed by using 22 tangent heights (up to 50 km) more information could be gained in the upper altitudes, i.e. the averaging kernels increased slightly at higher altitudes. In addition the RMS of the residuals at upper tangent heights decreased. With the new retrieval setup for the first time it made sense to include 22 tangent heights instead of 19. The mean SF_6 profile contains more information in the altitude range 40-50 km and is varying more rather then becoming a straight line as before, when no information could be extracted out of the measurements.

5.6 Non-LTE treatment

Using both V3O (high resolution) and V4O (low resolution) spectra the attempt of including non-LTE treatment of CO_2 lines always led to smaller residuals than the one with the LTE setup for CO_2. However, this was not true for V5R spectra, where the residuals of the previous LTE setup were slightly smaller than the one with the new non-LTE setup. But keeping in mind that the old setup had more fit parameters because two CO_2 gases (one for the laser band and one for the hot band) were used (compare with Section 5.3) it is not surprising that smaller residuals are found for the old setup. Contrary, the reduced χ^2 [1] was found to be smaller for the new non-LTE setup. Non-LTE effects are mostly observed during daytime, due to insolation, so differences between day and night are expected to be smaller with the non-LTE setup. And indeed the day/night difference in the residuals was minimised with the non-LTE setup.

5.7 Spectroscopic parameters

Spectroscopic data were used from a dedicated MIPAS database for gases like H_2O, CO_2, O_3 and COF_2 (Flaud et al. [2003]). For N_2O, NH_3, CFC-12 and SF_6 the spectroscopic database HITRAN2000 [Rothman et al., 2003] was used.

The spectral line and cross section data, respectively, have to be calculated for the pressures and temperatures of the atmospheric layers by the forward model. The

[1] The reduced χ^2 is defined as the χ^2 divided by the degrees of freedom.

accuracy with which this is done is set by the accuracy parameter. The default value of this parameter is 10^{-5}. In the final setup an accuracy parameter of 10^{-6} was used.

5.8 Further retrieval settings

Beyond the retrieval settings discussed above a series of further residuals have been critically assessed, but no improvement could be achieved and the original settings by Stiller et al. [2008, 2012] were found to be adequate. These settings are listed below for completeness.

1. The default value of the number of pencil beams (see Section 4.1) used is 7 in the lowest tangent heights and 5 above the fifth tangent height. A test retrieval was run with the maximum possible accuracy of 21 pencil beams, but no significant difference was found in the residuals, RMS of the residuals and χ^2.

2. Attempts to use a newer spectroscopic database like HITRAN2008 worsened the residuals in most tangent heights.

3. It was tried to use pseudolines (see Section 4.1.1) as spectroscopic input instead of cross sections for SF_6. However, the residuals increased.

4. Several trials were made with setting the accuracy parameter (see Section 5.7) to 10^{-6} and 10^{-8} (the default value is 10^{-5}), but the residuals did not change. It also had almost no impact on the computation time.

Thus, for #1 - #3 the original settings were maintained, while for #4 the accuracy parameter of 10^{-6} was used.

5.9 Summary and critical discussion

5.9.1 SF_6 "nose"

In this section the artefact of a local SF_6 maximum at an altitude of approximately 36 km, which occurs when no background radiation contribution in terms of continuum or offset is fitted in that altitude (see section 5.2), is investigated.

This "nose" occurs mostly in the summer hemisphere and highest interhemispheric differences are found at the poles and lowest in the tropics. This strengthens the assumption that this continuous radiation is caused by stray light from the ground or lower and warmer atmospheric layers. These layers obviously would radiate more in summer and this would explain the observed behaviour. Also the "nose" is slightly larger during daytime, as one would expect for the stray light assumption. If the SF_6 regularisation strength is lowered to a quarter of the original one, the SF_6 values at the "nose" are even exceeding the ground values which is definitely not physical because SF_6 has no sources in the stratosphere.

If the continuum is cut off lower than usually at 33 km, then the "nose" is also shifted to lower altitudes and increases. This means that if the continuum is cut off then the background radiation above is falsely assigned to SF_6. The lower the continuum is cut off, the lower and bigger is the "nose". If the continuum is cut off above 50 km, then the "nose" vanishes totally. Despite the continuous radiation which is put into the SF_6 mixing ratio, the "nose" could also be a "cut off"-artefact of the continuum.

Almost half of the single retrieved profiles of one test day exhibit a "nose" around 36 km. The filtered geolocations "with nose" appeared mostly in the Southern Hemisphere (where it was summer on the test day) and very rarely in the northern polar latitudes (where it was winter on the test day). This would also be compatible with the stray light hypothesis.

5.9.2 So-called "bad" profiles

A lot of single retrieved SF_6 profiles exhibit a "bad" behaviour, i.e. they increase with altitude and their values at highest altitude exceed values at lowest altitudes, which makes physically no sense since there are no sources of SF_6 in the stratosphere. There are also profiles which decrease even to values below zero and become negative at high altitudes. In order to test if there is anything systematically wrong, the distributions of SF_6 values at several altitudes were investigated.

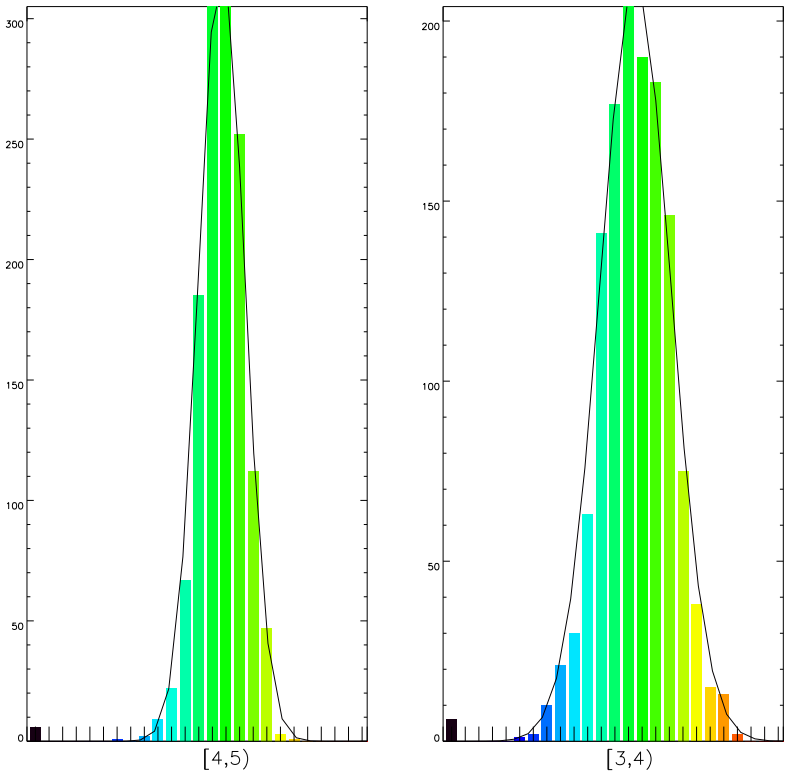

Figure 5.7: Distribution of SF_6 values at 40 km altitude (left) and 50 km altitude (right) for one day in intervals of 1 pptv. Intervals of the maximum are marked.

In Figure 5.7 the distribution of SF_6 values in intervals of 1 pptv is shown for 40 km and 50 km. The intervals of the respective maximum are marked. It can be seen that the distributions look (apart from the outliers at the lowest end of the distribution) approximately Gaussian. This means that there is no clear indication for a systematic problem. High SF_6 values in high altitudes are just a part of a normal distribution. "Bad" profiles are statistically compensated in tendency by other profiles with anomalies of the opposite sign. Mean profiles, which are used in this work will exhibit a normal behaviour, i.e. they will decrease monotonically with altitude as expected. It is also visible in Figure 5.7 that the variation of SF_6 values increases with altitude due to the decreasing signal-to-noise ratio. The maximum of the distribution is shifted from the interval [4,5] pptv at 40 km to [3,4] pptv at 50 km as expected because air is getting older with altitude.

5.9.3 The final average profile

In Figure 5.8 the mean SF_6 profile of the final new developed setup compared to the original setup developed by Stiller et al. [2012] for one test day covering all latitudes

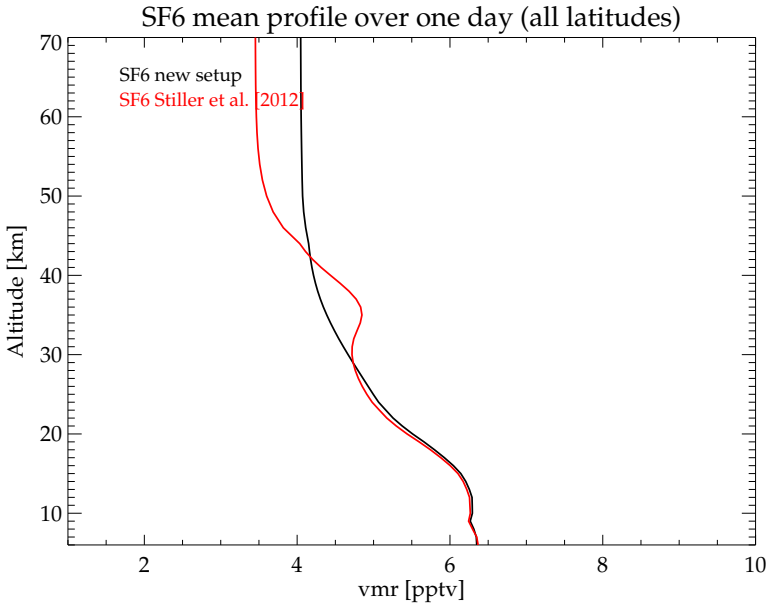

Figure 5.8: Mean profile of one day over all latitudes of the new retrieval setup compared to the old setup.

is shown. The main feature of the newly developed setup is the absence of the "nose" in the mean profile at an altitude of approximately 36 km. Further, the new setup does not lead to unrealistically low SF_6 values in the upper stratosphere which was a problem of the old setup leading to very old ages above 45 km. Up to an altitude of 30 km both profiles do not differ much. In this region of the atmosphere the retrieval was very robust, i.e. whatever changes were made during the sensitivity studies, the mean profile stayed approximately the same. Above an altitude of 50 km the profile of the new setup approaches a constant value of about 4 pptv, because at these altitudes there is almost no information on SF_6 left and the profile is forced towards the slope of the a priori profile, which is constant (cf. Section 4.2).

It should be mentioned, that no tuning has been performed to force the retrieval towards the expected profile. Instead, all improvements are achieved by modifications of the retrieval setup which are physically justified and appropriate.

5.9.4 Summary of all major changes in the new retrieval setup

With the new retrieval setup the unphysical "nose" (see Section 5.9.1) in the SF_6 profiles could be avoided by considering the continuum (see Section 5.2) above the standard upper boundary of 33 km up to an altitude of 50 km. The offset was regularised to minimise interference with continuum. The set of 19 tangent heights was extended to 22 tangent heights by which a bit more information could be gained in the

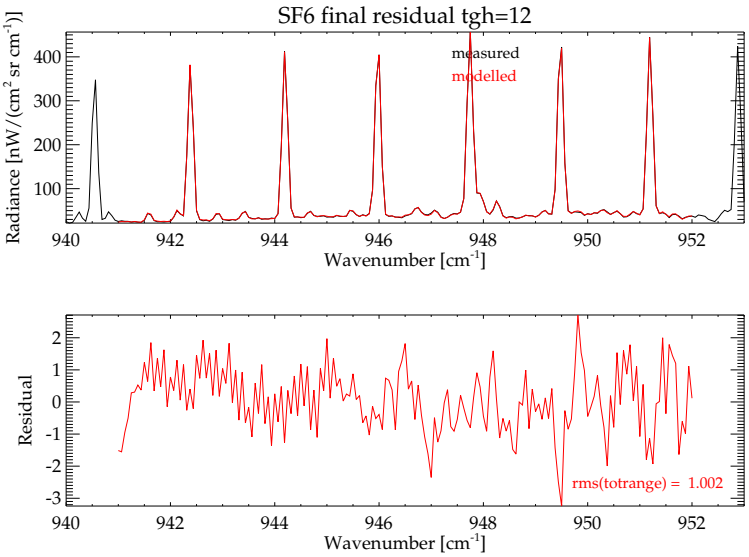

Figure 5.9: Coadded spectra for tangent altitude 12 (measured and modelled) over one day for the final retrieval setup

altitude range of 40-50 km.

The main spectrally contributing gas CO_2 was treated with an explicit non-LTE approach which replaced the old setup in which the two CO_2 bands were treated separately like two individual gases to emulate the non-Boltzmann-like populations of states. The use of V5R spectra reduced the residuals especially at the CO_2 lines. To further reduce the residuals, COF_2 and ozone were added in the joint-fit retrieval which also removed a tilt in the residuals.

The regularisation of SF_6 and all joint-fit gases was changed from a "Steck" regularisation scheme [Steck, 2002] to a Tikhonov type. The Steck approach forces the profile towards the a priori (in the case of SF_6 to zero) if no information is available while the Tikhonov regularisation forces the profile towards a constant value, which is more appropriate for SF_6.

In Figure 5.9 the residual at tangent height 12 of the final retrieval setup is shown while Figure 5.10 shows the respective residual of the old setup. It can be seen that the residual improved substantially. Especially the CO_2 lines and the water vapour line (compare with Figure 5.1) are fitted much better and overall the RMS of the residual has been reduced from about 1.8 to 1.0.

The improvements achieved in the residuals are dependent on altitude and latitude. In Table 5.1 previous and final RMS of the residuals between measured and modelled spectra resolved in latitude bands of 30° for our example day for three selected tangent

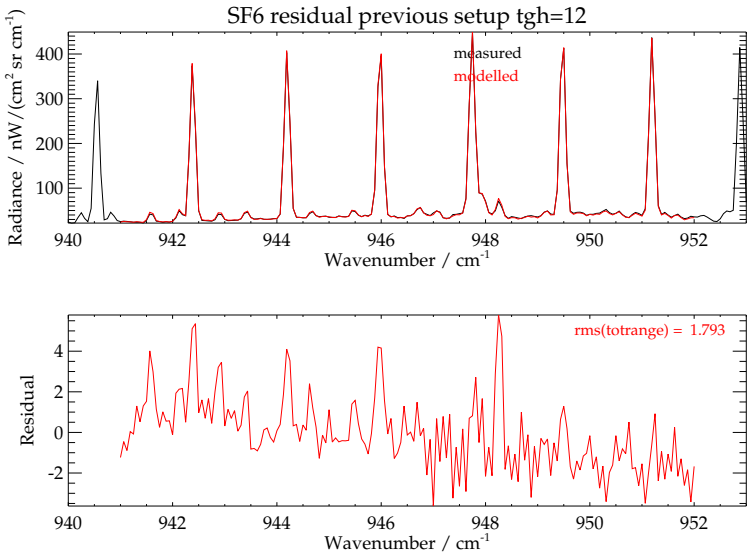

Figure 5.10: Coadded spectra for tangent altitude 12 (measured and modelled) over one day for the old retrieval setup

altitudes are presented. The relative improvements are largest in the tropics, amounting to about 40 %, and are smallest in the northern polar stratosphere, where infrared radiances are small, because our example data were a day in boreal winter.

The newly developed retrieval setup was also applied to the FR-period where the better calibrated spectra of version V5H (ESA version 5.02) were used. In particular the spectra of the FR period no longer suffer from a calibration insufficiency which was reported as "baseline oscillations" in Stiller et al. [2008]. Further technical details on the MIPAS level 1b data can be found at https://earth.esa.int/web/sppa/mission-performance/esa-missions/envisat/mipas/products-and-algorithms/products-information. In the following chapters the whole SF_6 data set (FR and RR-period) processed with this new retrieval setup will be used and investigated.

Table 5.1: Previous and final RMS of the residual for tangent altitude 12, 14 and 16 with coadded spectra over 1 day.

Latitude band	RMS previous	RMS final	Rel. improvement
Tangent altitude $12 \approx 24$ km			
0–30	1.861	1.108	40 %
30–60	1.704	1.188	30 %
60–90	1.092	1.001	8.3 %
−30–0	2.034	1.157	43 %
−60– −30	2.361	1.390	41 %
−90– −60	2.808	1.871	33 %
Tangent altitude $14 \approx 28$ km			
0–30	1.567	1.003	36 %
30–60	1.365	0.909	33 %
60–90	1.021	1.001	2 %
−30–0	1.786	1.035	42 %
−60– −30	1.987	1.229	38 %
−90– −60	2.432	1.6841	31 %
Tangent altitude $16 \approx 31$ km			
0–30	1.921	1.040	46 %
30–60	1.294	1.025	21 %
60–90	1.012	0.946	7 %
−30–0	1.971	1.034	48 %
−60– −30	1.969	1.117	43 %
−90– −60	2.037	1.547	24 %

Chapter 6

Observed SF_6 and age of air

6.1 The new SF_6 data set

The new SF_6 data set covers the total MIPAS period from July 2002 to April 2012. During this time several data gaps occurred, the largest one after the instruments' failure in March 2004 and resuming operation with a degraded spectral resolution in January 2005 (see Chapter 3). This new data set has been produced with the MIPAS processor developed at IMK/IAA [von Clarmann et al., 2003] using a revised retrieval setup described in Chapter 5. It comprises a set of approximately 2.3 million single SF_6 profiles which have been retrieved using the complete set of nominal mode MIPAS V5H and V5R spectra measured at geolocations that cover the whole globe. The scattering of single SF_6 profiles is large, as the noise error is in the order of 20% and increasing with altitude. Only averaged SF_6 profiles, where the noise is suppressed, led to a meaningful SF_6 database. In this study daily or monthly zonal averages are used.

In Figure 6.1 a time series of SF_6 over latitude at 25 km altitude produced from monthly zonal means is shown. SF_6 is increasing with time at all latitudes. Towards higher latitudes this increase is shifted in time, meaning that at higher latitudes the respective mixing ratios are reached at later times than in the tropics, as one would expect from the global circulation scheme. At high latitudes, especially in the southern polar stratosphere seasonal influences can be identified. Every year in late austral winter to austral spring tongues with very low SF_6 mixing ratios appear in the southern polar stratosphere. This can be explained by subsidence of very old air into the polar vortex, or even subsidence of SF_6 depleted air from the mesosphere. This effect is also indicated in the northern polar stratosphere, but much less pronounced. This is explained by the fact that the polar vortex is less stable and pronounced in the northern polar stratosphere and isolated subsidence inside the vortex does not occur

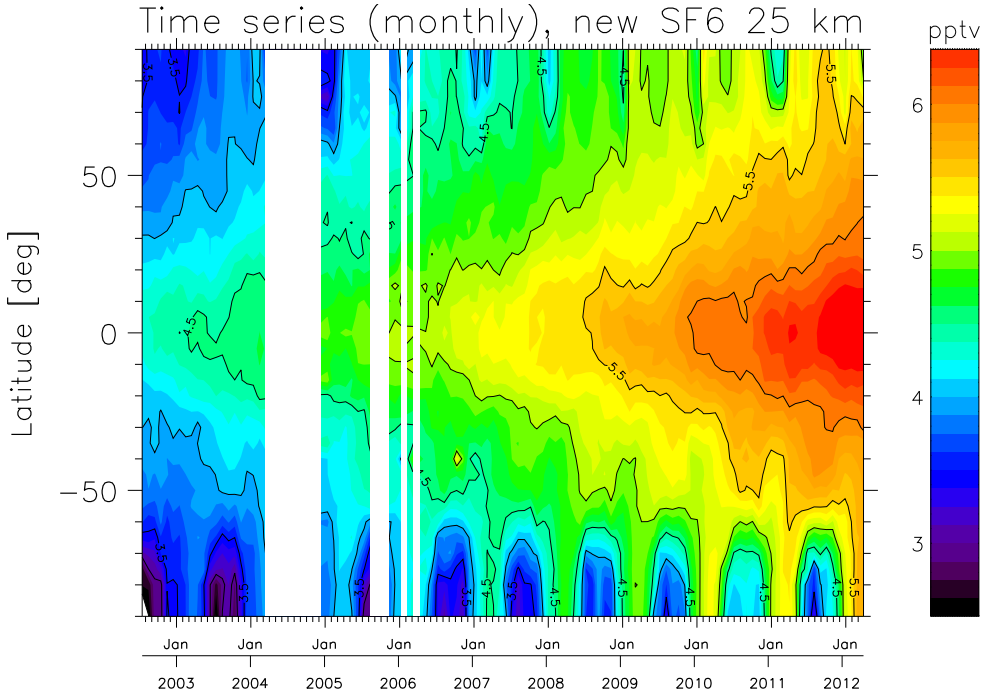

Figure 6.1: Time series of SF_6 monthly zonal means at 25 km. The white bars indicate data gaps where no measurements were available.

so often.

6.2 Conversion of SF_6 into age of air

For the calculation of AoA from SF_6 abundances a SF_6 reference curve is necessary. The theoretical concept of age of air as derived by Hall and Plumb [1994] (see Section 2.4) requires the knowledge of SF_6 mixing ratios at the entry point into the stratosphere, i.e. the tropical tropopause region, over a long period of time. As pointed out by Stiller et al. [2012] such a long-term observational data set is not available. Only ground-based observations can provide the necessary reference data. However, transport times from the surface to the tropical tropopause are somewhat uncertain and can amount from days or even hours (to the top of convection) to weeks or months (to the top of the tropical tropopause layer). Using surface data as a reference can imply a high bias in this order of magnitude on the AoA data. This has to be kept in mind when comparing MIPAS AoA distributions to model data, for which time 0 is set by tropopause crossing of the air parcel.

The SF_6 reference curve was constructed as described in Stiller et al. [2012] using NOAA/ESRL SF_6 data. For the period 1995 to November 2013 smoothed ground-

based global-mean combined flask and in-situ data [Hall et al., 2011] are used, while for times before 1995 a linear approximation from Hall et al. [2011] ($y = 0.125 + 0.215 \times (t - 1985)$) is applied. The reference curve is extended with a linear extrapolation using the average slope of the last 15 months of the ground based time series until June 2014 to deal with MIPAS SF_6 values slightly higher than the reference values at that certain time that can occur sporadically due to their random errors. The reference curve is shown in Figure 6.2.

The AoA is then calculated by mapping the measured SF_6 value measured at time t_{meas} on the reference curve (see Figure 6.2) and reading of the reference time t_{old}. The time difference $t_{meas} - t_{old}$, the so-called lag time, approximates the AoA. According to Hall and Plumb [1994] this lag time is only equivalent to the mean age of air when the used tracer is growing strictly linear, i.e. the reference curve has to be linear. Because our constructed reference curve appears to be slightly non-linear (see Figure 6.2), a correction is applied. Within an iterative procedure the reference curve is convoluted with a typical age spectrum G according to Equation 6.1, which is Equation 2.4 applied to SF_6. For the age spectrum G, which cannot be measured, assumptions have to be made. As in the study of Stiller et al. [2012], the Wald function described by Equation 2.13 (see Section 2.4) was used here. The procedure is started with the lag time as initial guess for the mean age Γ. Then $[SF_6]_{mod}$ is calculated using the reference curve and the Wald function G with the first guess for the mean age Γ:

$$[SF_6]_{mod} = \int_t [SF_6]_{ref}(t) \cdot G(\Gamma, \Delta, t) dt \tag{6.1}$$

The width Δ of the age spectrum is a function of the mean age scaled using an approximation by Waugh and Hall [2002] so that

$$\Delta^2/\Gamma = constant \approx 0.7 \tag{6.2}$$

$[SF_6]_{mod}$ is now the modelled SF_6 mixing ratio which corresponds to the first guess of the mean age Γ. Then the residual = $[SF_6]_{meas}$-$[SF_6]_{mod}$, the difference between measured and modelled SF_6, is evaluated and a Newtonian iteration is started, where a new guess for the mean age is derived from

$$\Gamma_{new} = t_{meas} - t_{new} \tag{6.3}$$

with

$$t_{new} = t_{old} + residual / \frac{d[SF_6]}{dt} \tag{6.4}$$

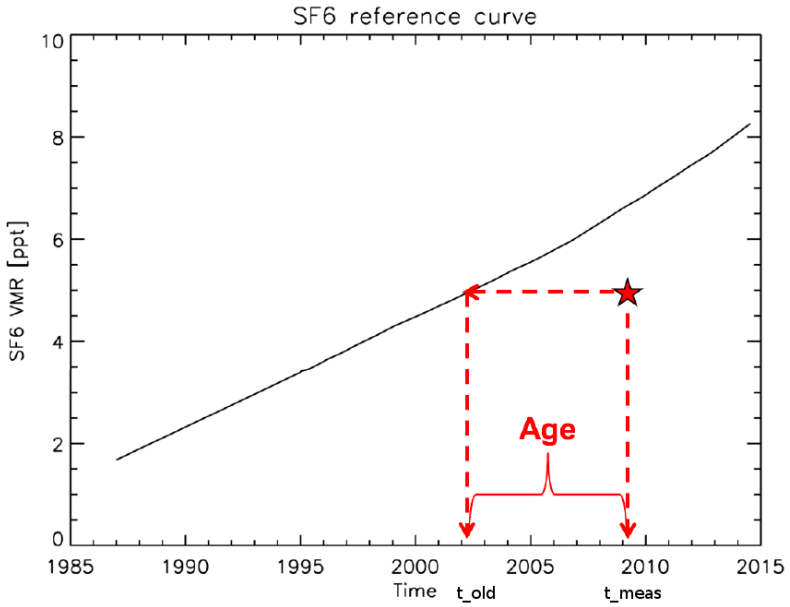

Figure 6.2: SF_6 reference curve

where $\frac{d[SF_6]}{dt}$ is the derivative of the SF_6 reference curve at time t_{old}. This procedure is iterated until convergence is achieved, i.e. when the residual is smaller than 0.01 pptv. The mean age found is the mean age where $[SF_6]_{mod}$ reproduces the measured SF_6 mixing ratio, $[SF_6]_{meas}$, and is considered a better estimate of the mean age than the lag time. If the age spectrum G was the real distribution of transit times of the sounded air parcel, this mean age would be the exact mean age of air corresponding to the measured SF_6 mixing ratio. However, because we have used an assumption on the shape of the age spectrum, there is still an uncertainty left. The atmosphere can certainly not be fully described by a one-dimensional model, which also does not include seasonal variations. In Section 8.2 the whole procedure of calculating the mean age is repeated using "real age spectra" simulated by the CLaMS model instead of Wald functions, and the effect on age of air distributions and trends is studied.

SF_6 is a stable tracer in the stratosphere. However, it has a mesospheric sink where the main SF_6 loss reaction is electron attachment (see Section 2.5). Every winter SF_6-depleted air from the mesosphere subsides into the polar vortex leading to "apparent ages" which are considerably larger than the true ages. This "overaging" is most pronounced in the polar vortices, where AoA derived from SF_6 can be greater by 2 or more years compared to CO_2-derived AoA [Waugh and Hall, 2002]. However, due to in-mixing of some of the vortex air into midlatitudes, the entire stratosphere is affected to a certain degree. This should be kept in mind when comparing AoA calculated from SF_6 abundances with AoA calculated from other tracers or model studies. Stiller et al.

[2012] estimated the global effect of overaging to about 0.08 years per year of age for the Southern Hemisphere and to about 0.04 years per year of age for the Northern Hemisphere.

Kovács et al. [2016] studied this effect on AoA by comparing the "reactive SF_6 tracer" including mesospheric loss processes with an inert SF_6 tracer in the Whole Atmosphere Community Climate Model (WACCM). They found AoA to be about 9% older in polar latitudes at 20 km compared to AoA derived from a passive SF_6 tracer, while at the same altitude in the tropics the effect was of minor importance on the derived AoA (0.5%).

6.3 Global distribution of age of air

The derived monthly zonal means of AoA have a precision in terms of the standard error of the means of 0.06–0.4 years for the RR-period and of 0.08–0.5 years for the FR-period. Most of the monthly means are composed of 500–800 single values when fully occupied.

The global distribution of the newly derived AoA data set is shown as average over all years for the four seasons in Figure 6.3. It reflects the general pattern of the BDC with young air rising in the tropics (isopleths bulging upward) and old air descending in the polar regions. If the BDC only consisted of the advective transport, oldest air would be found in the lower polar stratosphere. However, the AoA distribution reflects the combined effect of residual circulation and mixing, and therefore oldest air is found in the upper polar stratosphere. In addition the basic seasonality of the deep branch of the BDC is visible: The circulation is stronger during winter, which is especially demonstrated in older AoA found in the extratropics in the winter hemispheres due to stronger BDC-downwelling. The strongest upwelling in the tropics is expected during northern hemispheric winter [Rosenlof, 1995] and shifted into the respective summer hemisphere [see e.g. Seviour et al., 2012], which is reflected in the bulging of isolines of AoA.

Highest AoA values occur in the upper polar stratosphere in hemispheric winter to spring being particularly high in the Southern Hemisphere. This again can be explained by intrusion and subsidence of old upper stratospheric and mesospheric air into the polar vortex. Due to the mesospheric SF_6 sink, this mesospheric air appears even older than it actually is. However, these features even appear in model simulations when a "clock tracer" is used (e.g. Figure 4 in Ploeger and Birner [2016]).

In Figure 6.3 a clear hemispheric asymmetry is discernible in the AoA distributions:

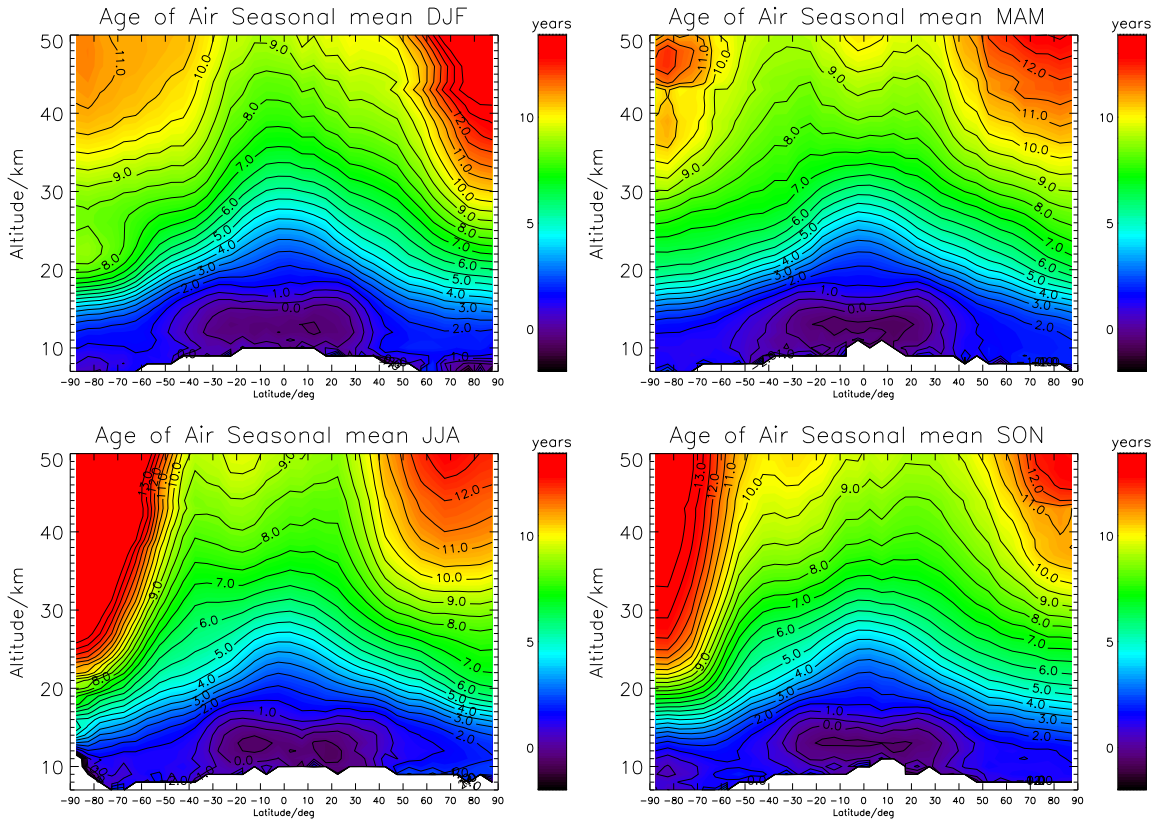

Figure 6.3: Zonal mean distribution of mean age of stratospheric air for the four seasons, derived by averaging MIPAS AoA data of all available years for the respective season.

In hemispheric winter, where highest AoA is observed, air is up to 5 years older around 25 km in the southern polar stratosphere than in the northern polar region. In contrast in hemispheric summer air is younger in the southern upper polar stratosphere than the respective region in the Northern Hemisphere, meaning that the seasonal cycle in AoA is stronger in the Southern Hemisphere than in the Northern Hemisphere.

In Konopka et al. [2015] AoA has been simulated by the CLaMS model, which is driven by ECMWF ERA-Interim reanalysis, for the period 2002-2012 covered by MIPAS. In their Figure 1 they found air to be always younger in the Northern Hemisphere than in the Southern Hemisphere during the same season in an altitude range from 5 to 20 km. This is confirmed with the MIPAS data between about 13 and 30 km in all four seasons. In winter and in spring air is always older in the Southern Hemisphere throughout the whole stratosphere. In addition, the vertical gradient of AoA is much larger in the Southern Hemisphere than in the Northern Hemisphere in the MIPAS data.

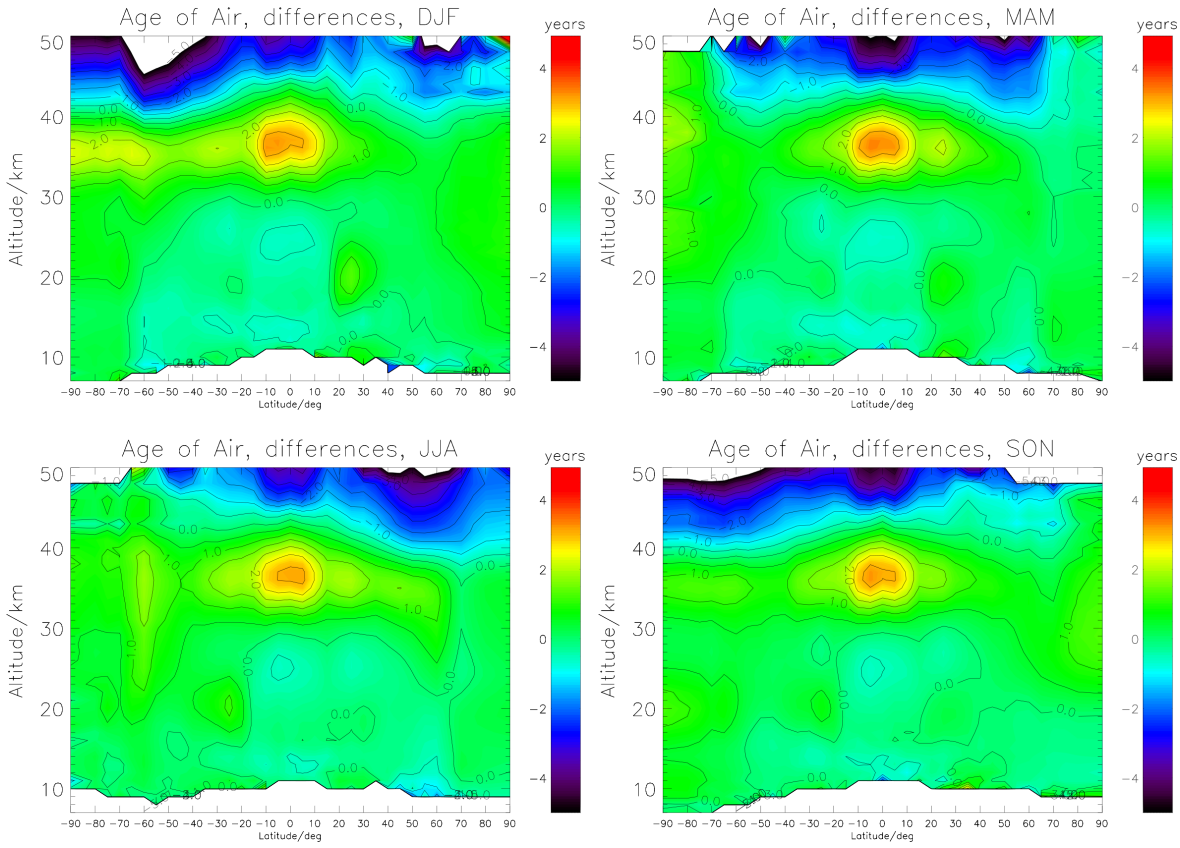

Figure 6.4: Differences of zonal seasonal mean distribution of mean age of stratospheric air to the previous data version averaged for the four seasons.

Ploeger and Birner [2016] further analysed the AoA in the CLaMS model and pointed out a further hemispheric asymmetry in the northern lower stratosphere during summer, when young air is mixed in (their Figure 4). There seems to be only a slight indication for this in the MIPAS data in fall (September to November).

The differences in the zonal monthly means of AoA to the previous data set, averaged over all years for the four seasons, are presented in Figure 6.4. The main difference to the old data set is that the local minimum of AoA in the tropics around 36 km is no longer present in the new data set. This feature of the old data set has been proven to be a retrieval artefact, which was eliminated by a refined treatment of continuum radiation (see Chapter 5). This artefact triggered an oscillation in lower layers which are no longer present in the new data set. Above 40 km, the air is now found to be younger at almost all latitudes, which appears to be more realistic. The old data version was reported to have a possible high bias of up to 2 years above 35 km, most pronounced at the summer pole due to the simplified approach concerning the non-LTE treatment of interfering CO_2 lines [Stiller et al., 2008]. The full non-LTE treatment used for the new

data set has removed this systematic uncertainty. In addition, part of the lower AoA in the upper stratosphere is attributed to the revised regularisation of the retrieval.

Chapter 7

Validation of SF_6 and age of air

7.1 Validation with cryosampler data

In this section MIPAS SF_6 measurements are compared to in-situ cryosampler measurements from 8 balloon flights conducted by the University of Frankfurt [see e.g. Engel et al., 2006]. At first the comparison is made for the 3 balloon flights performed during the MIPAS full resolution period (2002-2004). In the second subsection the relation of MIPAS reduced resolution measurements (2005-2012) to the remaining 5 in-situ SF_6 profiles are analysed.

7.1.1 MIPAS full resolution data

The 3 balloon flights during MIPAS FR-period were B39, B40 and B41. Flight B39 was performed on September 24 in 2002 over Southern France (mean latitude: 43.49°, mean longitude: 0.85°), while flight B40 and B41 collected air samples over Northern Scandinavia on March 6 (mean latitude: 67.13°, mean longitude: 25.52°) and June 9 (mean latitude: 67.86°, mean longitude: 20.02°) in 2003, respectively.

First of all MIPAS measurements have been selected, which match with the balloon-borne measurements in terms of location and time (in the following called collocated profiles). A "collocation criteria" of a distance of 1000 km and a time mismatch of 24 hours has been chosen (with respect to the tangent point of the MIPAS measurements). Secondly the MIPAS closest profile, according to a metric of $\sqrt{\text{distance[km]}^2 + 10000 \cdot \text{time difference[hours]}^2}$ was identified. As single MIPAS SF_6 profiles scatter a lot due to the large noise error, in addition the mean of all collocated profiles as well as the mean in the respective month and latitude bin was determined.

The MIPAS measurements exhibit a finite altitude resolution due to their averaging

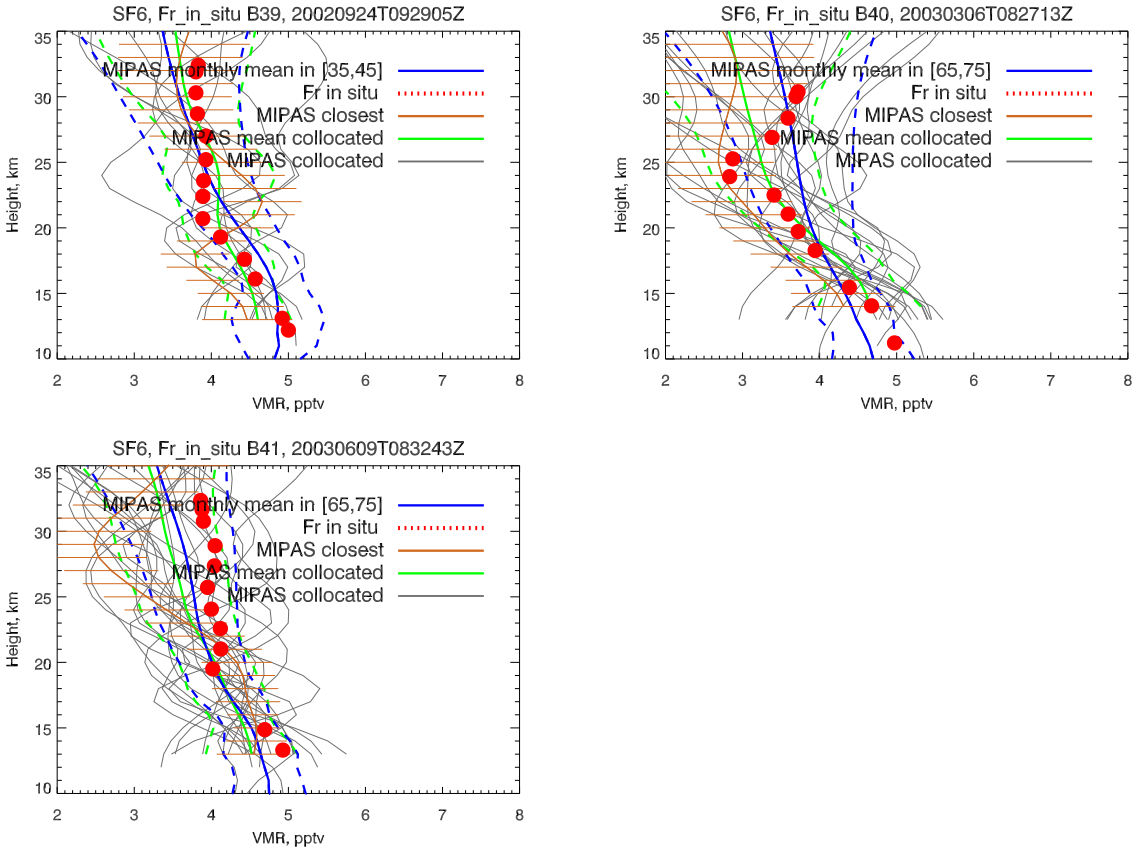

Figure 7.1: Validation of full resolution SF_6 profiles with cryosampler data: Three cryosampler profiles (red filled circles) and MIPAS profiles - all collocated (grey), closest collocations (orange), the mean profiles from all collocations (green) and the monthly mean profile (blue). The dashed lines indicate the standard deviations of the respective distributions of MIPAS profiles.

kernels (see Section 4.2.4). In order to carry out the comparison with the in-situ measurements properly, these cryosampler profiles would need to be adapted to the MIPAS altitude resolution, i.e. these profiles would have to be convoluted with the MIPAS averaging kernels. However, the convolution at each altitude requires a certain amount of values in the vicinity of each profile value, so that the uppermost and the lowermost values of the balloon profile would have to be neglected, which in turn, would further restrict the usable altitude range of the balloon profile. For these reasons the MIPAS profiles were compared to the original in-situ profiles.

The results of this validation are shown in Figure 7.1, where the balloon SF_6 profiles are depicted as red circles. The green profile represents the mean over all collocated profiles (thin grey lines), whereas the blue profile represents the monthly mean. The

dashed lines mark the respective standard deviations representing a measure of the variation of the MIPAS profiles including both noise error and natural variability. The closest MIPAS profile is shown in orange with error bars.

The cryosampler SF_6 mixing ratios from flight B39 match fairly well with the MIPAS mean collocated profile. The closest of all collocated MIPAS profiles only agrees with the in-situ profile within the error bars above 25 km, whereas it exhibits oscillations below.

The in-situ measurements from flight B40 show an almost linearly decreasing SF_6 profile, with two outliers around 25 km and increasing vmrs above. At this latitude during spring SF_6 vmrs can exhibit large variations depending on if the air is sampled inside or outside the polar vortex. Some of the MIPAS collocated profiles also increase with altitude above 25 km including MIPAS closest profile as well, corroborating this phenomenon. The MIPAS mean profiles, however, do not reflect this. The mean of all collocations fits well to the balloon-borne measurements up to an altitude about 22-23 km. The monthly mean profile (in blue) shows a weaker decrease with altitude leading to higher SF_6 vmrs in higher altitudes (which corresponds to younger age of air). This can be explained by the fact that the balloon-borne measurements took place at the beginning of March, the MIPAS monthly mean, which covers the whole month, could also include measurements of younger air (higher SF_6 vmrs) mixed in from lower latitudes, as the winter polar vortex breaks up during this time of the year. The closest MIPAS profile agrees with the in-situ profile within the error bars.

In contrast, the comparison of MIPAS with the third balloon profile (B41) hints at a possible low bias of MIPAS SF_6. The closest MIPAS profile exhibits significantly lower SF_6 values above 23 km and also both mean profiles.

Nevertheless, in all three cases the red in-situ measurements lie within the standard deviation of the distributions of MIPAS collocated profiles and profiles in the respective month (with exception of the two outliers around 25 km of flight B40). This means that the red profile could be understood as a member of the respective ensembles of MIPAS profiles, which demonstrates that MIPAS measurements and the in-situ measurements by the cryosampler are compatible.

7.1.2 MIPAS reduced resolution data

Figure 7.2 shows the equivalent comparison of MIPAS SF_6 data with the 5 cryosampler profiles, which sampled air masses during the MIPAS RR-period (flight B42-B46). B42, B43 and B44 were launched from Teresina, Brazil, B45 and B46 took place near Kiruna,

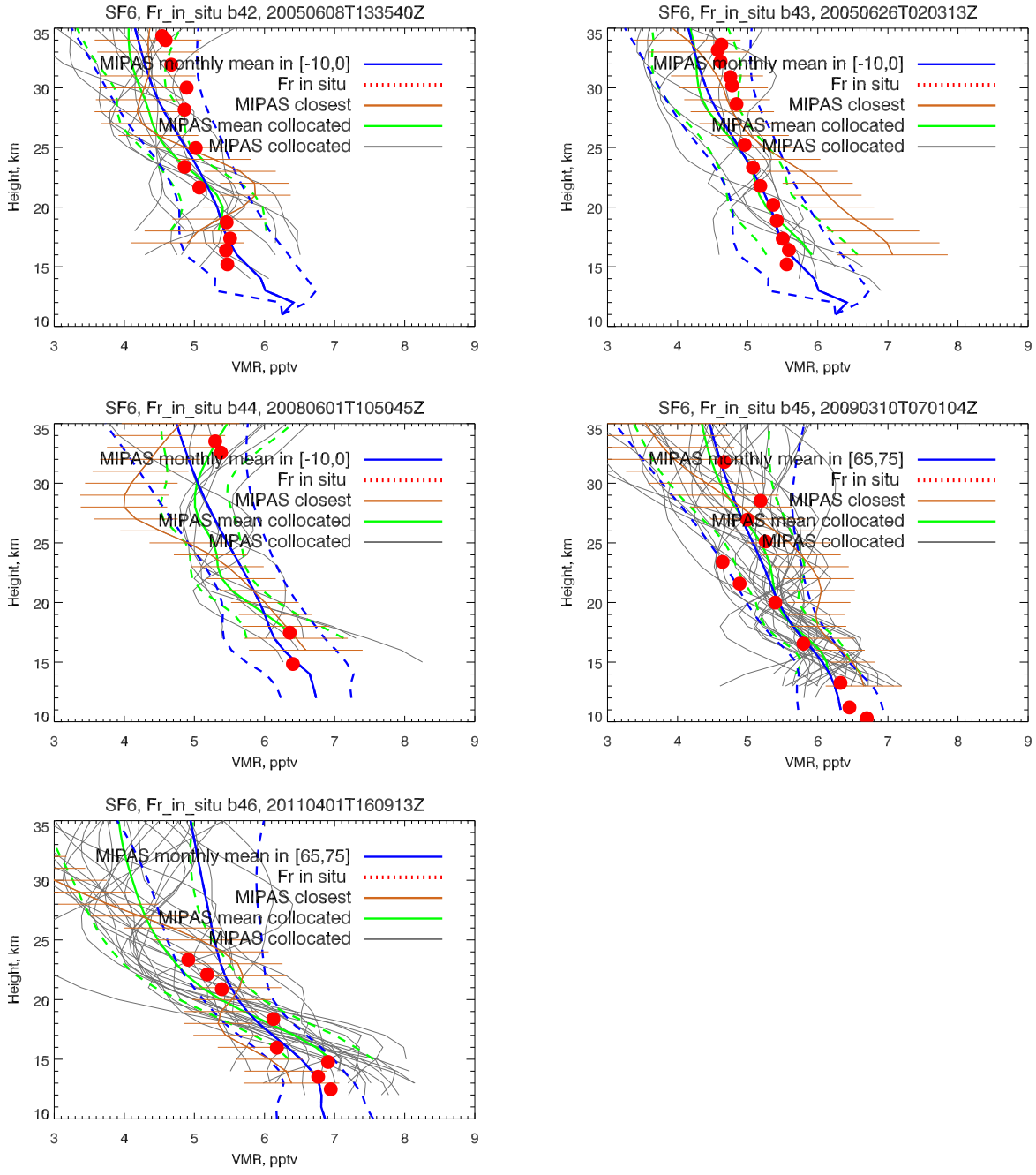

Figure 7.2: Validation of reduced resolution SF_6 profiles with cryosampler data: Five cryosampler profiles (red filled circles) and MIPAS profiles - all collocated (grey), closest collocations (orange), the mean profiles from all collocations (green) and the monthly mean profile (blue). The dashed lines indicate the standard deviations of the respective distributions of MIPAS profiles.

Sweden.

Flight B42 (mean latitude: -5.22°, mean longitude: -44.48°) also shows that MIPAS SF_6 vmrs are lower than the in-situ measurements above 25 km, since the mean profiles as well as closest of MIPAS collocated profiles exhibit lower values. Below that altitude the agreement of the MIPAS mean profiles with the balloon-borne measurements is fairly good, whereas the closest MIPAS profile has oscillations with a maximum around 20-23 km.

SF_6 mixing ratios of MIPAS closest profile in comparison with the in-situ data of flight B43 (mean latitude: -5.00°, mean longitude: -42.90°) are larger below 24 km. However, the MIPAS mean profiles fit well up to an altitude of 25 km. Above MIPAS mean profiles are again biased low. The closest collocated profile is an outlier of the ensemble of collocated profiles itself below 25 km.

Balloon flight B44 (mean latitude: -5.10°, mean longitude: -43.00°) only yields 4 SF_6 measurements, 2 at the lower and 2 at the upper end of the profile, respectively. The upper two agree well with the MIPAS mean over all collocated profiles, but are at the edge of the error bars of MIPAS closest profile. The lowest data point at approximately 15 km is out of range of the collocated profiles, but still coincides with the MIPAS monthly mean. The fourth in-situ value at approximately 17 km matches both the mean collocated and the value of MIPAS closest.

The profile B45 shows good agreement with MIPAS closest collocated profiles, as well as with the mean profiles. There are two very low values between 20 and 25 km in the balloon profile which were also to be found outliers in other tracers, e.g. the methane profiles as shown in Laeng et al. [2015]. This hints towards a tongue of air masses that had subsided before. This fine structure cannot be resolved by MIPAS.

The comparison between in-situ measurements of balloon flight B46 with MIPAS yields good agreement in general. There is a strong vertical gradient both in MIPAS and in cryosampler profiles.

In all five cases the red in-situ measurements lie within the standard deviation of the MIPAS profiles of the month and in most cases also within the standard deviation of the collocated profiles. This means that the red profile could be understood as member of the ensemble of MIPAS profiles in the corresponding month and of the collocated profiles, respectively, which again demonstrates that MIPAS measurements and the in-situ measurements by the cryosampler are compatible.

7.2 Validation with tropospheric in-situ measurements

In this section MIPAS SF_6 measurements are compared to in-situ measurements from various ground based stations. Figure 7.3 shows the time series of SF_6 measured in-situ at Mauna Loa, Hawaii (19.539°N, 155.578°W, elevation: 3397 m, in red) compared with MIPAS SF_6 measurements zonally averaged in the latitude interval 17.5°N to 22.5°N (in black) at different altitudes over the total MIPAS reduced resolution time period.

The lowest altitude where a considerable amount of MIPAS measurements were found is 11 km. Data gaps are due to contamination by clouds originating from high-reaching and strong convection in the tropics. Below 11 km no cloud-free observations are available. In Figure 7.3 a MIPAS measurements are shown together with their linear fit which appears to be slightly positively biased compared to the in-situ measurements in red. But there is a remarkable accordance in the slope of the SF_6 increase. Similar results are observed for altitudes 12 and 14 km (Figures 7.3 b and c) whereas Figure 7.3 d shows a slight negative bias of the MIPAS data. In 17 and 18 km the MIPAS negative bias gets even larger (Figures 7.3 e and f). At these altitudes MIPAS measurements are expected to be already in the stratosphere where the air is older than the tropospheric air measured at the ground due to slow transport through the tropopause. This time lack explains the negative bias between MIPAS and the ground-based measurements. Figures 7.3 e and f also exhibit a seasonal cycle in the MIPAS data which could be a result of the seasonal cycle in the tropopause height. To investigate this issue the tropopause height was determined from ECMWF temperature data using the WMO definition for the tropopause as being the lowest point (above the 500 mb level) for which the temperature lapse rate decreases to 2 K/km or less, and for which the average lapse rate from this level to any point within the next 2 km does not exceed 2 K/km [Craig, 1965]. The tropopause height was determined for every ECMWF temperature profile and averaged daily and zonally. The result is shown in Figure 7.4 together with the MIPAS daily deviation from its linear fit in arbitrary units. The correlation between both curves can be clearly seen. The tropopause height oscillates around 17 km so the highest amplitude of the seasonal cycle of the MIPAS measurements should be expected there which is shown in Figure 7.4 (right). The tropopause height has a maximum in boreal winter and a minimum in late boreal summer which is in agreement with findings of Reid and Gage [1981]. MIPAS SF_6 at a constant altitude in the tropopause region is typically high for high tropopause altitudes when tropospheric air is sounded, and low for low tropopause altitudes when

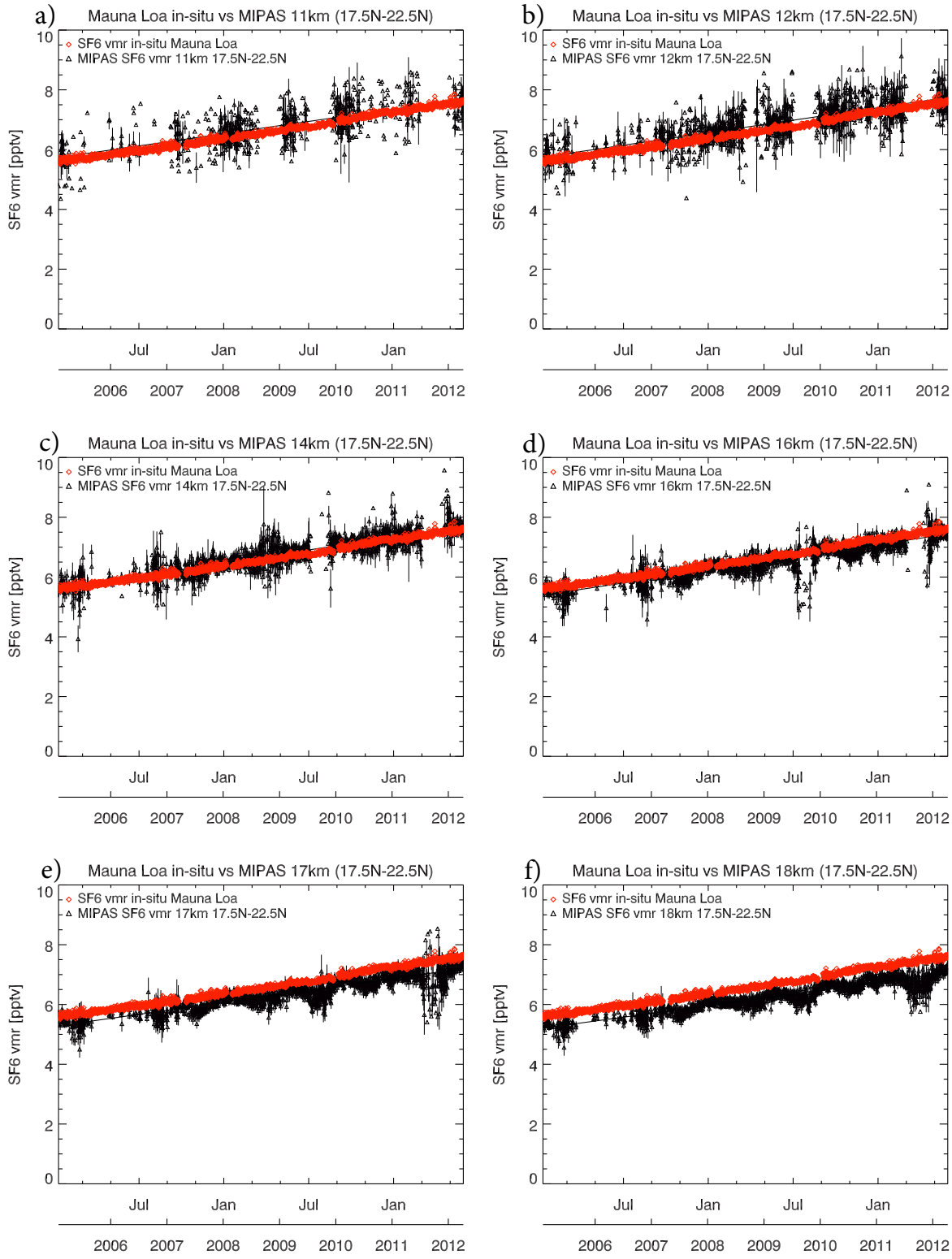

Figure 7.3: Time series of MIPAS SF_6 daily zonal means (17.5°-22.5°N, in black) at different altitudes compared to ground-based in-situ measurements at Mauna Loa (red)

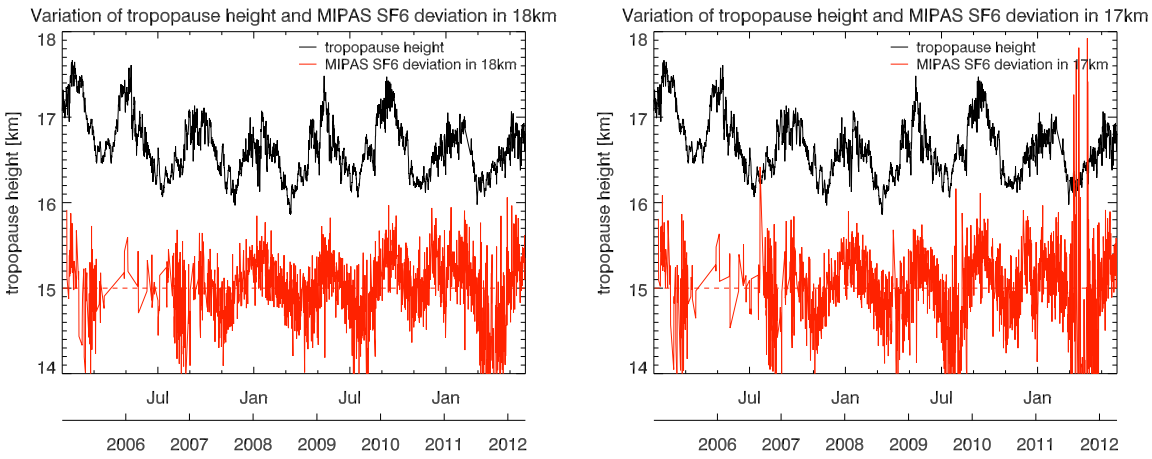

Figure 7.4: Tropopause height and MIPAS SF_6 deviation at 18 km (left) and 17 km (right) for the northern tropics.

stratospheric air is sounded.

The situation in the Southern Hemisphere is different. Figures 7.5 a to g show the same study for the comparison of MIPAS measurements at various altitudes with a ground station in the southern tropics at Cape Matatula in American Samoa (14.3°S, 170.6°W, elevation: 77 m). At 10 km (Figure 7.5 a) the agreement is fairly good, even though the slope of the fit of MIPAS measurements and the in-situ measurements is slightly different. At the altitudes 11 to 14 km (Figures 7.5 b to d) MIPAS values appear to be higher than the surface based measurements. It is a well known fact that SF_6 abundances are higher in the Northern Hemisphere than in the Southern Hemisphere (at the surface), just because there are more sources in the north and a interhemispheric mixing barrier exists. At higher altitudes (in the free troposphere) air masses could be already affected by interhemispheric mixing. This could be a reason why MIPAS measurements show higher values than the ground based station. The same behaviour was found for HCFC-22 [Chirkov et al., 2016] (their Figure 19). This was explained there by MIPAS observing the outflow of northern hemispheric tropical air above the convection. In 16 km air masses are already near the tropopause in the Tropopause Transition Layer (TTL), where upward transport is very slow. Therefore there exists a time lag between MIPAS measurements and the ground-based measurements and this compensates the bias so that both measurements fit well again. In Figures 7.5 f and g MIPAS measurements are again low biased at altitudes 17 and 18 km, respectively and also show a seasonal cycle but much less pronounced than in the Northern Hemisphere.

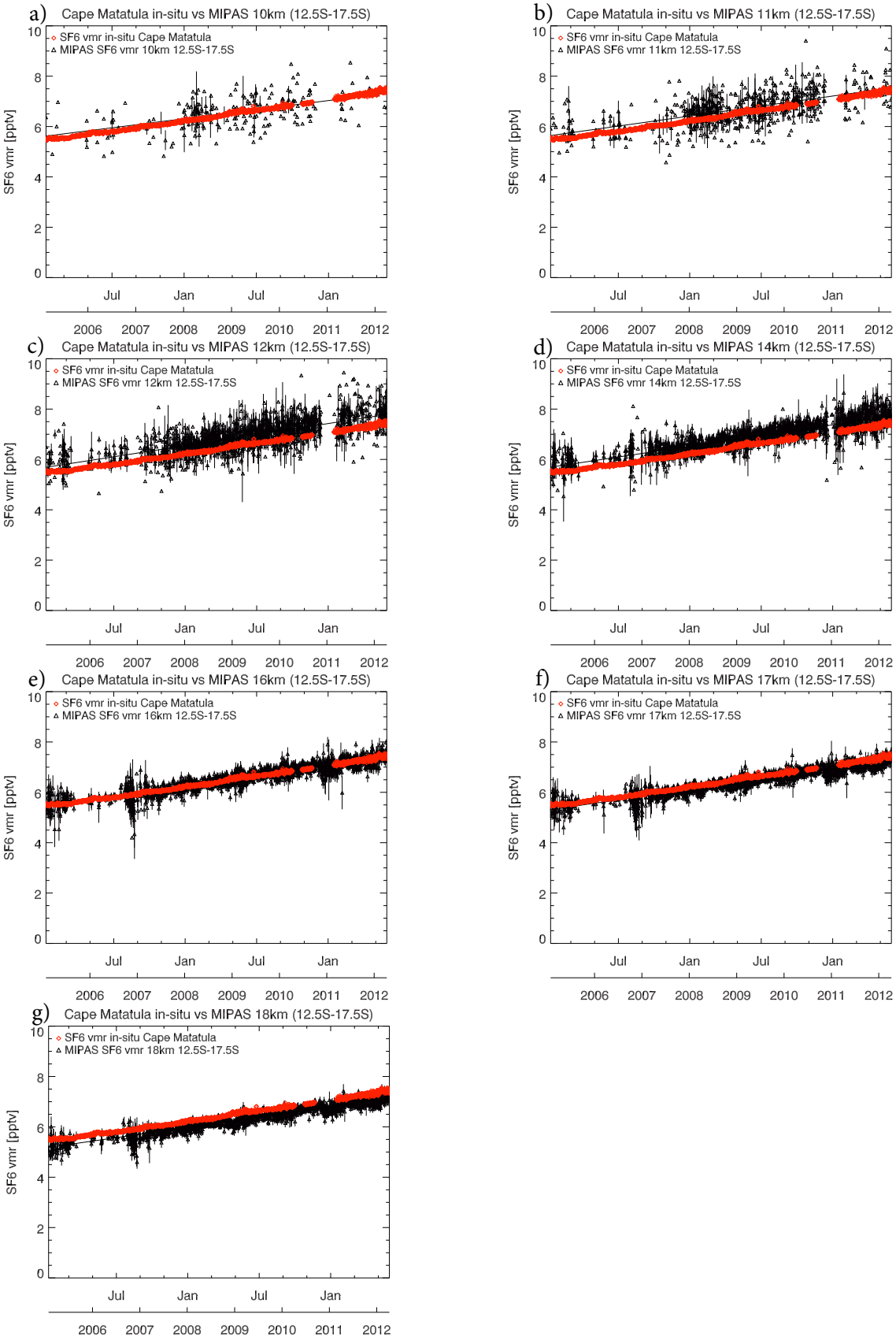

Figure 7.5: Time series of MIPAS SF_6 daily zonal means (12.5°-17.5°S, in black) at different altitudes compared to ground-based in-situ measurements at Cape Matatula (red)

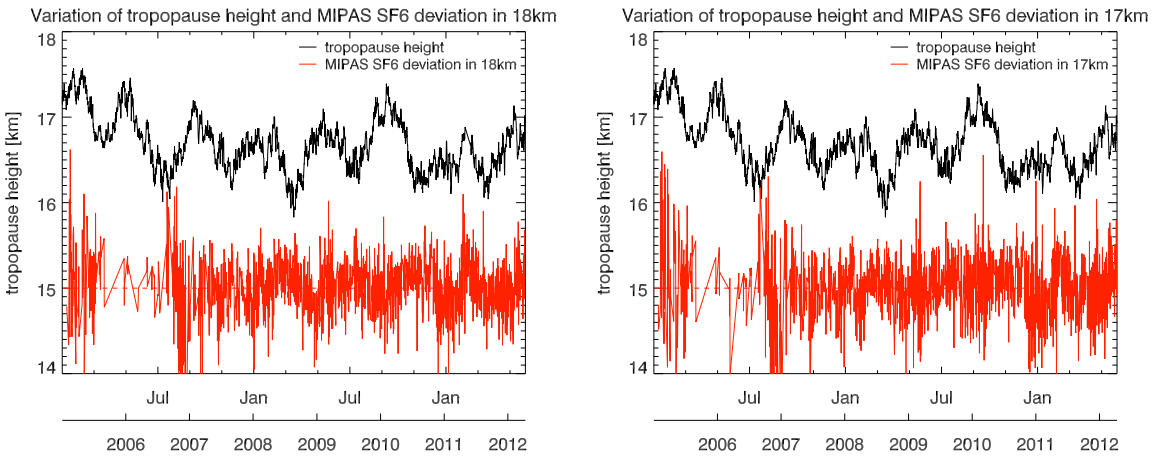

Figure 7.6: Tropopause height and MIPAS SF_6 deviation at 18 km (left) and 17 km (right) for the southern tropics.

The tropopause height time series was inferred from EMCWF temperature using the same procedure as for Mauna Loa and is plotted together with the MIPAS deviation in Figure 7.6. The phase of the seasonal cycle in tropopause heights remains the same as for the Northern Hemisphere which was also observed by Reid and Gage [1981], whereas the MIPAS deviation appears to be off-phase now, with maxima in southern winter. The seasonal cycle of the MIPAS deviation could also be affected by a seasonal variation in tropical upwelling, which is stronger in hemispheric winter. This could explain why the pattern of a seasonal variation in MIPAS deviation is more pronounced in the Northern Hemisphere where seasonal cycle of tropopause height and tropical upwelling are in phase whereas in the Southern Hemisphere they seem to compensate each other.

7.3 Validation with ACE-FTS

In this section MIPAS SF_6 results are compared to SF_6 measurements performed by the Atmospheric Chemistry Experiment (ACE-FTS). ACE is also a Fourier Transform Spectrometer (FTS) which is the main instrument on the SCISAT-1 satellite. As opposed to MIPAS, ACE-FTS is a solar occultation instrument, which looks directly into the sun and can only take measurements during sunrise and sunset. This implies that measurements are by far more sparse than the MIPAS measurements. However, the signal-to-noise ratio is far higher.

Figure 7.7 shows the comparison between ACE-FTS and MIPAS for the whole RR-period. On the left panel, averaged profiles for MIPAS and ACE-FTS are shown, whose single profiles matched a collocation criteria of 500 km and 5 hours, which corresponds to about 8000 MIPAS-ACE-FTS pairs. The error bars indicate the average errors of the single SF_6 profiles. MIPAS exhibits lower values between 20 and 30 km than ACE-FTS, which means that age of air would be older than observed by ACE-FTS. The plot of the averaged difference between MIPAS and ACE-FTS (middle panel) reveals that the difference is significant at all altitudes, as the denoted error is the standard error of the mean difference (standard deviation divided by $\sqrt{8000}$). The standard deviation of the difference can be seen on the right panel representing the variation of the difference. The standard deviation of the difference is always smaller than the combined error of ACE-FTS and MIPAS which implies that the errors for ACE-FTS or MIPAS are overestimated. Probably the stated errors for ACE-FTS are too large.

The comparison is now further investigated for six 30°-latitude bins and for the four seasons. Figure 7.8 to Figure 7.13 show averaged MIPAS and ACE-FTS profiles for the tropics, the midlatitudes and the polar regions, first for the Northern Hemisphere and second the respective regions for the Southern Hemisphere.

Most of the ACE-FTS measurements are located in the polar regions (see Figure 7.10 and Figure 7.13), so most of the MIPAS-ACE-FTS pairs are found in these two latitude bands. The picture is quite similar to the total comparison in Figure 7.7: MIPAS is biased low in the middle stratosphere with biggest differences in hemispheric summer and smallest differences in hemispheric autumn.

For the northern and southern midlatitudes (Figures 7.9 and 7.12) most accordance between MIPAS and ACE-FTS is found in hemispheric winter, still MIPAS exhibits a low bias compared to ACE-FTS in the middle stratosphere in all four seasons. The statistics for the tropics is poor, as ACE-FTS measurements are very sparse.

The distributions of SF_6 values measured by MIPAS and ACE-FTS as a histogram

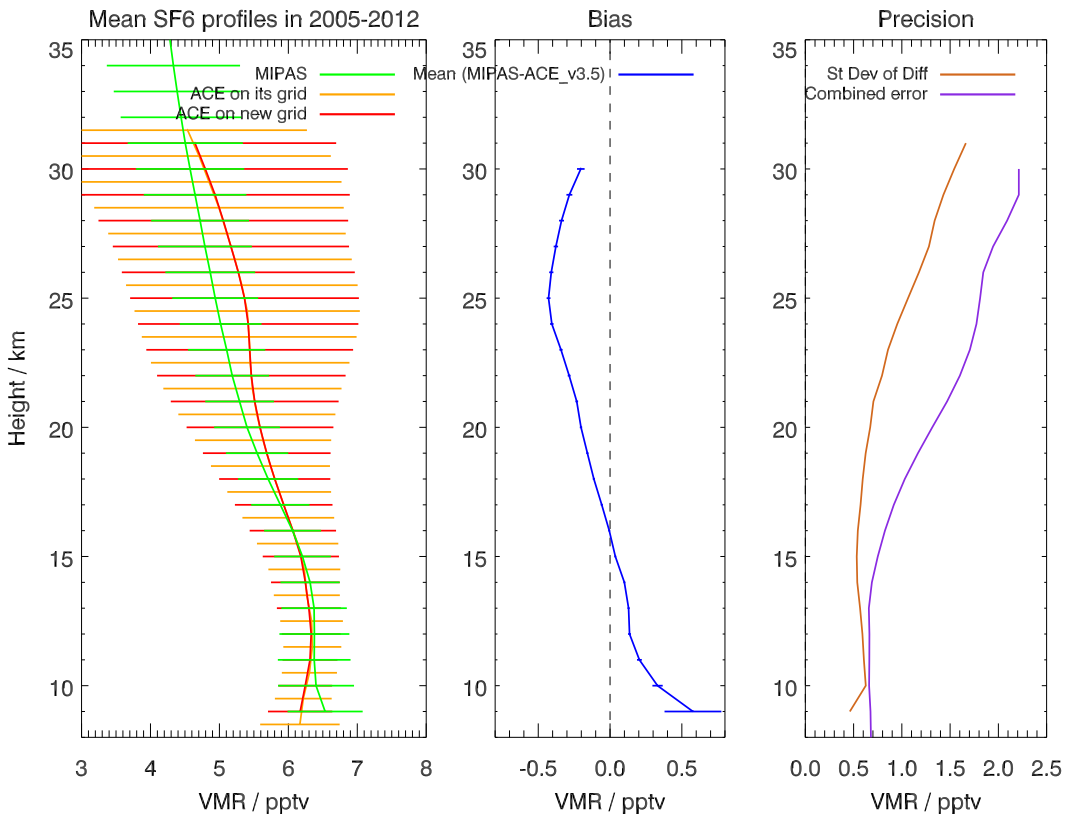

Figure 7.7: Comparison between ACE-FTS and MIPAS SF_6 profiles: Left panel: Average profiles of MIPAS (green) and ACE-FTS on its own grid (orange) and interpolated on the MIPAS grid (red) together with the respective average errors of a single profile. Middle panel: Averaged difference between MIPAS and ACE-FTS with the standard error of the mean difference. Right panel: Standard deviation of the difference and combined error.

are shown in Figure 7.14 for two selected altitudes (18 and 25 km). At 25 km the largest difference between MIPAS and ACE-FTS is found (compare with Figure 7.7), whereas 18 km is just above the best agreement of the two satellite instruments. For both data sets, the distribution is shifted towards lower SF_6 values when comparing the left with the right panel, as air is getting older with increasing altitude. This effect is more pronounced in the MIPAS data due to the steeper gradient in the SF_6 average profile. Also the width of the distributions is greater at 25 km than at 18 km for both instruments, meaning that the scatter of SF_6 values is larger. This was already observed in the MIPAS data in Section 5.9.2. At 18 km the MIPAS and the ACE-FTS distribution almost peak at the same SF_6 value, as their mean difference is very small, but the ACE-FTS distribution is narrower than the MIPAS one. As the denoted average error is larger for ACE-FTS than for MIPAS, this is a further indication that ACE-FTS errors are overestimated. Comparing the MIPAS distribution at 25 km with

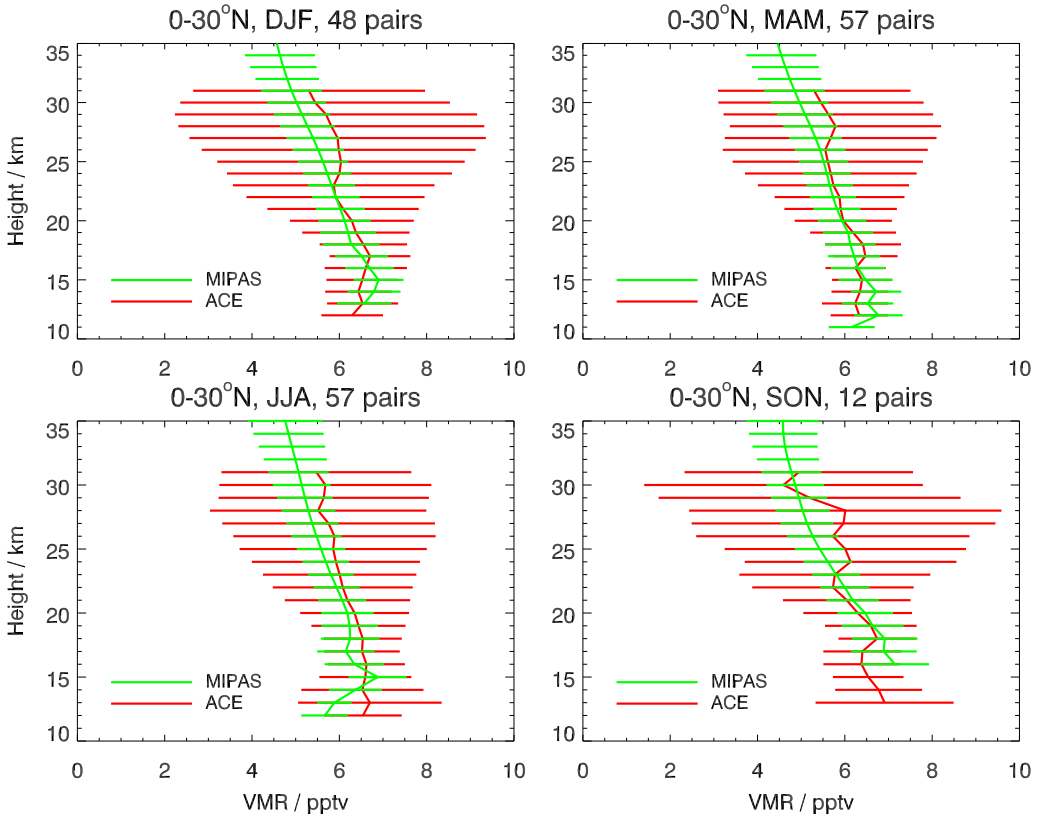

Figure 7.8: Average profiles of MIPAS (green) and ACE-FTS (red) together with the respective average errors of a single profile for the northern tropics in the four seasons.

the one from ACE-FTS, the ACE-FTS distribution is shifted towards higher values, as expected from looking at the averaged profiles (see Figure 7.7).

Figure 7.15 shows the correlation scatter plot between MIPAS and ACE-FTS. It reflects in principle the findings already discussed with Figure 7.7 (middle panel): The vertical gradient is stronger in the MIPAS data compared to the ACE-FTS data.

Now the ACE-FTS monthly averaged profile is compared to cryosampler in-situ measurements from balloon flight B45 in the relevant altitude band 65°-75°N in Figure 7.16. For all other balloon flights no ACE-FTS measurements were available. For illustration the MIPAS averaged profile is also displayed. Because ACE-FTS data are far more sparse than MIPAS data the ACE-FTS profile appears not as smooth as the MIPAS profile. It can be seen that ACE-FTS, MIPAS and the in-situ data agree well: The balloon data points are found to be within the standard deviation of ACE-FTS and MIPAS (with exception of the two very low values, refer to Section 7.1), meaning that they could be part of the ACE-FTS and MIPAS ensemble, respectively.

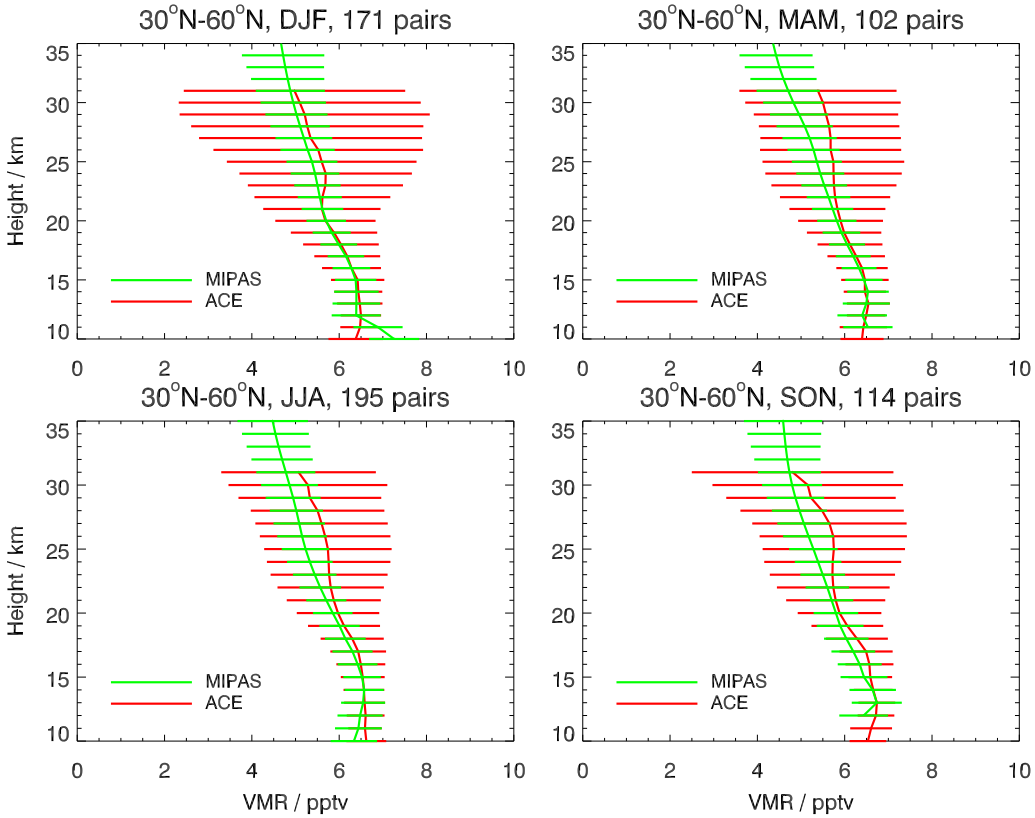

Figure 7.9: Same as Figure 7.8 but for the northern midlatitudes

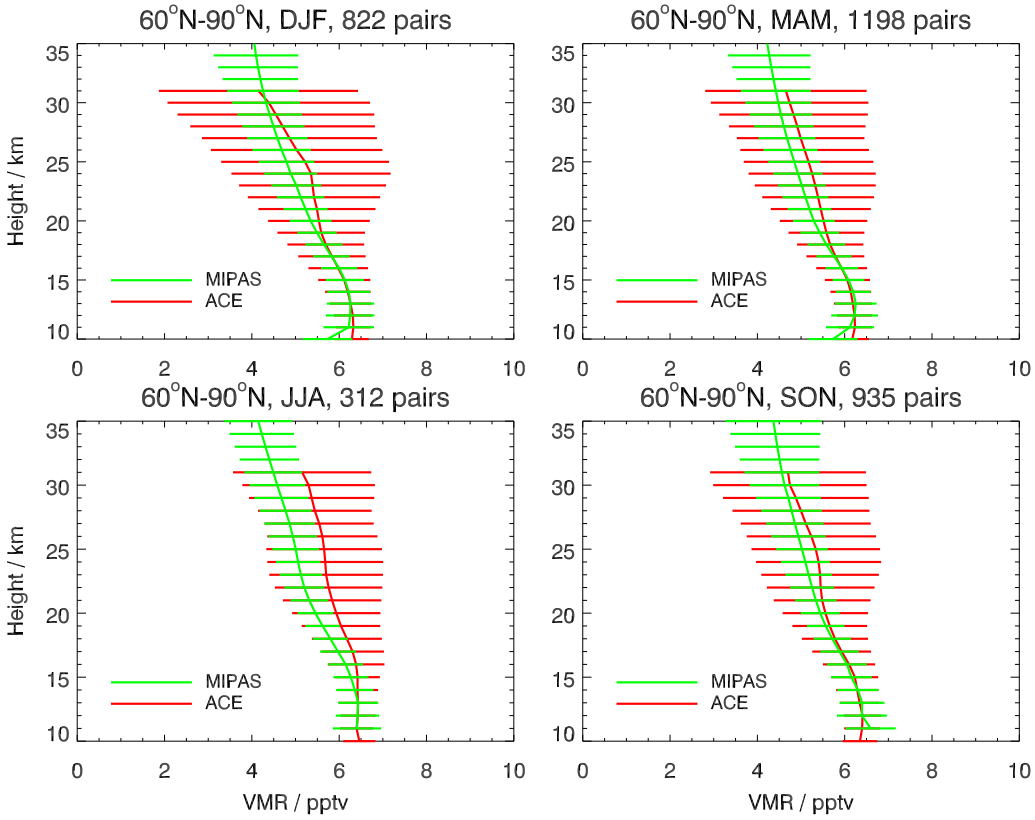

Figure 7.10: Same as Figure 7.8 but for the northern polar region

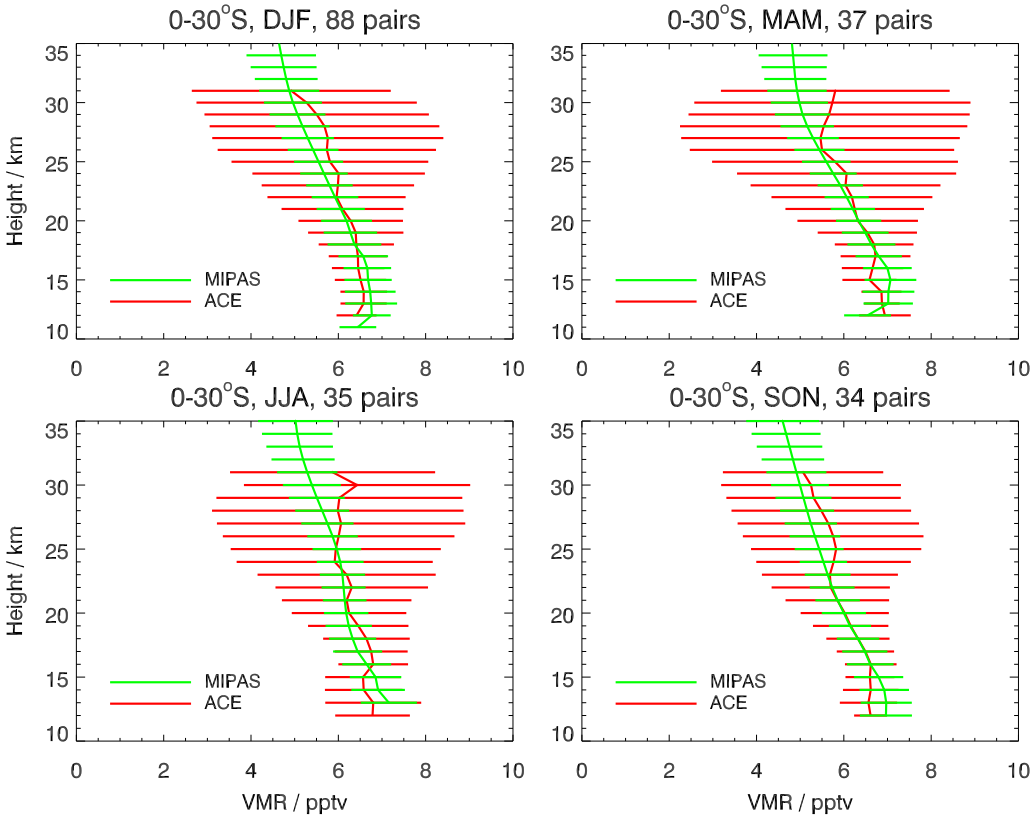

Figure 7.11: Same as Figure 7.8 but for the southern tropics

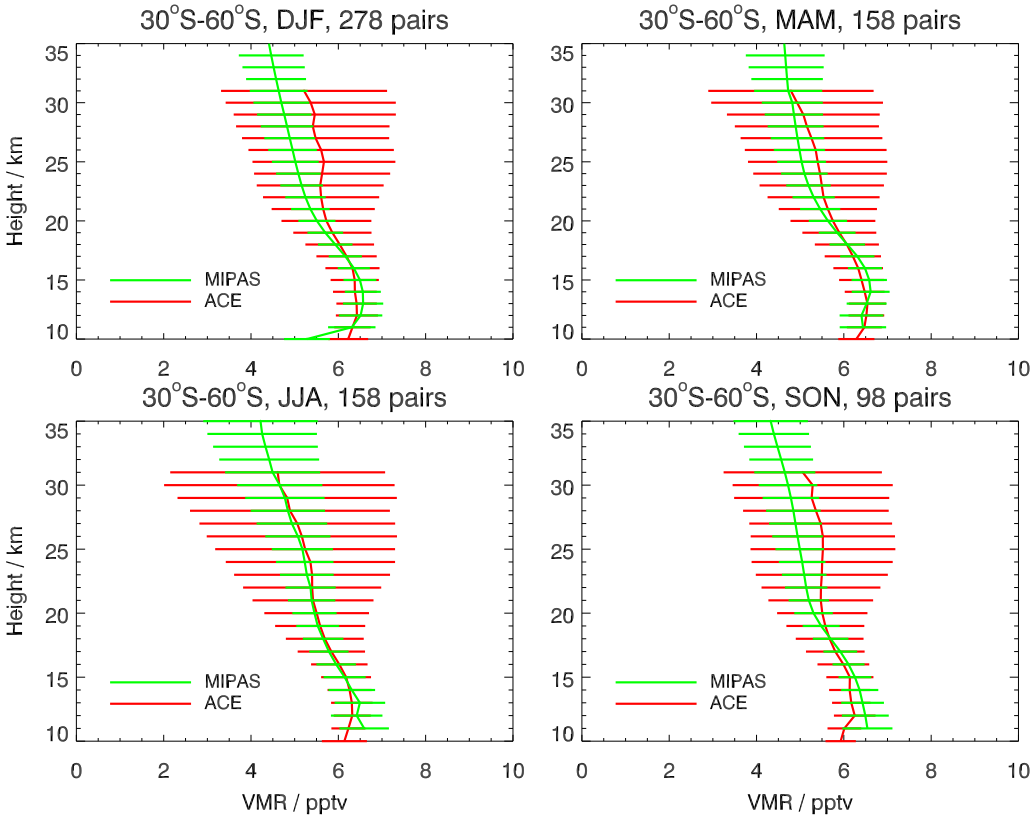

Figure 7.12: Same as Figure 7.8 but for the southern midlatitudes

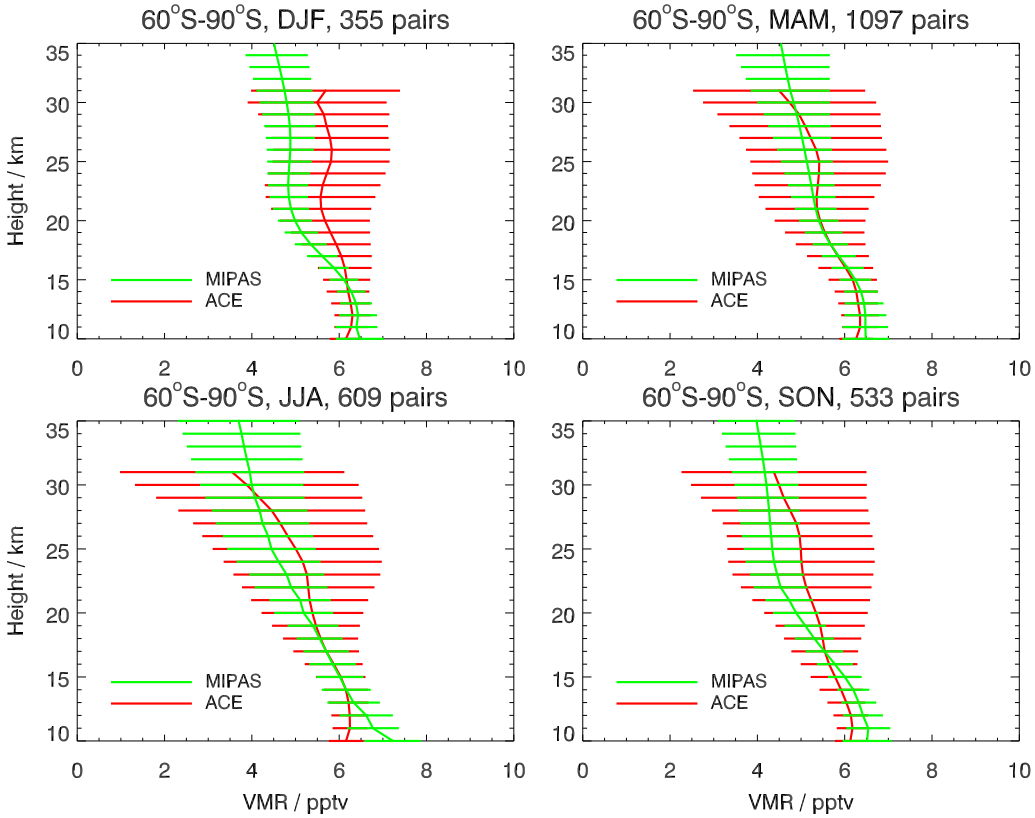

Figure 7.13: Same as Figure 7.8 but for the southern polar region

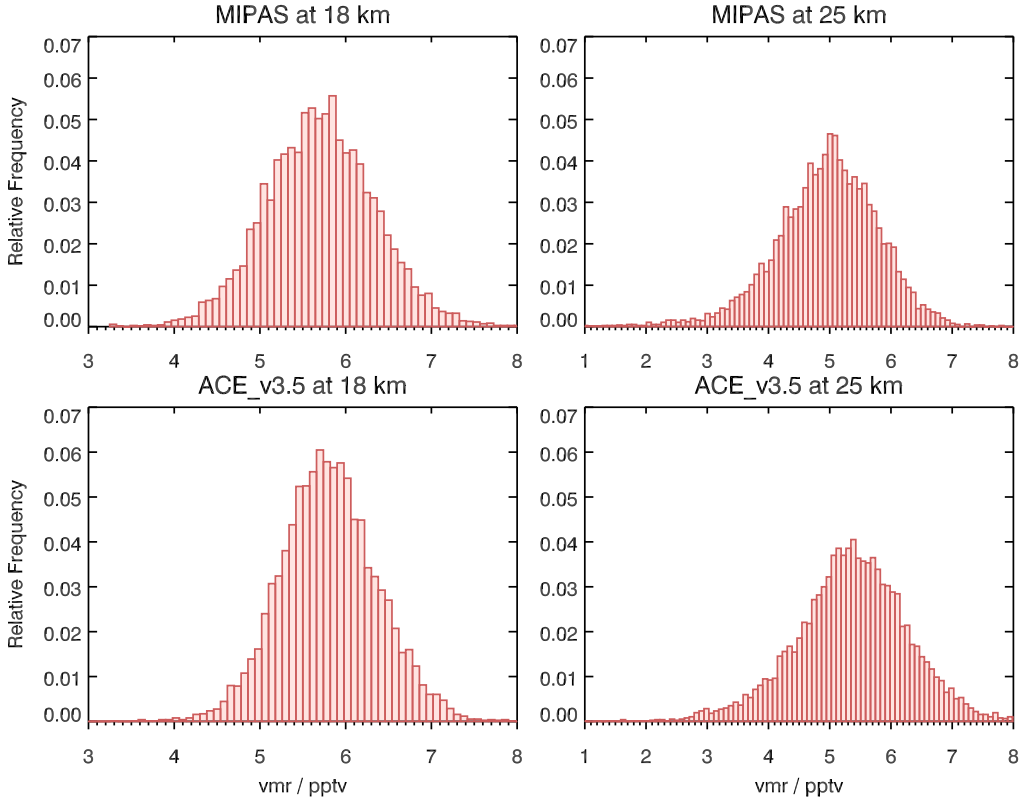

Figure 7.14: Distributions of SF_6 values measured by MIPAS and ACE-FTS at 18 and 25 km

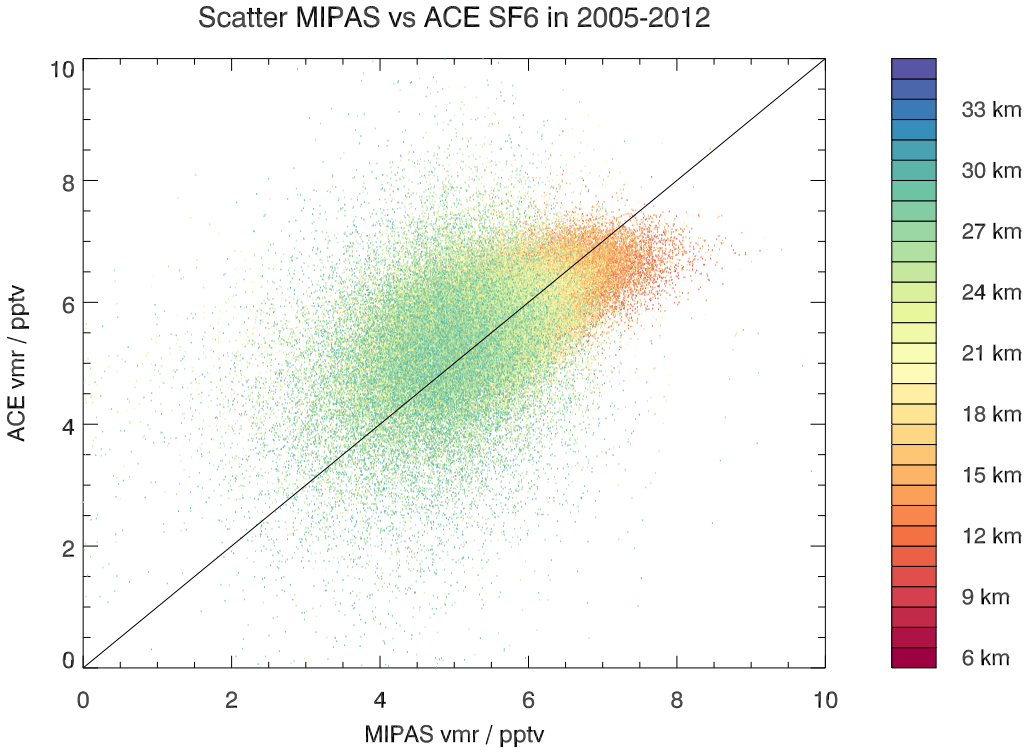

Figure 7.15: Correlation scatter plot between MIPAS and ACE-FTS for the total altitude range

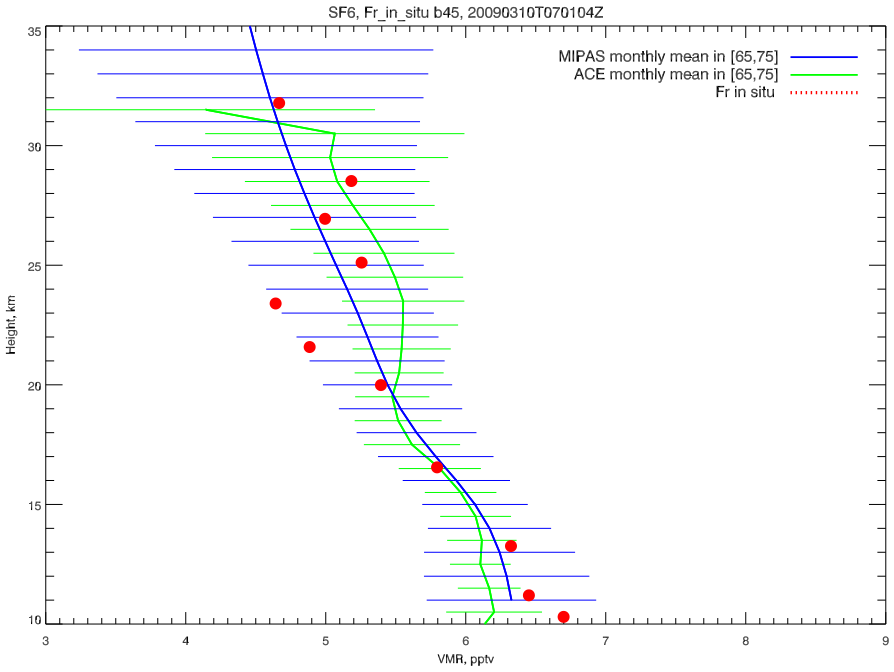

Figure 7.16: MIPAS and ACE monthly mean profiles in comparison with in-situ measurements of balloon flight B45

7.4 Comparison of MIPAS age of air with airborne measurements

Among studies of AoA (e.g. Diallo et al., 2012; Konopka et al., 2015; SPARC CCMVal, 2010; Stiller et al., 2012) it became a standard for validation of measured or modelled AoA to compare with earlier airborne measurements from the 1990s as published by Waugh and Hall [2002] and Hall et al. [1999]. In Figure 7.17 the new MIPAS monthly zonal means of AoA are compared with these airborne measurements. Figure 7.17 shows the latitudinal cross section of the new MIPAS AoA at 20 km for selected months together with the total AoA range covered by all monthly mean data from MIPAS as derived from the minimum and maximum value for each latitude bin (shaded in grey), and the AoA derived from airborne measurements of SF_6 and CO_2. The AoA from CO_2 refers to CO_2 observations at the tropical tropopause, so it might exhibit a slight low bias compared to the SF_6-derived AoA measurements. Overaging (see Section 6.2) of the SF_6-derived AoA values could also be a reason.

As with the previous version of MIPAS AoA discussed in Stiller et al. [2012] (their Figure 4), the agreement of MIPAS AoA with the earlier airborne measurements is excellent in the northern and southern midlatitudes. Overall the comparison turns out to be quite similar to the one in Figure 4 in Stiller et al. [2012]: MIPAS AoA is higher in the tropics with an AoA of about 2 years at 20 km, maybe slightly lower than in the previous comparison. The negative peak of low MIPAS AoA at about 30° N is no longer present in the new version of the figure. This peak was due to retrieval artefacts in previous temperature data. The spread of MIPAS AoA in the tropics is also lower. At high latitudes MIPAS AoA is higher than the airborne observations, however, the error bars of the airborne measurements still overlap with the range of the MIPAS observations. The spread of MIPAS data at high latitudes is very large, especially in the southern polar stratosphere, and is in agreement with high amplitudes found in the seasonal cycle (see Section 8.3). The hemispheric asymmetry in AoA, already noted in Section 6.3, is clearly visible also at 20 km. By comparing the latitudinal cross sections of MIPAS AoA with the aircraft data one has to keep in mind that these data were observed in the 1990s, whereas MIPAS AoA represent the decade from 2002 to 2012. We cannot expect that AoA estimates from different decades fit perfectly together, especially in the tropics where temperature changes have been reported e.g. by Randel et al. [2006]. The AoA gradients at the subtropical mixing barriers are also smaller in the MIPAS data, which could be a hint to a weakening of the mixing barriers, as proposed by Stiller et al. [2012], which would also explain the higher ages in

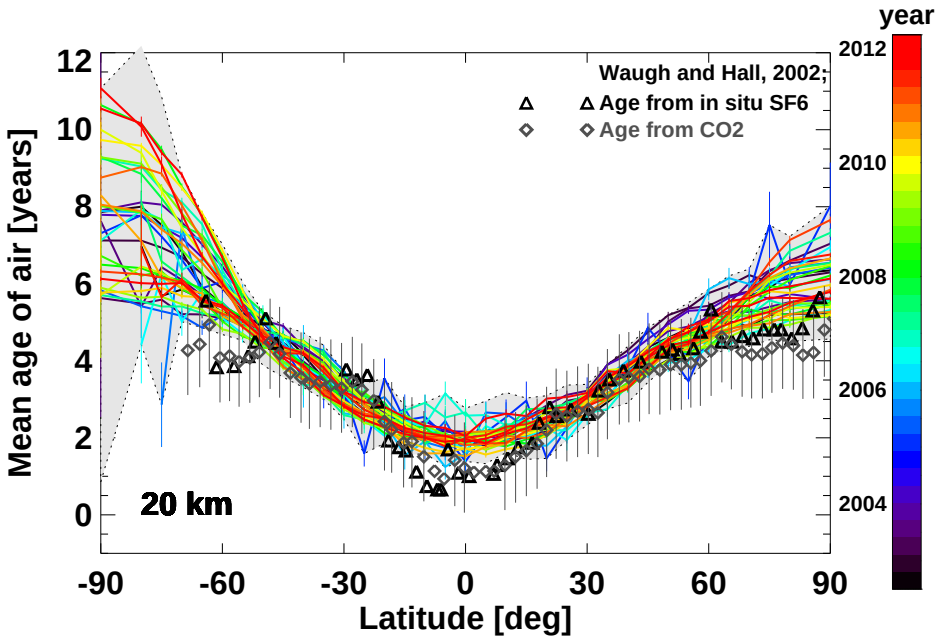

Figure 7.17: Comparison of MIPAS AoA latitude cross sections at 20 km altitude (coloured curves and shaded area) with AoA derived from earlier airborne SF_6 (black triangles) and CO_2 measurements (grey diamonds with error bars) as published in Waugh and Hall [2002] and Hall et al. [1999]. The shaded area represents the range of all MIPAS monthly mean AoA observations, while the coloured curves show AoA latitudinal dependence for every third month. The colour code provides the time of measurement.

the tropics compared to the airborne data due to increased in-mixing of older air from higher latitudes. In addition it should be noted that the airborne measurements do not represent a latitudinal cross section at a given time, but a compilation of measurements from different years and seasons.

In Figure 7.18 MIPAS AoA profiles are compared to airborne AoA profiles (in-situ CO_2 measurements by Andrews et al. [2001a]; Boering et al. [1996]; in-situ SF_6 measurements by Ray et al. [1999]; air sample measurements by Harnisch et al. [1996]) for the tropics (5° S), the northern midlatitudes (40° N) and the northern high latitudes (65° N). In the tropics MIPAS AoA is older than in-situ CO_2 and SF_6 measurements at all altitudes. In the northern midlatitudes the MIPAS profile fits excellently to the SF_6 in-situ data up to an altitude of 27 km and is older higher up. As expected, in-situ CO_2 measurements provide lower ages, and the AoA from SF_6 air samples by Harnisch et al. [1996] is younger, too. At northern high latitudes, MIPAS age profiles only fit well to the SF_6 air samples taken from polar vortex air. To illustrate the high seasonality, monthly averaged MIPAS profiles are additionally shown with oldest ages

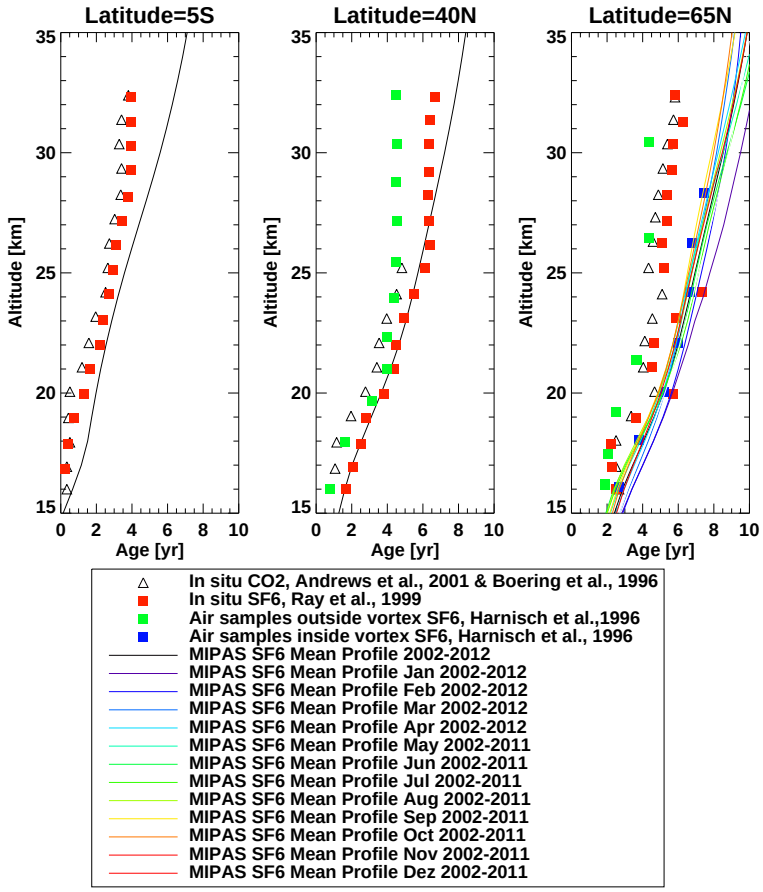

Figure 7.18: Comparison of MIPAS AoA profiles with airborne profiles of the 1990s for the tropics (5° S), the northern midlatitudes (40° N) and the northern high latitudes (65° N).

found for January.

Chapter 8

Observed temporal variability of age of air for the period July 2002 to April 2012

For the analysis of the temporal variability of the new AoA data set the same methods were applied as in Stiller et al. [2012]. However, in contrast to their study and to the publication preceding to this thesis [see Haenel et al., 2015] a revised multilinear regression analysis was used, where sinusoidal terms with periods higher than 1 year and those which are no overtones of the seasonal cycle have been omitted, i.e. the following regression function was now fitted to the data:

$$\begin{aligned} \mathrm{age}(t) = a + bt + c_1 \mathrm{qbo}_1(t) + d_1 \mathrm{qbo}_2(t) \\ + \sum_{n=2}^{5} \left(c_n \sin \frac{2\pi t}{l_n} + d_n \cos \frac{2\pi t}{l_n} \right) \end{aligned} \tag{8.1}$$

where t is time, qbo_1 and qbo_2 are the quasi-biennial oscillation (QBO) indices and the sum represents four sine and four cosine functions of the period length l_n. The period of the first two sine and cosine functions is 12 and 6 months respectively, representing the seasonal and the semiannual cycle. The other two terms have period lengths of 3 and 4 months and describe deviations of the temporal variation from a pure sine or cosine wave (overtones). Fitting sine and cosine of the same period length accounts for a possible phase shift of the oscillation. The terms qbo_1 and qbo_2 are the normalised Singapore winds at 30 and 50 hPa as provided by the Free University of Berlin via http://www.geo.fu-berlin.de/met/ag/strat/produkte/qbo/index.html. These QBO proxies are approximately orthogonal such that their combination can emulate

any QBO phase shift [Kyrölä et al., 2010]. For the fit of the coefficients a, b, c_1, ..., c_5, d_1, ..., d_5 to the data, the method of von Clarmann et al. [2010] is used, which considers the full error covariance matrix of mean age data $\mathbf{S}_\mathrm{m}$ with the squared standard errors of the means of the monthly zonal means as the diagonal terms [Stiller et al., 2012]. Sensitivity studies have shown that the derived AoA trends are robust with respect to the inclusion of further sinusoidal terms in the regression model as applied in Stiller et al. [2012] and Haenel et al. [2015]. Since sinusoidal oscillations with periods 8,9,18 and 24 months have no known physical causes, they have been omitted in the following analysis. In addition, it was tried to fit also a proxy for the 11-years solar cycle to the AoA time series, but the MIPAS period of approximately one decade turned out to be too short for the search for a solar impact. The ENSO signal is another candidate to look for in AoA time series, but since this signal is not periodic no orthogonal term can be used to fit a possible phase shift. The ENSO signal could possibly impact the tropical upwelling, the whole BDC and therefore AoA, but it is also possible that the stratosphere influences processes in the troposphere as the ENSO phenomenon, so both positive and negative phase shifts would need to be considered.

8.1 Age of air trends

First the time series analysis is discussed within the framework of descriptive statistics, i.e. without consideration of the autocorrelations in the residuals of the trend analysis. As a second step, the analysis is repeated within the framework of inductive statistics, where autocorrelated model errors have to be considered (Section 8.1.1).

Figure 8.1 shows an example of the fit of the regression model (in orange) to MIPAS monthly zonal mean data (in blue). The derived linear trend is illustrated as a straight line (orange). The fit considers a potential bias of the two MIPAS measurement periods (dashed orange line) as described in von Clarmann et al. [2010]. Coloured squares indicate the measurements of Engel et al. [2009] and the green dashed line represents the estimated trend of Engel et al. [2009]. The diagram underneath shows the residual of the fit. Such a fit is done for every 10°/1–2 km latitude–altitude bin.

The linear increase of AoA over the whole MIPAS period derived from the regression analysis varies with altitude and latitude. The global view can be seen in Figure 8.2. Red areas indicate increasing AoA, while blue regions indicate decreasing AoA. The distribution of trends in the latitude–altitude plane roughly confirms the mean trends of those obtained by Stiller et al. [2012] and their general morphology but looks more coherent and less patchy, meaning that regions of linear increase and decrease, respec-

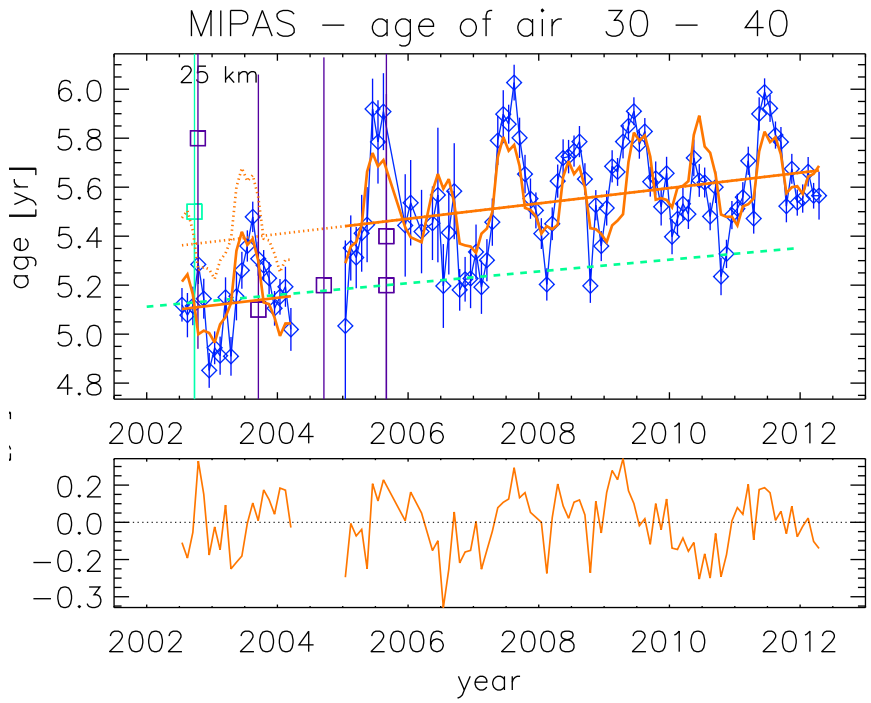

Figure 8.1: Example of the fit (orange curve) of the regression model to MIPAS AoA monthly means (in blue) at 25 km for 30° to 40° N with consideration of autocorrelation and model errors. The error bars represent the standard error of the mean (SEM). The straight orange line is the derived trend, squares represent the measurements by Engel et al. [2009] and the green dashed line is their estimated trend. Underneath the residual of the fit is shown.

tively, are more contiguous. There are basically two regions of linear decrease: A large one consisting of the tropics between about 19 to 33 km and extending to the lower and middle midlatitudinal southern stratosphere, and a smaller one consisting of the upper tropical troposphere extending to the lowermost stratosphere of midlatitudes. These regions are surrounded by regions of AoA linear increase. Largest positive linear trends were observed in the polar regions. Compared to findings of Stiller et al. [2012] a positive linear increase of mean age is confirmed for the northern midlatitudes and southern upper polar stratosphere, as well as for the northern polar lowermost stratosphere. Negative age of air trends of Stiller et al. [2012] in the lowermost tropical stratosphere and lower southern midlatitudinal stratosphere are also confirmed. Differences are found in the northern polar stratosphere, where the mean age is now increasing as well. In the tropical stratosphere the picture is now almost opposite to the previous data of Stiller et al. [2012] meaning that AoA is increasing where it used to be decreasing and vice versa. These changes are attributed to the more adequate

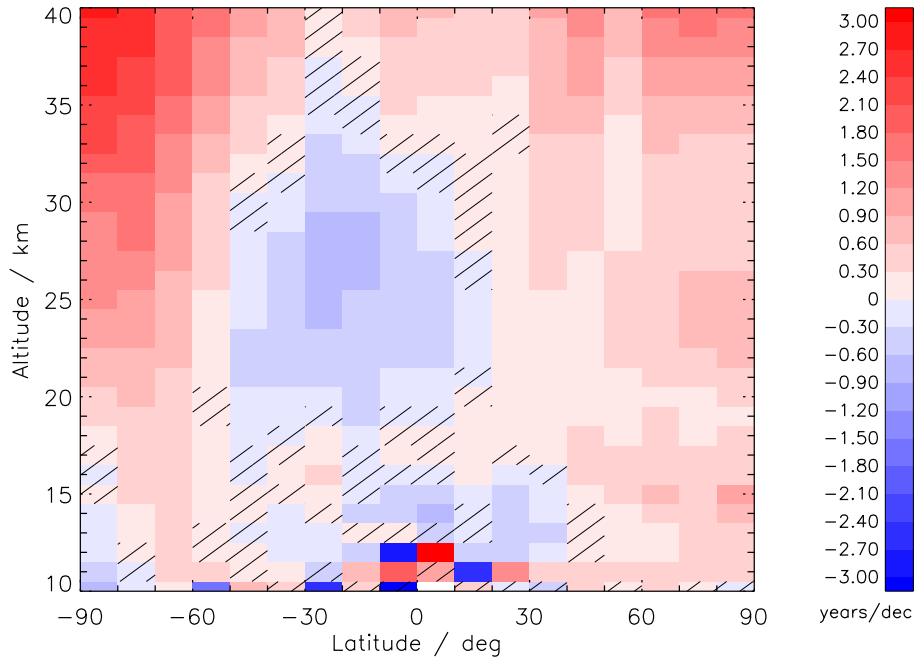

Figure 8.2: Altitude–latitude cross sections of the MIPAS age of air linear increase/decrease over the years 2002 to 2012 without consideration of autocorrelation and model errors. Hatched areas indicate where the trend is not significant.

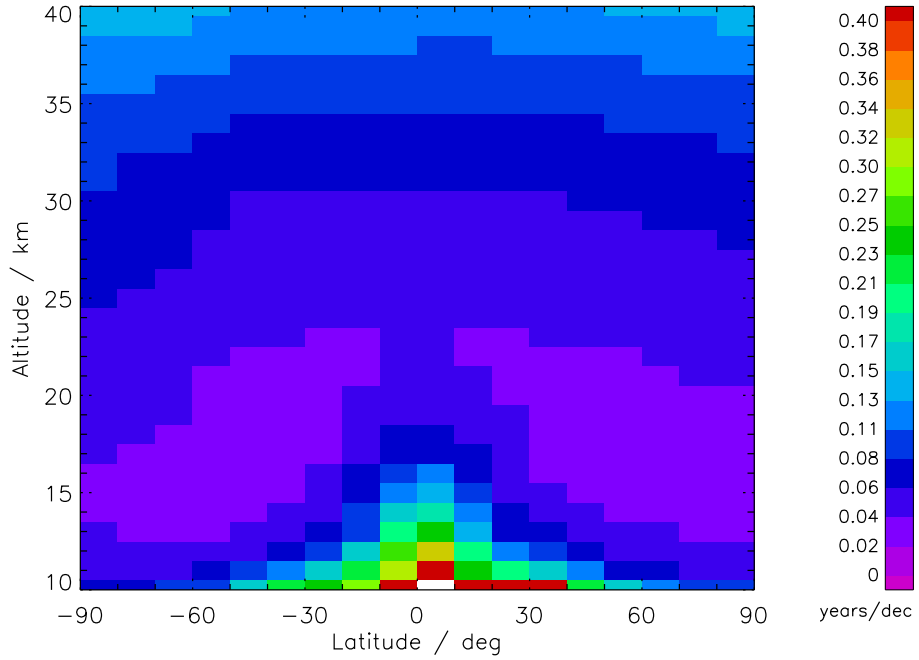

Figure 8.3: 1σ uncertainties of the AoA trends

treatment of the background continuum emission in the retrieval and the associated removal of the spurious SF_6 maximum and subsequent errors.

The uncertainties are rather small, even smaller than the ones derived by Stiller et al. [2012] (see Figure 8.3). This could be a result of the longer time series, covering the full MIPAS period, and the fact that the new AoA data set is less noisy than the previous one. The results are significant on the 2σ level for most of the altitude/latitude bins (see Figure 8.2). Hatched areas indicate where the trend is not significant (i.e. less than its 2σ uncertainty in absolute terms).

8.1.1 Impact of empirical errors and autocorrelation on the AoA trends

As described in Stiller et al. [2012] our regression model only accounts for the linear trend, several periodics and the QBO-terms. Other atmospheric variability especially from non-periodic events is not included in this model. This results in fit residuals which are considerably larger than the data errors represented by the covariance matrix $\mathbf{S}_\mathrm{m}$, which includes only the standard errors of the monthly means and the correlated terms to account for the possible bias between the MIPAS data subsets [von Clarmann et al., 2010]. Therefore the χ^2_reduced of the fit with

$$\chi^2_\mathrm{reduced} = \frac{(a\vec{g}e_\mathrm{MIPAS} - a\vec{g}e_\mathrm{modelled})^\mathrm{T}\mathbf{S}_\mathrm{m}^{-1}(a\vec{g}e_\mathrm{MIPAS} - a\vec{g}e_\mathrm{modelled})}{m-n} \tag{8.2}$$

exceeds the value of unity in most cases, where $a\vec{g}e_\mathrm{MIPAS}$ and $a\vec{g}e_\mathrm{modelled}$ are the data vectors containing the measured and modelled age values, respectively, and where m and n are the number of data pairs and the number of fitted coefficients, respectively [Stiller et al., 2012]. In order to consider these model errors of the regression model, the autocorrelation of the residual time series was estimated in a first step. In a second step the fit was rerun with the autocorrelation and a constant error term added to the covariance matrices. These additional terms in the covariance matrices were scaled within an iterative procedure, such that the resulting χ^2_reduced of the trend fit was close to unity. This iterative procedure is necessary because the additional autocorrelated error term changes the weight between the data points in the fit.

The result of the linear increase/decrease, which is referred to as "model-error corrected linear increase" in Stiller et al. [2012] is shown in Figure 8.4. Compared with the respective figure in Stiller et al. [2012] (Fig. 12) linear increase is again confirmed for the northern midlatitudes and the southern polar middle stratosphere, whereas

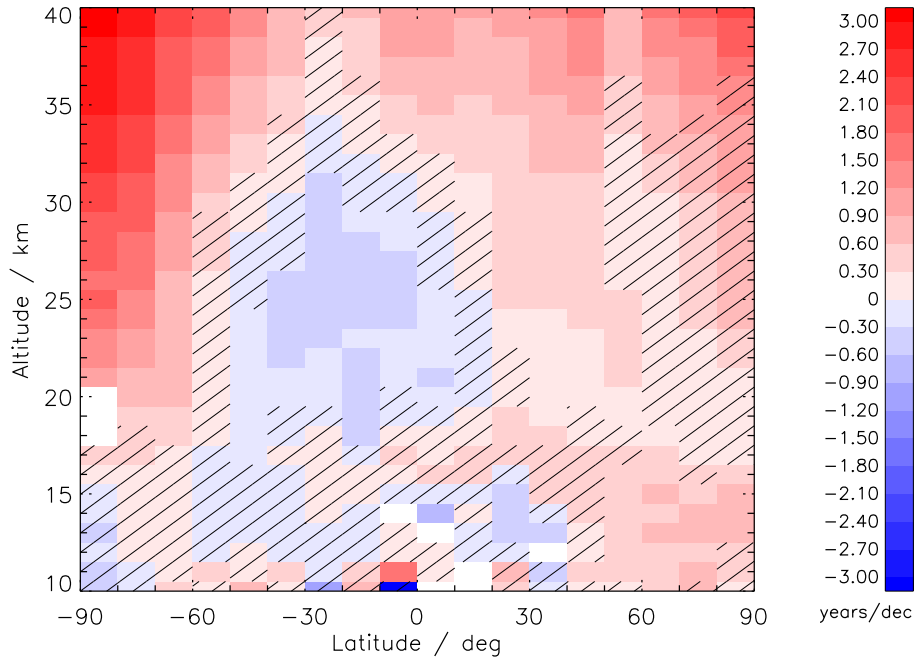

Figure 8.4: Altitude-latitude cross section of the model-error corrected linear increase of MIPAS AoA over the years 2002 to 2012, i.e. after including the model error and autocorrelations between the data points in the fit. Hatched areas indicate where the trend is not significant, i.e. it is smaller (in absolute terms) than its 2σ uncertainty.

linear decrease is confirmed for the lowermost tropical stratosphere and lower and lowermost southern midlatitudinal stratosphere. Differences compared to Figure 12 in Stiller et al. [2012] occur again in the tropics and in the northern polar stratosphere, as well as in the upper southern polar stratosphere.

The overall pattern of linear increase/decrease resembles a lot the pattern in the trend fit without consideration of autocorrelation and empirical errors (Figure 8.2). The significance of most data bins is lower, as expected, due to the additional error (see Figure 8.5). Significant features which appear in both approaches, with and without consideration of autocorrelation and empirical errors, are considered to be most reliable. By comparing Figure 8.4 with Figure 8.2 these features are the linear increase in the southern and northern upper polar stratosphere and in the northern midlatitudes as well as the linear decrease in the tropics and southern subtropics and the southern lower midlatitudinal stratosphere. A clear asymmetry between both hemispheres is confirmed.

The vertical profiles of AoA linear trends for every other latitude bin are shown in Figure 8.6, top panel. Engel et al. [2009] derived a trend of AoA for 30° to 50° N of $+0.24 \pm 0.22$ year per decade (1σ uncertainty level) for the 24 to 35 km altitude range

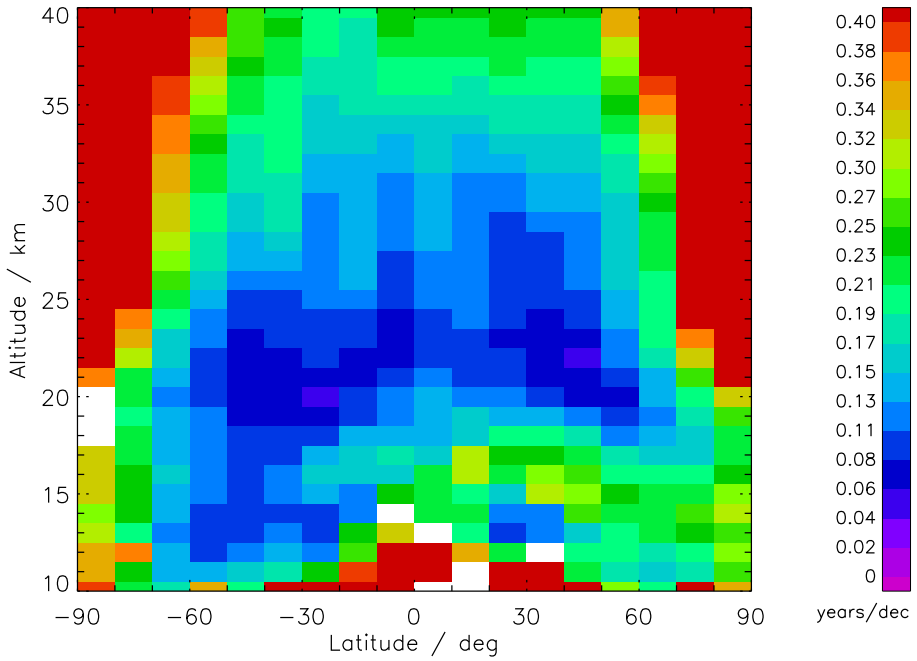

Figure 8.5: 1σ uncertainty of the model-error corrected trend in terms of years/decade.

for 1975–2005. This trend together with its valid altitude range and its 2σ uncertainty is marked as big black cross in Figure 8.6. For better illustration the same picture with the MIPAS linear trend profiles for the two relevant latitude bins is shown in Figure 8.7. The MIPAS AoA trends of 30° to 40° N and 40° to 50° N are slightly lower than in the previous version and match now impressively well (within their error bars) with the trend estimated by Engel et al. [2009] in the 24 to 35 km altitude region. One has to keep in mind that the trend derived by Engel et al. [2009] represents the time period 1975–2005, while MIPAS measured from 2002 to 2012. So there is only a small overlap between the two periods. Still the agreement of both trends is remarkable. The MIPAS AoA trends for the latitude bins 30° to 40° N and 40° to 50° N are significantly distinct from 0 for all altitudes above 21 km even on the 2σ uncertainty level.

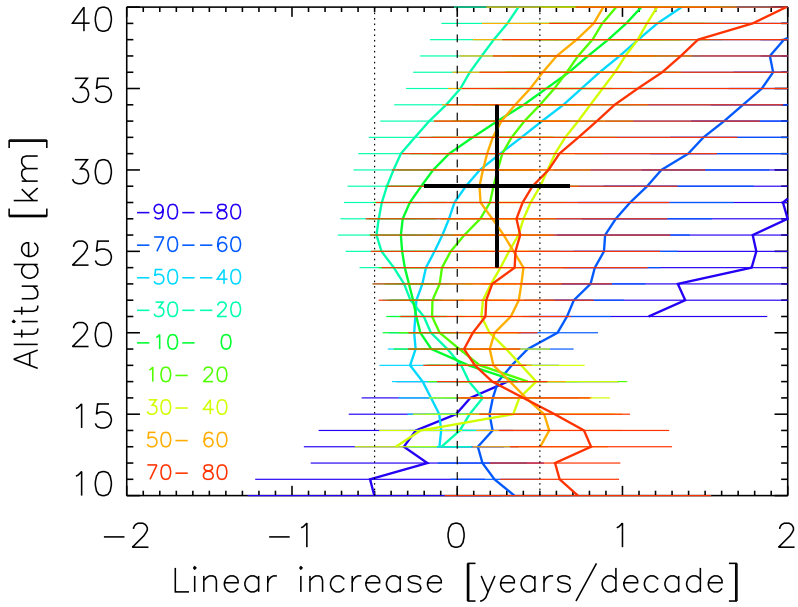

Figure 8.6: Vertical profiles of the age of air linear increase/decrease over the years 2002 to 2012 for example latitudes. Horizontal bars give the 2σ uncertainties of the linear variations. The 30-year trend as derived by Engel et al. [2009] for the northern midlatitudes is also shown for comparison as a black cross indicating its valid altitude range and its 2σ uncertainty.

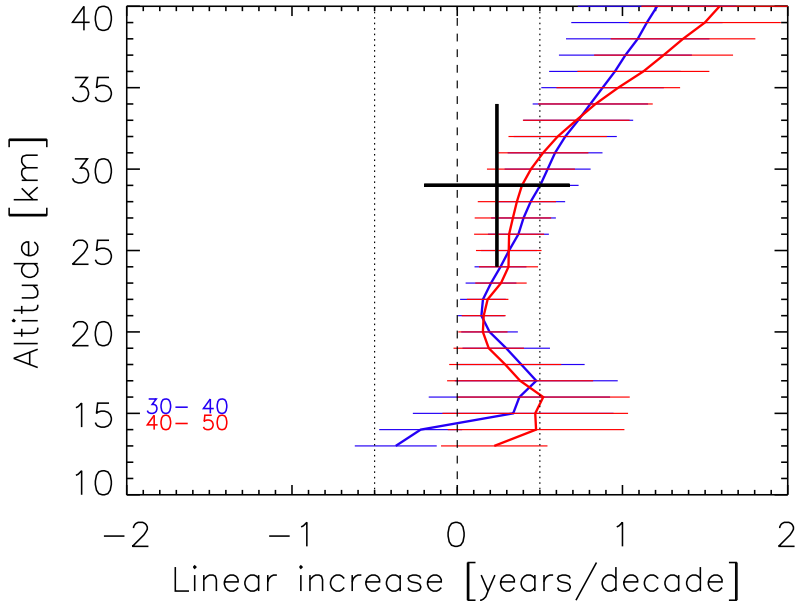

Figure 8.7: Same as Figure 8.6 but for the latitude bins 30° to 40° N and 40° to 50° N

8.1.2 The importance of the considered bias on age of air trends

The trend calculations of the previous sections consider a potential bias in AoA between the two MIPAS measurement periods. The procedure allows a different bias for each altitude/latitude bin. The bias can result from the different vertical sampling in FR- and RR-period, which is finer in the latter. The investigation in this section will demonstrate that the consideration of such a bias is crucial for the estimation of the correct decadal trend over the whole MIPAS period.

Figure 8.9 shows the distributions of MIPAS AoA trends, if a potential bias in each altitude and latitude was neglected. This pattern of negative AoA trends in the upper troposphere and lower stratosphere and positive AoA trends above is totally different than the patterns of the previous sections. The dipole structure in the distributions of trends in the middle stratosphere is completely lost.

An example of how the bias between the two measurement periods strongly influences the AoA decadal trend, if not accounted for, can be seen in Figure 8.8. The upper panel shows the estimated trend, if the bias was not considered, while the lower panel demonstrates that a completely different trend is obtained, if the fitting procedure allows a possible bias. Both MIPAS periods exhibit a decreasing trend if examined separately (as in the lower panel of Figure 8.8). However, the jump between 2004 and 2005 produces an artificial total trend (slightly positive in this case), which is not a real trend in the atmosphere.

The specific decadal AoA trends from 2002 to 2012 in the atmosphere as shown in Sections 8.1 and 8.1.1 should also be present in the second MIPAS period from 2005 to 2012, which covers approximately 80% of the MIPAS measurements. And indeed, as shown in Figure 8.10, the consideration of only the RR-period of MIPAS, roughly confirms the trend patterns of those found in Sections 8.1 and 8.1.1. The distinctive dipole structure of negative trends in the Southern Hemisphere and positive trends in the Northern Hemisphere can also be found if only the RR-period is considered. This is a strong indication that the trend patterns in the previous sections (see Figure 8.2 and Figure 8.4) reflect real trends in the atmosphere, while the trends in Figure 8.9 are strongly biased by the jumps in AoA between the two MIPAS periods.

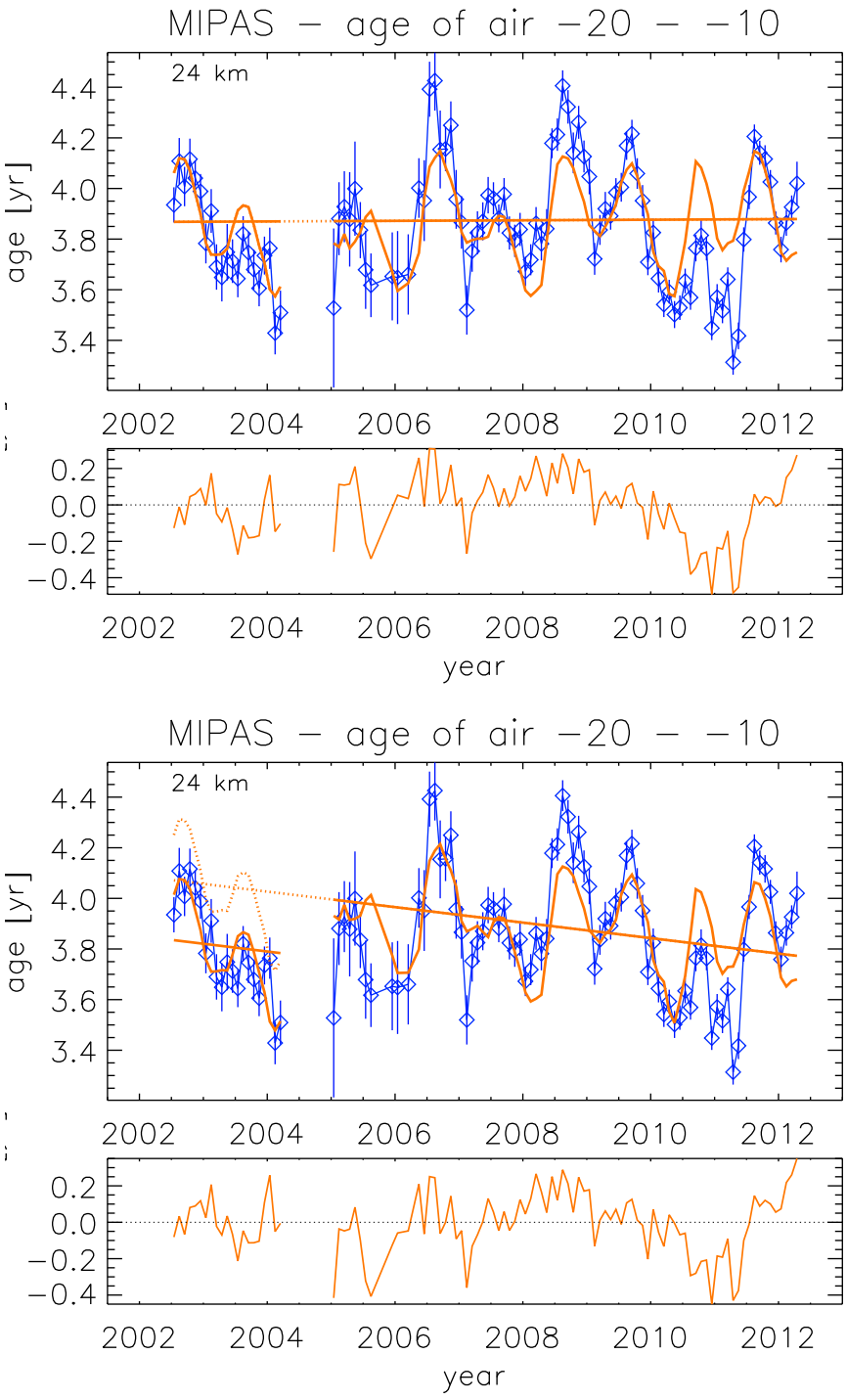

Figure 8.8: Example of the fit (orange curve) of the regression model to MIPAS AoA monthly means (in blue) at 24 km for 10° to 20° S with consideration of autocorrelation and model errors. The error bars represent the standard error of the mean (SEM). The straight orange line is the derived trend without consideration of a bias (upper panels) and with consideration of a bias between MIPAS FR- and RR-period (lower panels).

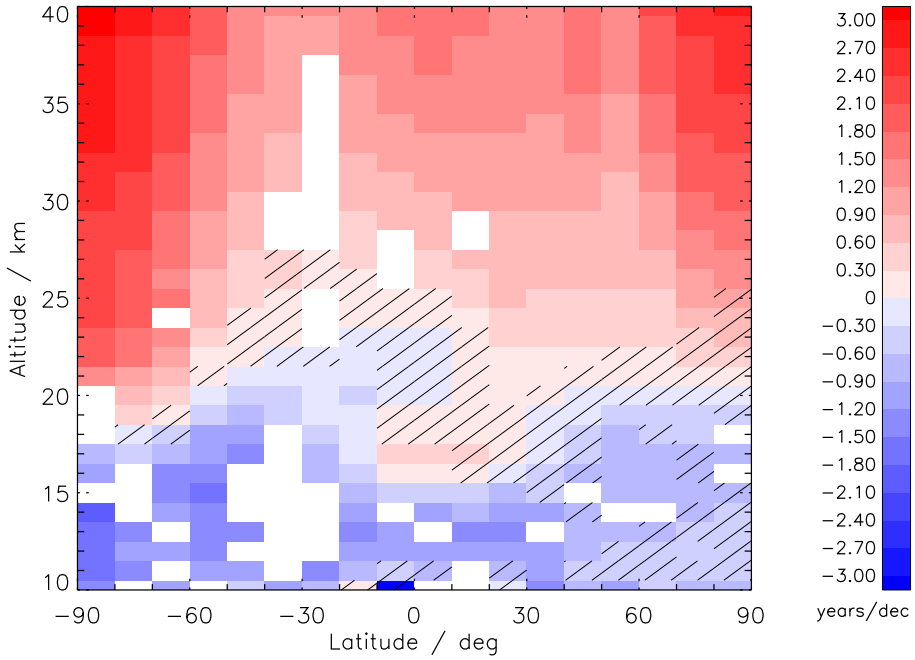

Figure 8.9: MIPAS age of air trends (model-error corrected) without consideration of a potential bias between FR- and RR-period. Hatched areas indicate where the trend is not significant.

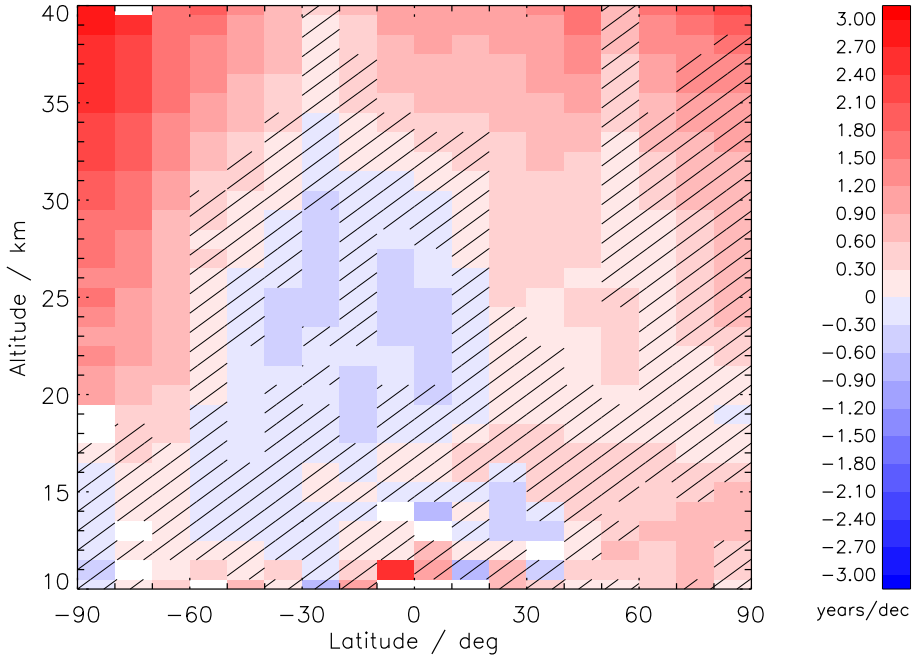

Figure 8.10: MIPAS age of air trends (model-error corrected) only for the reduced resolution time period (2005-2012). Hatched areas indicate where the trend is not significant.

8.2 Impact of age spectra on age of air and trends

The Brewer-Dobson circulation (BDC) transports air parcels through the stratosphere. During its way the air parcels undergo also mixing processes. Therefore an air parcel does not have a single transit time. In order to describe its transport the distribution of all transit times, called the age spectrum (see Section 2.4), needs to be considered. The age spectrum is not a measurable quantity. However, to calculate the mean age from tracer distributions in the stratosphere, which are not growing strictly linear in the troposphere, the age spectrum is needed, because only for a strictly linearly growing tracer the mean of the age spectrum and the lag time are identical. In Section 6.2 the age of air was inferred from MIPAS SF_6 distributions under consideration of the non-linearity of the SF_6 reference curve. For this approach an assumption on the shape of the age spectrum represented by an inverse Gaussian function (Wald function, see Section 2.4) has been used. Sensitivity studies have shown that the age of air trends are strongly influenced by the slight non-linearity of the SF_6 reference curve and by its correction applying an age spectrum. If the SF_6 reference curve was exactly linear, then the mean AoA would be equal to the time lag a certain SF_6 mixing ratio is observed in the stratosphere compared to when it was observed in the troposphere. In this case the AoA trend can be calculated directly from the SF_6 trends observed in the atmosphere:

$$[SF_6](r,t) = [SF_6]_{ref}(t - age(r,t)) \tag{8.3}$$

Then the derivative with respect to time is taken:

$$\frac{\partial [SF_6](r,t)}{\partial t} = \frac{d[SF_6]_{ref}}{dt} - \frac{d[SF_6]_{ref}}{dt} \cdot \frac{\partial age(r,t)}{\partial t} \tag{8.4}$$

This equation can now be solved for the age trend:

$$\frac{\partial age(r,t)}{\partial t} = \frac{\frac{d[SF_6]_{ref}}{dt} - \frac{\partial [SF_6](r,t)}{\partial t}}{\frac{d[SF_6]_{ref}}{dt}} = 1 - \frac{\frac{\partial [SF_6](r,t)}{dt}}{\frac{d[SF_6]_{ref}}{dt}} \tag{8.5}$$

The AoA trends inferred from MIPAS SF_6 trends assuming an exact linear tropospheric increase in $SF_{6_{ref}}$ are shown in Figure 8.11. The pattern differs significantly from the trend patterns calculated in Sections 8.1 and 8.1.1. However, the distribution of trends appears to be slightly asymmetric which means that the asymmetry observed in the MIPAS AoA trends can already be found in the SF_6 trends.

The next step in this sensitivity study was deriving AoA trends from AoA calcu-

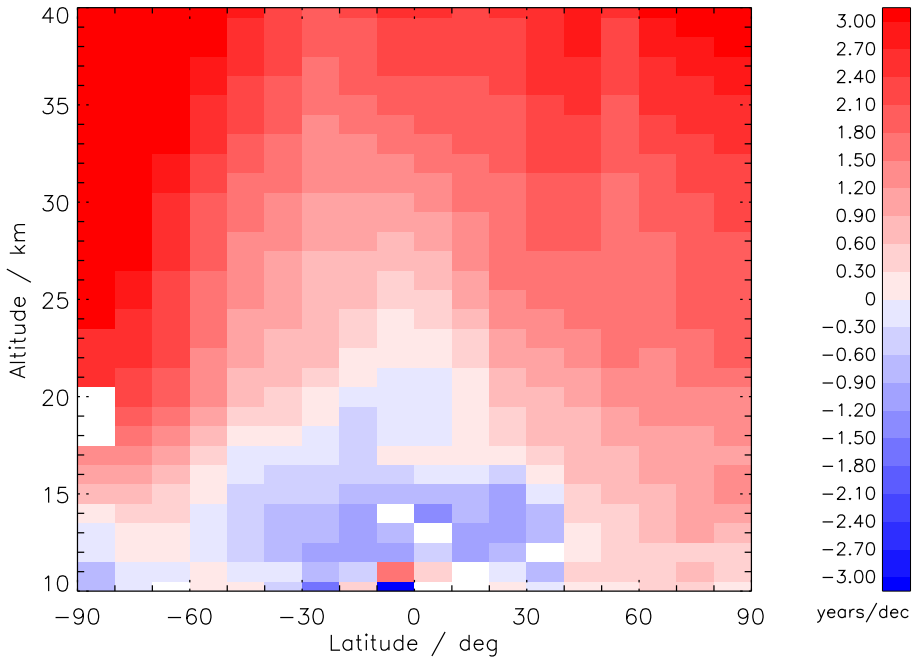

Figure 8.11: AoA trends calculated from measured stratospheric SF_6 trends assuming strictly linear increase of the reference SF_6 abundance.

lated using the real slightly non-linear reference curve (see Figure 6.2), but without applying the non-linearity correction, i.e. a delta function was used as age spectrum in the convolution procedure (see Section 6.2). The resulting trend pattern is depicted in Figure 8.12 and brings out the asymmetry of negative trends in the Southern Hemisphere and positive trends in the Northern Hemisphere. In contrast to Figure 8.4 there appear also some negative trends in the northern mid- and polar latitudes, but they are not significant. The trends of AoA calculated from slightly non-linearly increasing reference SF_6 and idealised age spectra are shown in Figure 8.2 and Figure 8.4, respectively.

Age spectra varying according to the location in the stratosphere and time can be assessed by models using the pulse tracer method (see Section 2.4.1) for example. The aim of this section is to apply model spectra from the CLaMS model [Ploeger and Birner, 2016] to the non-linearity correction of MIPAS age of air and to study the effect on MIPAS age of air trends.

CLaMS age spectra are provided as monthly zonal means on a potential temperature grid used as the altitude coordinate ranging from 320 K to 2500 K and on 91 latitude levels. For every MIPAS latitude/altitude bin, the potential temperature Θ was calculated using MIPAS monthly zonal means for pressure and temperature ac-

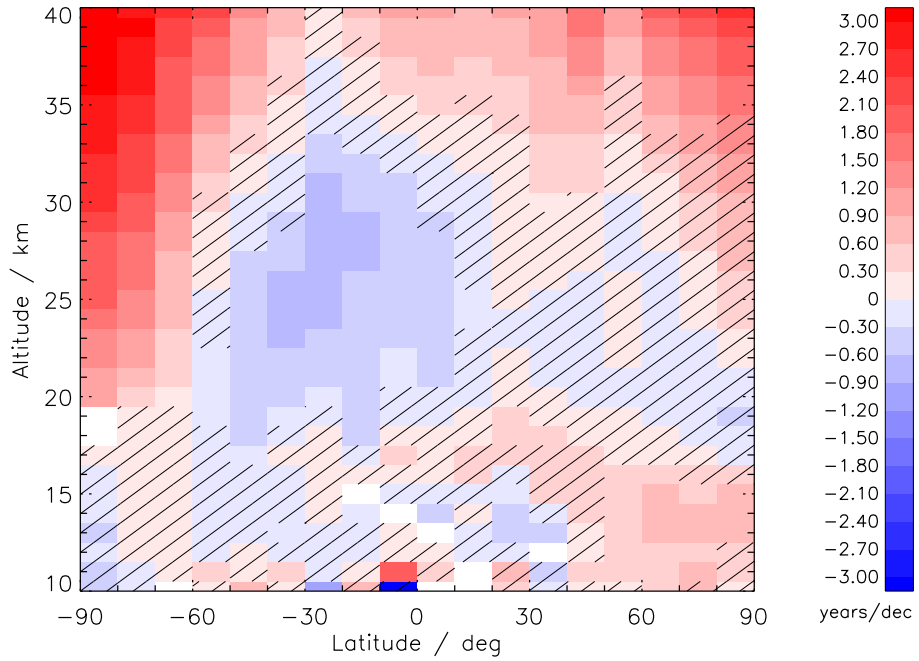

Figure 8.12: Trends for AoA calculated with a realistically increasing SF_6 reference abundance, but a delta-shaped age spectrum. Hatched areas indicate where the trend is not significant.

cording to the formula

$$\Theta = T \cdot (\frac{p_0}{p})^{\frac{R}{c_p}} \tag{8.6}$$

where p_o=1000 hPa and $\frac{R}{c_p}$=0.286 for dry air have been used.

Then, for each monthly zonal mean, the closest CLaMS age spectra in potential temperature and latitude space to the MIPAS measurements was determined. As most models, CLaMS age of air has a low bias compared to the MIPAS measurements. Therefore the CLaMS age spectra cannot be used in the convolution procedure (see Section 6.2) directly. It was assumed that the CLaMS model provides a better estimation on the shape of the age spectra than the simple Wald function, but it needed to be shifted in time towards the higher MIPAS age of air values. As stated by Ploeger and Birner [2016] the Wald function assuming idealised stationary flow provides a good approximation of the annual mean age spectrum.

Figure 8.13 shows typical CLaMS age spectra for different latitudes and potential temperatures in the Northern Hemisphere as monthly zonal means for January 2008 compared to the Wald function of the same mean age, which was used to infer MIPAS age of air and trends. The Wald functions reflect roughly the shape of the age

spectra, as already stated by Waugh and Hall [2002], but they cannot describe the seasonal variability included in the CLaMS age spectra. The CLaMS age spectrum in Figure 8.13 a exhibits a large peak at an age of about 0.2 years, is very narrow and can be described by the Wald function fairly well. It describes the transport and mixing just above the tropopause at 10° N in the tropics, where the AoA is still very young and hardly any mixing has occurred. In Figure 8.13 b the situation is shown at 50° N and 800 K (approx. 30 km). The CLaMS spectrum has a double peak at younger ages than the Wald function and shows strong seasonal variation. The lower panels of Figure 8.13 represent the northern polar regions at 800 K (approx. 29 km) and 2000 K (approx. 46 km), respectively. In general it seems that the Wald functions underestimate the CLaMS spectra in the vicinity of the peaks which describe the advection, but overestimate the tail of the distribution, which is primarily caused by mixing and recirculation processes[1]. Figure 8.14 shows the same picture, but now for January 2003 and demonstrates that the CLaMS spectra vary considerably over the MIPAS measurement period even in the same month.

In order to apply the correct shift in time to the CLaMS age spectra accounting for the bias between CLaMS and MIPAS age of air, a precise estimate of the CLaMS mean age is needed, which is the first moment of the age spectrum (see Section 2.4). The typical age spectra are asymmetric and the mean age is strongly dependent on the long "tail" of the age spectrum. However, CLaMS age spectra are cut off at a transit time of 10 years. Therefore the CLaMS mean age is calculated by fitting an exponential decay to represent the tail of the age spectrum and the integral calculating the mean age is then extended to infinity. This assumption implies that the age spectrum is approximated by the former approach for very high ages, as the Wald function approximately also decays exponentially with the transit time going to infinity. This exponential decay of the age spectrum for ages larger than about 4-5 years is also corroborated by other studies [e.g. Diallo et al., 2012; Li et al., 2012].

The MIPAS age of air measurements at a given latitude, altitude and time are then corrected by convolution of the SF_6 reference curve with the respective CLaMS age spectra, shifted by the difference of MIPAS and CLaMS mean age during the iterative procedure as described in Section 6.2. This was necessary, because CLaMS mean ages are considerably younger than MIPAS ones. As the integral of the convolution also covers the full set of transit times from zero to infinity, the tail of the age spectrum

[1] recirculation occurs e.g. when an air parcel travels along the residual circulation to the extratropics, is mixed back to the tropics and circulates again along the residual circulation [Garny et al., 2014].

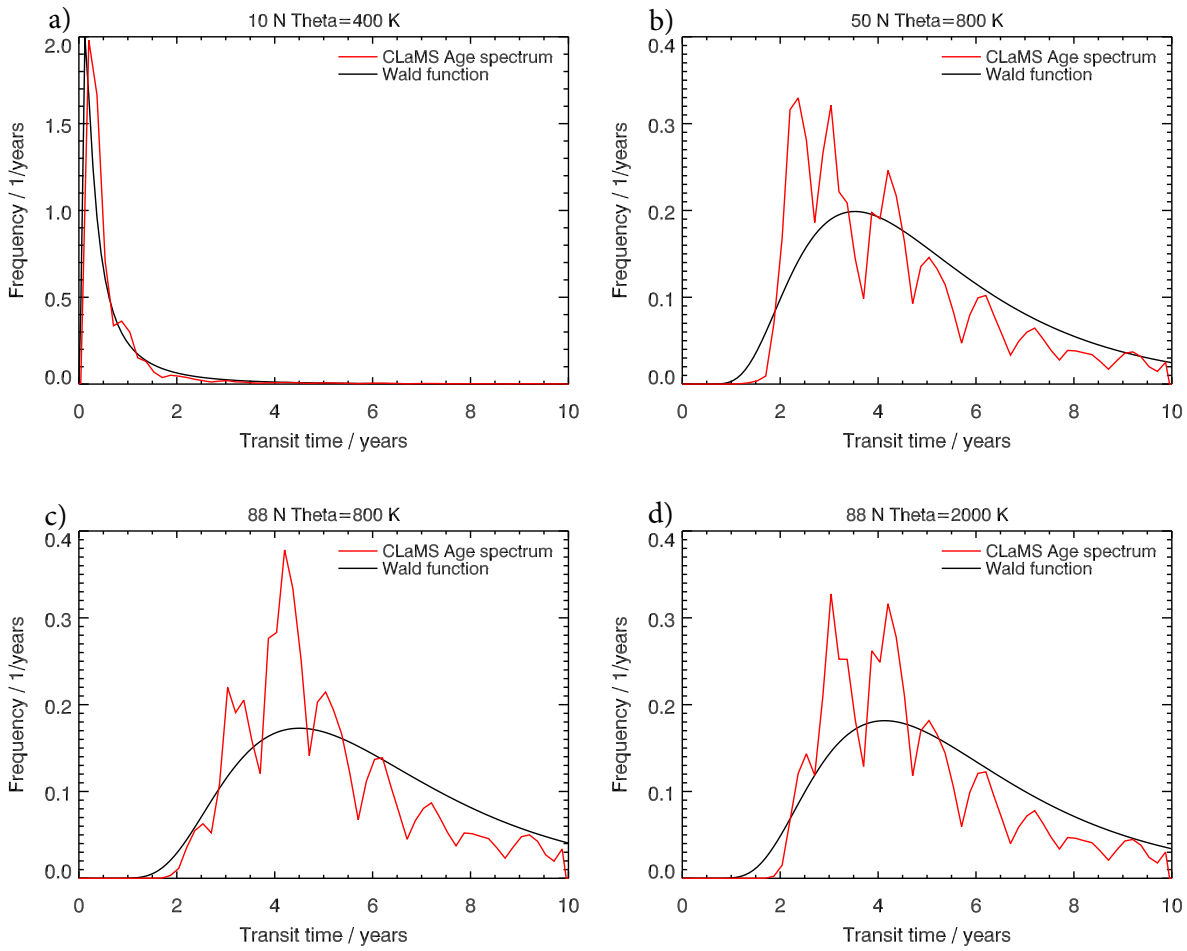

Figure 8.13: Age spectra simulated by the CLaMS model for January 2008 for different potential temperatures and latitudes (in red) compared to the Wald function (black lines) of the respective mean age.

was again approximated by the tail of the Wald function for ages greater than the "cut-off"-age of the CLaMS spectrum. The age of air distributions calculated with this method are shown in Figure 8.15. Compared to the respective figure of the former approach (Figure 6.3) using ideal Wald functions to approximate age spectra, one can see that effects of a more realistic age spectrum are small, which demonstrates that our age of air calculation is robust. Little differences occur in the upper stratosphere where the age of air is now slightly lower. But it should be noted that CLaMS age spectra are only shifted on the time axis accounting for the bias between MIPAS and CLaMS AoA, whereas the shape and especially the width of the CLaMS spectrum remained the same. The CLaMS age spectra are dependent on potential temperature and latitude and also their variation in time is considered, but they are not a function of the mean age itself. However, there seems to be no way to remove this uncertainty

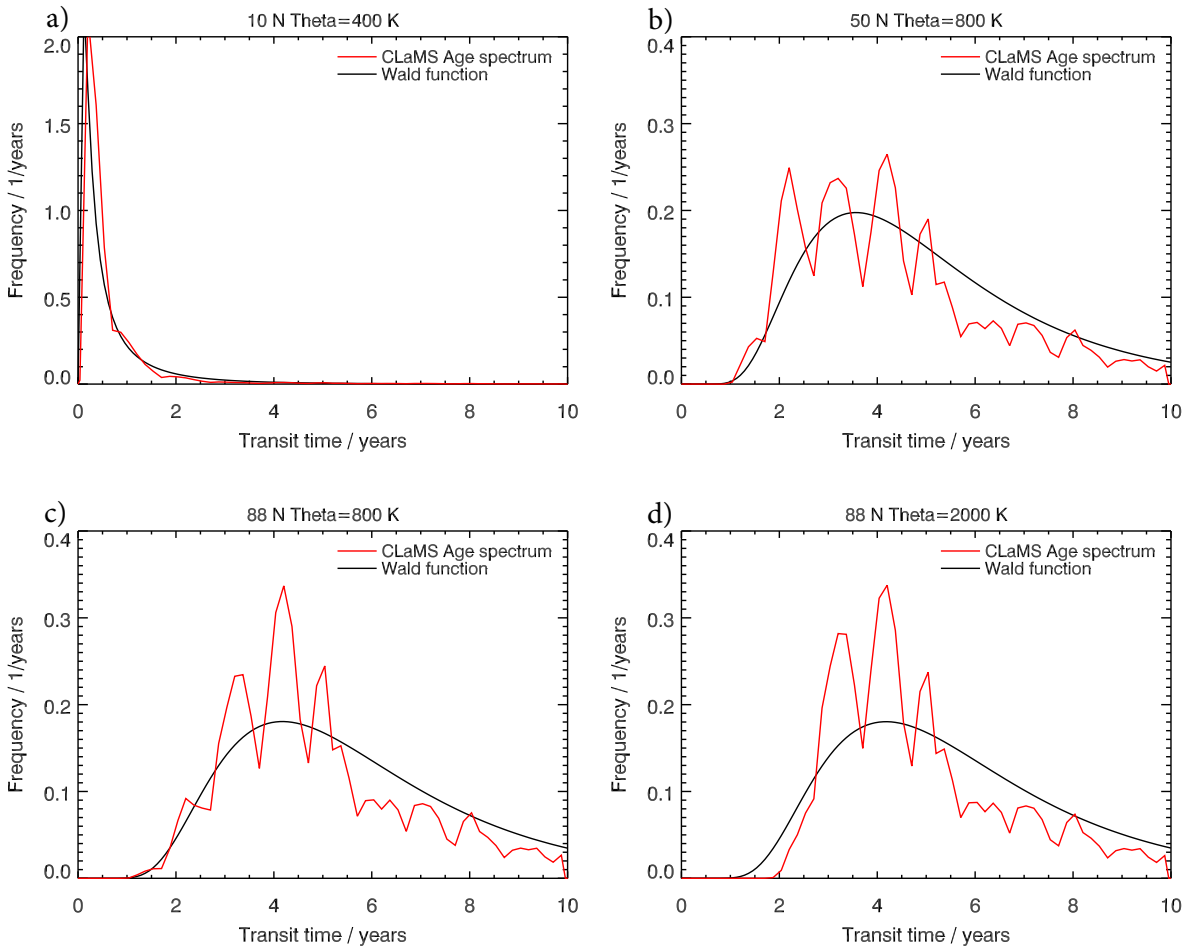

Figure 8.14: Age spectra simulated by the CLaMS model for January 2003 for different potential temperatures and latitudes (in red) compared to the Wald function (black lines) of the respective mean age.

which is caused by the bias between MIPAS and CLaMS mean age.

Now the impact of using CLaMS age spectra for the non-linearity correction of the SF_6 reference curve on the decadal MIPAS AoA trend is studied. The procedure described in Section 8.1 was now repeated for this refined AoA data set. The result is shown in Figure 8.16 directly for the "model-error corrected linear increase" as its significance is more realistic (see Section 8.1.1) and corroborates the previous findings (Figure 8.4), as the patterns of AoA linear increase and decrease are nicely reproduced. Especially the pronounced dipole structure of negative AoA trends in the Southern Hemisphere and positive AoA trends in the Northern Hemisphere is confirmed. However, trends in the middle stratosphere at low- to midlatitudes are smaller than before (in absolute terms).

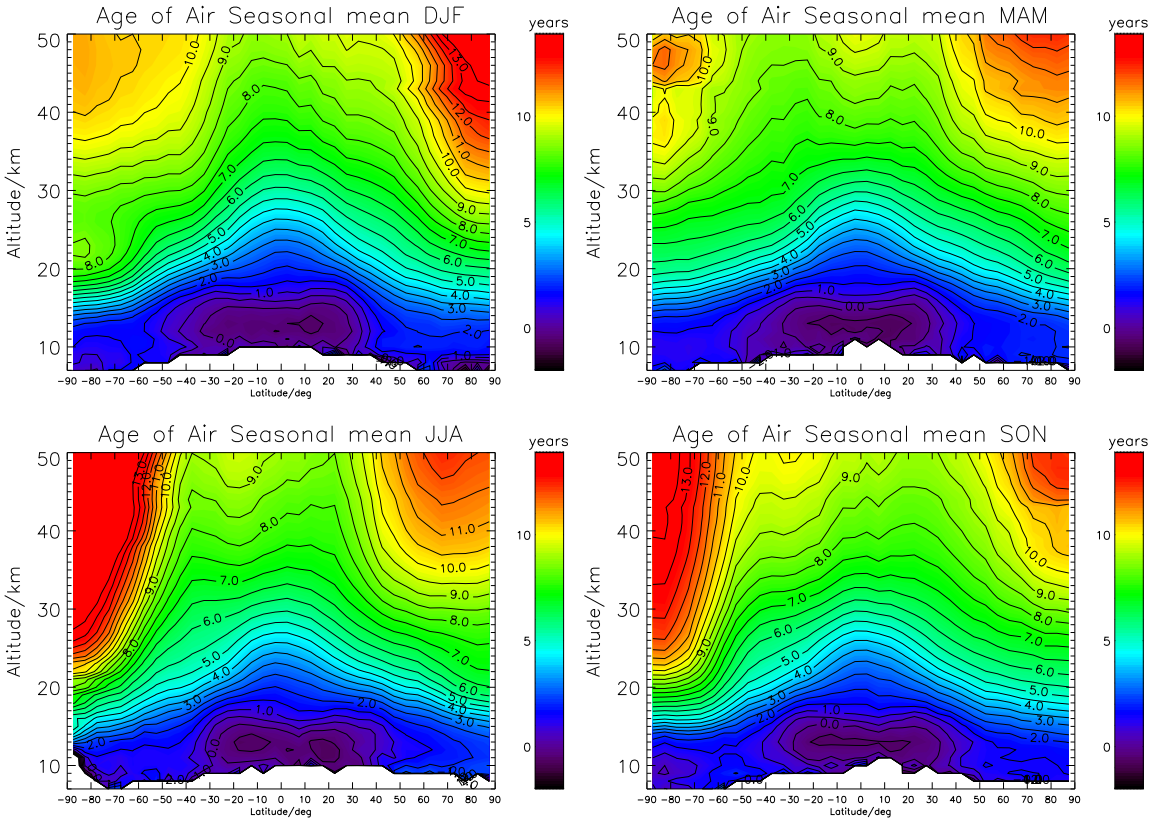

Figure 8.15: Zonal mean distribution of mean age of stratospheric air averaged for the four seasons, where the AoA has been corrected using simulated age spectra from the CLaMS model

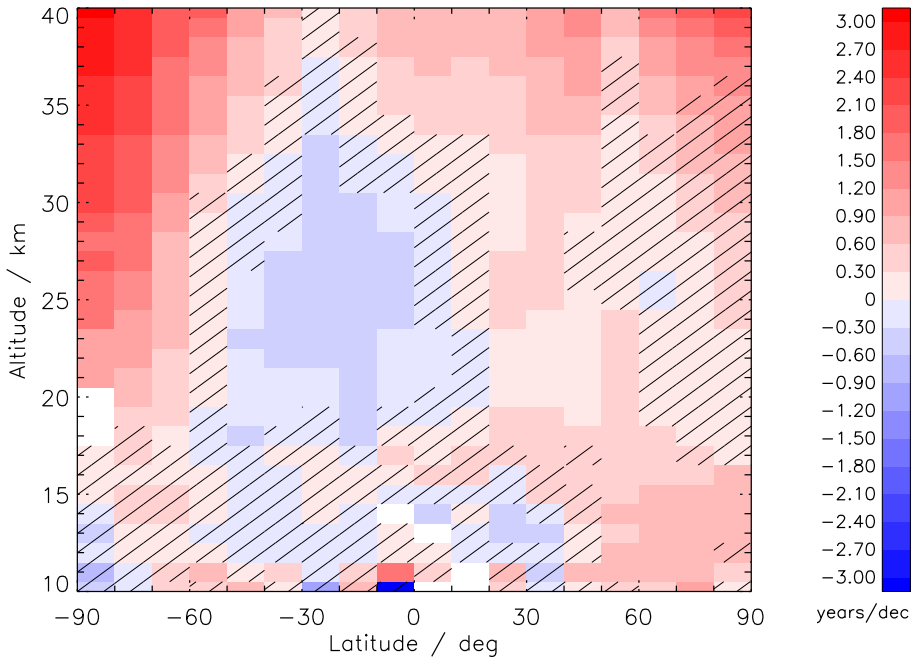

Figure 8.16: MIPAS AoA trends (model-error corrected) using CLaMS age spectra for the non-linearity correction. Hatched areas indicate where the trend is not significant.

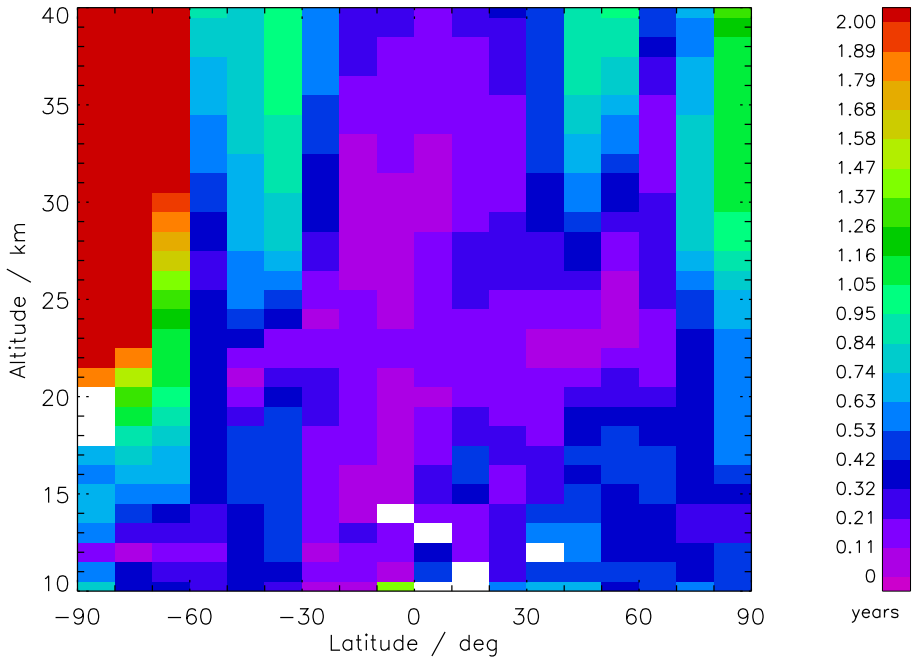

Figure 8.17: Altitude-latitude cross section of amplitudes of the seasonal variation of mean age of air

8.3 Annual cycle and influence of the quasi-biennial oscillation

In this section the annual cycle of AoA in different regions of the stratosphere is studied and compared to previous findings in literature including both model and empirical studies. The seasonal variations of AoA basically reflect the seasonality of stratospheric transport, mixing and the mixing barriers, in particular the polar vortex and the tropical pipe boundary as well as the subtropical jets. Figure 8.17 shows the amplitudes and Figures 8.18 and 8.19 the phases of the seasonal cycle of MIPAS AoA in terms of the month where the minimum and maximum, respectively, occurs. These are the amplitudes and phases of terms with period length 1 year determined with the regression model described above. Compared to Figure 9 in Stiller et al. [2012] there are no substantial differences in the new data set. As observed by Stiller et al. [2012], the amplitudes of the seasonal variation are strongest in the southern polar stratosphere, which can be explained by regular intrusion of SF_6-depleted mesospheric air into the polar winter vortex, which leads to very old apparent ages, and its removal during summer by the overturning circulation. Over the year, the oldest AoA occurs there at the end of southern hemispheric winter to spring, as expected, while the youngest air

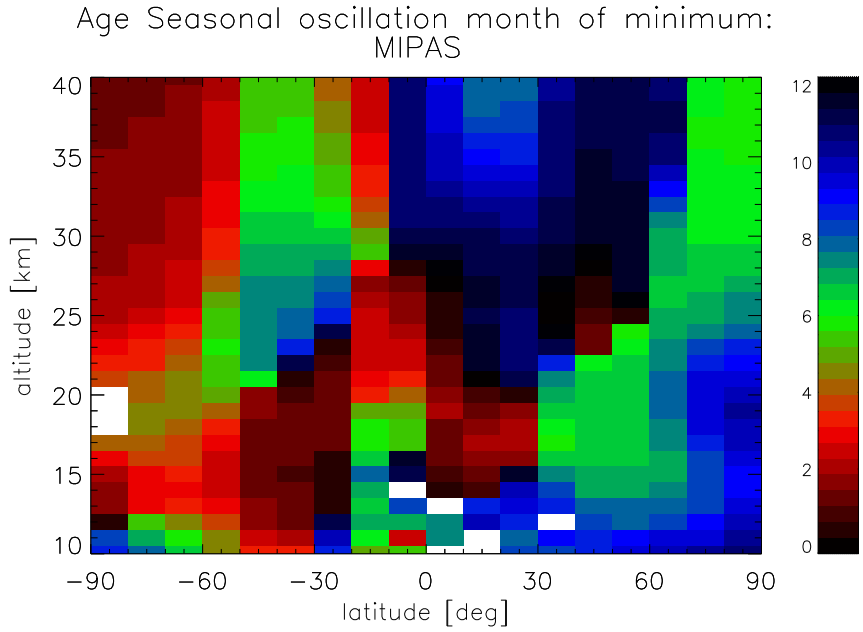

Figure 8.18: Altitude–latitude cross sections of month of the minimum of the seasonal variation of the mean age of air.

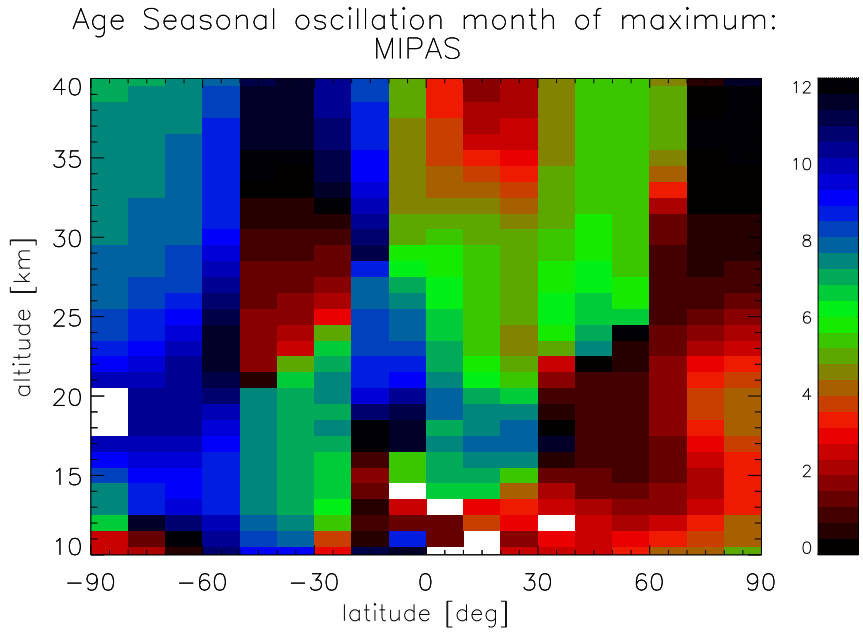

Figure 8.19: Altitude–latitude cross sections of month of the maximum of the seasonal variation of the mean age of air.

is observed at the end of southern summer to autumn. This process is also observed in the Northern Hemisphere, but with smaller amplitude [see also Funke et al., 2005].

The phase shift of half a year between below and above 25 km in the polar stratosphere reported by Stiller et al. [2012] is only partially visible between the upper stratosphere and the lowermost altitude bins in both hemispheres in the new MIPAS data. Diallo et al. [2012] found polar stratospheric AoA above 25 km, with youngest air at the end of local winter to spring, to be in the opposite phase than in the lowermost extratropical stratosphere in their analysis of ERA-Interim data. In the model analysis of Li et al. [2012] the maximum of AoA in the polar region in spring is also restricted to the lower stratosphere, whereas the upper polar stratosphere exhibits younger air (lower age). In contrast, the oldest air in northern polar regions is found in MIPAS data in spring in the lower stratosphere and in midwinter in the higher stratosphere. This difference to MIPAS AoA can be explained by the different derivations of AoA in the respective studies: while in Diallo et al. [2012] AoA is explicitly calculated by backward trajectories of the air parcel, and in Li et al. [2012] the AoA is determined by the pulse tracer method, the MIPAS AoA is derived by SF_6 observations which exhibit an overaging when SF_6-depleted mesospheric air subsides into the polar stratosphere during winter. This overaging in the polar stratosphere during winter shifts the phase in the MIPAS data towards oldest air in polar midwinter, when subsidence of mesospheric air is strongest. However, the distinct annual cycle in the lower southern polar stratosphere seems to be "real" and not an artefact of the SF_6 sink in the mesosphere, as it was also simulated with the CLaMS model in Ploeger et al. [2015b] using a "clock tracer" with oldest air at the end of winter at 500 K (approx. 20 km).

In the tropics and most parts of the northern midlatitudes the amplitude of the seasonal cycle is rather small (except for the midlatitudes above 25 km). The overall distribution of amplitudes is consistent to the one in Stiller et al. [2012].

Some discernible difference to the previous data set is that the band of high seasonal amplitudes in the northern midlatitudes is not visible anymore in the new distribution of amplitudes (Figure 8.17). Instead there is a region in northern midlatitudes above 25 km, which also exhibits high amplitudes like the equivalent region in the Southern Hemisphere. A higher amplitude of the seasonal cycle is now also found in the extratropical southern lowermost stratosphere (LMS). Hence, now both hemispheres (much less pronounced in the Northern Hemisphere) show enhanced seasonal amplitudes in the extratropical LMS, which are tentatively attributed to the seasonality of the permeability of the subtropical jet [Stiller et al., 2012] (most permeable in summer) and flooding of this region with old vortex air after the vortex breakdown at the end of

winter and spring.

Consistently Diallo et al. [2012] found high amplitudes of the seasonal cycle in the southern and northern extratropical LMS. Most parts of both the southern and northern extratropical LMS reach their maximum in AoA at the end of local winter to spring in the MIPAS data set as well as in the analysis by Diallo et al. [2012]. This hemispheric symmetry is a feature of the new MIPAS data set. Bönisch et al. [2009] found oldest AoA in the northern LMS in April and youngest in October with in-situ measurements of SF_6 and CO_2 during the SPURT aircraft campaigns. MIPAS observed youngest air in hemispheric late summer to autumn when the mixing barrier in the subtropics is weakest and young air from the tropics is injected in this region, also referred to as "flushing" of the LMS [Hegglin and Shepherd, 2007]. This flushing was noticed by Ploeger and Birner [2016] and Ploeger et al. [2015b], who analysed the seasonality of AoA in the CLaMS model, to be especially pronounced in the Northern Hemisphere. Also cross-tropopause isentropic mixing from the tropical troposphere in the extratropical LMS is enhanced during summer–early autumn when the subtropical jet is weak [Chen, 1995].

Model results of Li et al. [2012] of the seasonal variation of AoA also agree with MIPAS in the extratropical LMS.

In the northern subtropical lower stratosphere an abrupt meridional phase shift of almost half a year occurs, which means that these air masses are well isolated by the subtropical jet. Equatorwards the air is oldest in summer, when the subtropical mixing barrier and the upwelling of the BDC are weakest and older air from the extratropics is mixed in. This process is also indicated in the Southern Hemisphere and these opposite phases between the subtropics and the extratropics are also observed in the model results of Li et al. [2012].

In the northern tropical to midlatitudinal middle and upper stratosphere [0°-60° N, 25-40 km] the air is youngest in local winter, when, according to the known seasonality of the deep branch of the Brewer–Dobson circulation, younger air is brought to higher altitudes and latitudes more efficiently. This is also observed in the southern midlatitudinal middle and upper stratosphere [20°-50° S, 28-40 km]. The mixing barriers are partially visible by abrupt phase shifts in the month of minimum and maximum age respectively: air masses in the polar vortex are well isolated from the rest of the hemisphere. The subtropical mixing barrier is visible in the northern lower stratosphere at 30° N and is indicated in the upper stratosphere only in the plot of maximum age (Figure 8.19). In the Southern Hemisphere the abrupt phase shifts seem to occur at 50°–60° S and at 10°–20° S.

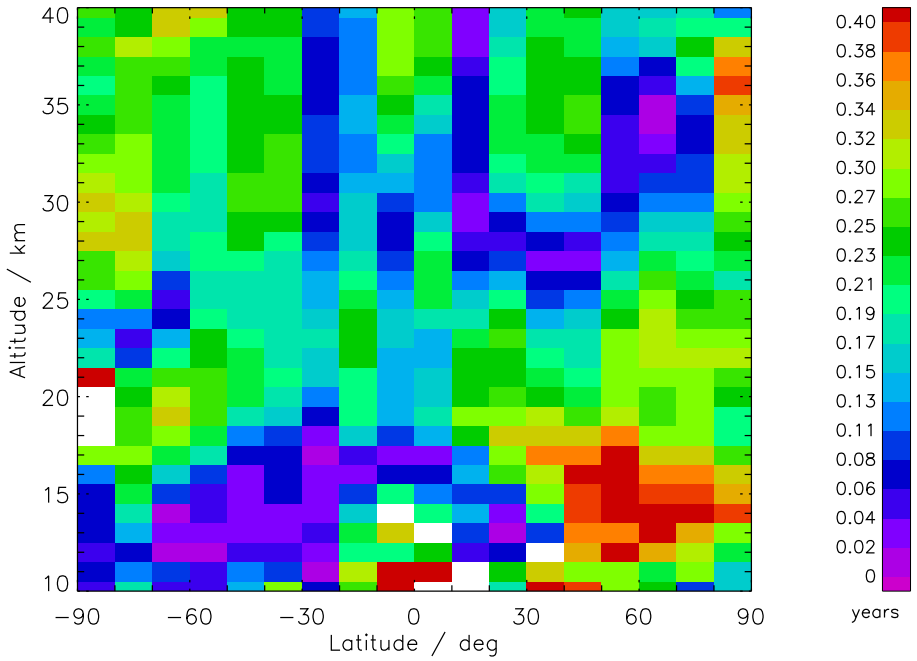

Figure 8.20: Altitude–latitude cross sections of amplitudes of the QBO variation of mean age of air.

In the tropics below approximately 28 km air is youngest in boreal winter, even in the Southern Hemisphere (except for altitude–latitude bins below 20 km) and confirms, that tropical upwelling is strongest in northern hemispheric winter [e.g. Rosenlof, 1995]. The hemispheric difference is small, which was also noticed by Stiller et al. [2012]. However, this minimum in AoA in the southern tropics occurs approximately 2 months later in the new MIPAS data. In the Northern Hemisphere air is oldest in late summer, while it is oldest in austral spring to early summer in the Southern Hemisphere. Furthermore this maximum in AoA in the southern tropics occurs 2 months earlier in the new MIPAS data set compared to the previous one.

The amplitude of the QBO signal in AoA is shown in Figure 8.20 for all latitudes and altitudes under assessment. In the publication Haenel et al. [2015] prior to this thesis highest amplitudes of the QBO variation were found in the upper polar stratosphere, as well as in the northern lowermost extratropical stratosphere. In that study also the 2-year cycle was included in the multilinear regression model (see beginning of this Chapter). Because the period of the QBO is also approximately 2 years, the QBO- and the sinusoidal terms representing the 2-year cycle became linearly dependent and compensated each other. This effect artificially caused high amplitudes in the QBO- and 2-year oscillation signal. As mentioned above, in the analysis of this thesis,

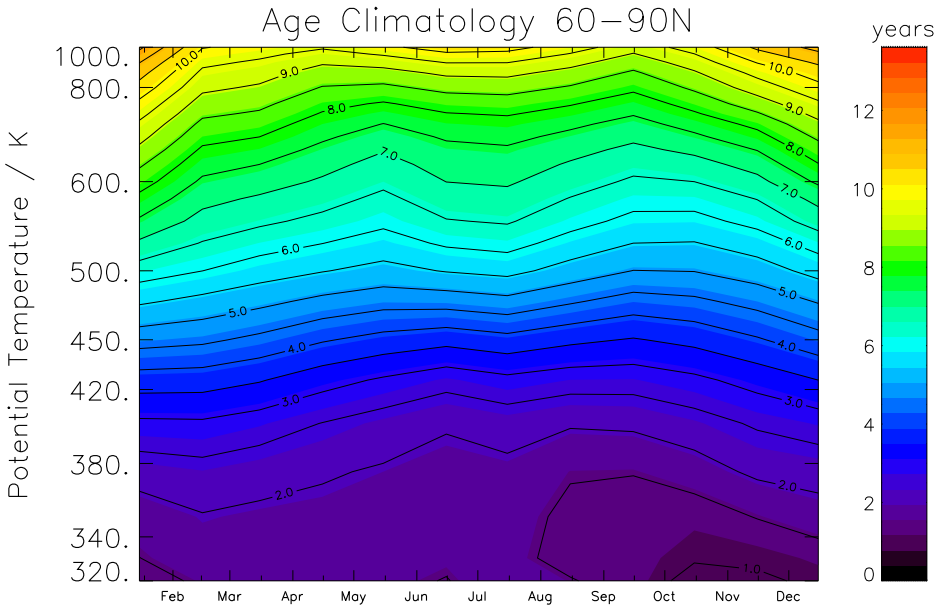

Figure 8.21: MIPAS climatology of the seasonality of AoA for the northern high latitudes. Non-equidistant potential temperature was used as the vertical axis.

sinusoidal terms with periods higher than 1 year have been omitted, so that interference of the QBO- and the 2-year oscillation is inhibited. The revised distribution of QBO amplitudes is now considered to be more realistic. High amplitudes can still be found in the northern upper polar stratosphere [80°-90° N, 30-38 km] and in the southern middle polar stratosphere [70°-90° S, 28-31 km], but they are much lower now than in Haenel et al. [2015]. In general the southern midlatitudinal and polar stratosphere [30°-90° S, 18-40 km] exhibits a contiguous region of elevated QBO amplitudes. However, highest QBO amplitudes remain now in the northern lowermost extratropical stratosphere. An explanation of this phenomenon is still pending.

Figures 8.21 to 8.25 have been created to compare the AoA seasonality observed by MIPAS with AoA simulations with the CLaMS model as published in Konopka et al. [2015] (Figures 8.23 and 8.26). In a first step MIPAS AoA needed to be calculated on a potential temperature grid using MIPAS temperature and pressure data. Then a climatology was built for the whole MIPAS period. Figures 8.21 and 8.22 show the vertical structure for the northern and southern polar latitudes. In order to be comparable with the respective figures in Konopka et al. [2015], the same non-equidistant potential temperature was used as a vertical axis, i.e. the entropy density $s = c_p \rho \; ln(\theta/\theta_0)$ from a standard atmosphere was used here as a scaling factor to magnify the UTLS-region. The youngest air in the northern high latitudes just above

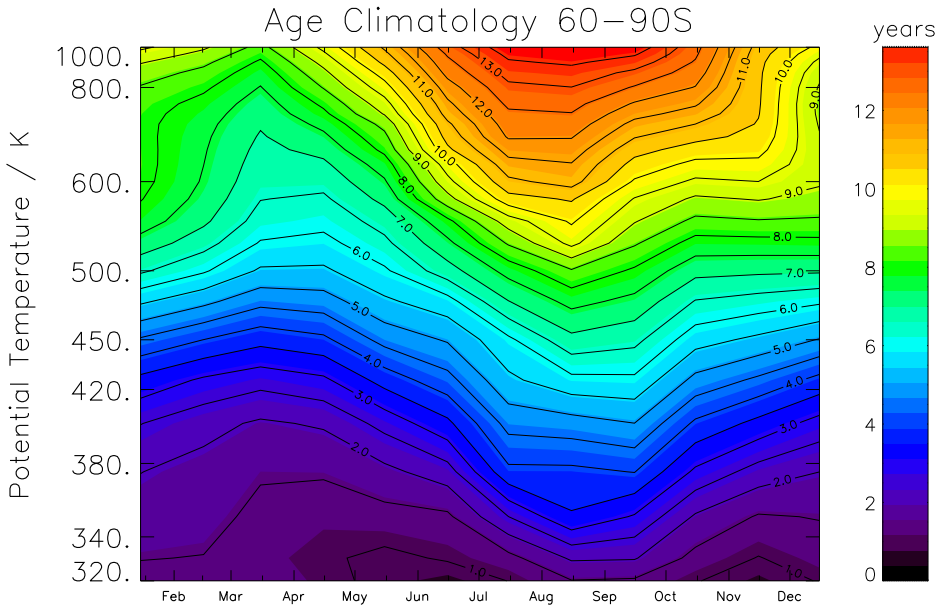

Figure 8.22: MIPAS climatology of the seasonality of AoA for the southern high latitudes. Non-equidistant potential temperature was used as the vertical axis.

the tropopause with $\Theta \approx 380\,\mathrm{K}$ is observed during August and September like in the simulations with the CLaMS model. However, this peak in MIPAS is shifted towards September to October in higher altitudes and the isolines develop more towards a double peak structure around 600 K, with a second peak of young air appearing in spring hinting at a semiannual oscillation in AoA.

The CLaMS AoA seasonality does not reflect these double peaks of young air, however its peak is shifted from late summer in the UTLS towards spring at around 600 to 700 K. The oldest air at around 800 to 1000 K ($\approx$ 29-33 km) is observed in December/January, whereas it appears from September to December in the CLaMS model. The maximum in AoA in the MIPAS climatology is found during February and March in the UTLS-region, which was already diagnosed in Figure 8.19. This is also reproduced in the CLaMS model.

The seasonal cycle in the Southern Hemisphere south of 60°S (Figure 8.22) is much stronger, as already diagnosed in Figure 8.17, and is shifted by approximately 6 months compared to the Northern Hemisphere. The oldest air occurs around August and September at almost all potential temperature levels, while the minimum of AoA is observed during early April (fall on SH). This basic pattern of the seasonality in the Southern Hemisphere is reproduced in the CLaMS model (Figure 8.23, bottom panel). However, the shift of the AoA maxima and minima between the UTLS and

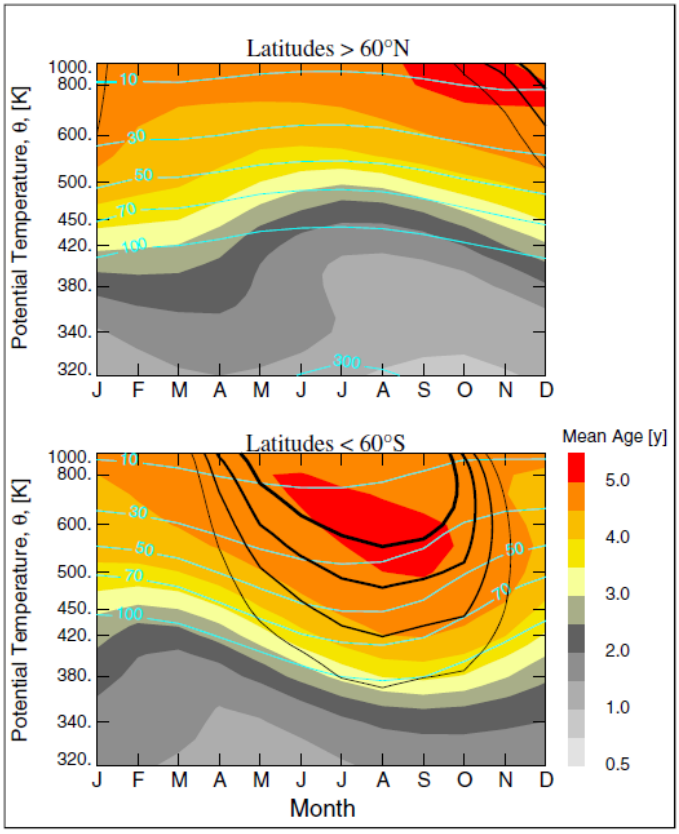

Figure 8.23: Seasonality of AoA simulated with the CLaMS model for the northern high latitudes (upper panel) and for the southern high latitudes (lower panel). Non-equidistant potential temperature was used as the vertical axis. The black lines represent isolines of the zonal wind and the cyan lines are isobars (figure from Konopka et al. [2015] by courtesy of AGU).

the stratosphere above is more pronounced in the CLaMS data. The minimal AoA just above the tropopause with $\Theta \approx 380\,\mathrm{K}$ is about the same in the Northern and the Southern Hemisphere for MIPAS, while CLaMS simulates a hemispheric asymmetry of about 0.5-1 years here. However, at the AoA maximum in hemispheric late winter, air is about 1.5 years older at $\Theta \approx 380\,\mathrm{K}$ in the southern than in the northern high latitudes in the MIPAS data compared to the respective difference of about 1 year in the CLaMS data (Figure 8.23). At 600 K in the MIPAS data air is again about the same age in the northern and southern polar stratosphere during its minimum, but about 2 years older in the south at the maximum of AoA. In the AoA maxima around 1000 K, the Southern Hemisphere is more than 2 years older than during the same season in the Northern Hemisphere, but it is even about one year younger in austral autumn. The amplitude of the seasonal cycle is more than 2.5 years in the Southern

polar latitudes for MIPAS AoA, which was already found in Figure 8.17.

In summary the general patterns of the seasonality in AoA in high latitudes simulated by the CLaMS model are confirmed with the MIPAS data. The modelled asymmetry between the Northern and Southern Hemisphere in the absolute values of AoA is also observed in the MIPAS data, but in addition, MIPAS detected a much larger amplitude of the seasonal cycle in the Southern polar region. Overall, the absolute values in both hemispheres are biased low in CLaMS compared to the MIPAS data.

The latitudinal distributions of AoA on two isentropes are shown in Figures 8.24 and 8.25 and compared in the following with Figure 8.26 (Figure 3 in Konopka et al. [2015]). At 400 K, which represents an altitude directly above the tropopause, oldest air is observed in the southern polar region from midwinter to the beginning of spring consistent with the discussion of Figure 8.22. This maximum in the AoA climatology is nicely reproduced in the CLaMS model. It is transported downward to 350 K in the MIPAS as well as in the CLaMS data. (For technical reasons the MIPAS climatology was built on a potential temperature of 350 K, whereas the CLaMS climatology is presented on 340 K.) On this level the AoA maximum in the southern high latitudes appears to be shifted slightly towards spring in the ClaMS data. The seasonal cycle in the northern high latitudes at 400 K is shifted by approximately 6 months and is much less pronounced than in the Southern Hemisphere, which is in accordance to the discussions above. This hemispheric asymmetry is also found in the CLaMS data, however it is more evident in the MIPAS data.

In the tropics seasonal differences in MIPAS and CLaMS AoA at 400 K are much smaller, but still discernible with oldest air during late summer to fall and youngest during winter to the beginning of spring in the Northern Hemisphere. As stated in Konopka et al. [2015] and in the previous discussion of this section this can be attributed to the seasonality of the subtropical jet as a mixing barrier between the tropics and extratropics, which almost vanishes during summer and allows old air from higher latitudes to penetrate into the tropics. In addition, these observations are in accordance with the seasonality of the BDC, being strongest in northern hemispheric winter. In the southern tropics the MIPAS seasonal cycle is again shifted by about half a year with oldest air during December to February and younger air during austral winter, which is consistent with Figures 8.18 and 8.19 (400 K corresponds to an altitude of approximately 18 km in the tropics). This maybe an indication that in the southern tropics enhanced mixing in austral summer (boreal winter) outweighs the decrease of AoA due to the maximum of tropical upwelling in northern hemispheric winter. A

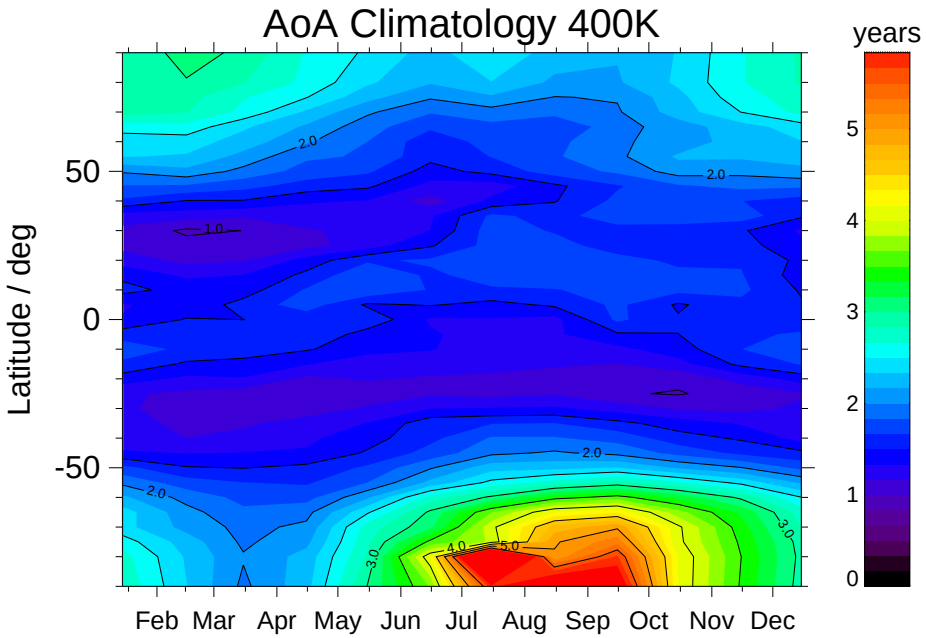

Figure 8.24: MIPAS climatology of the seasonality of AoA over latitude at a potential temperature of 400 K

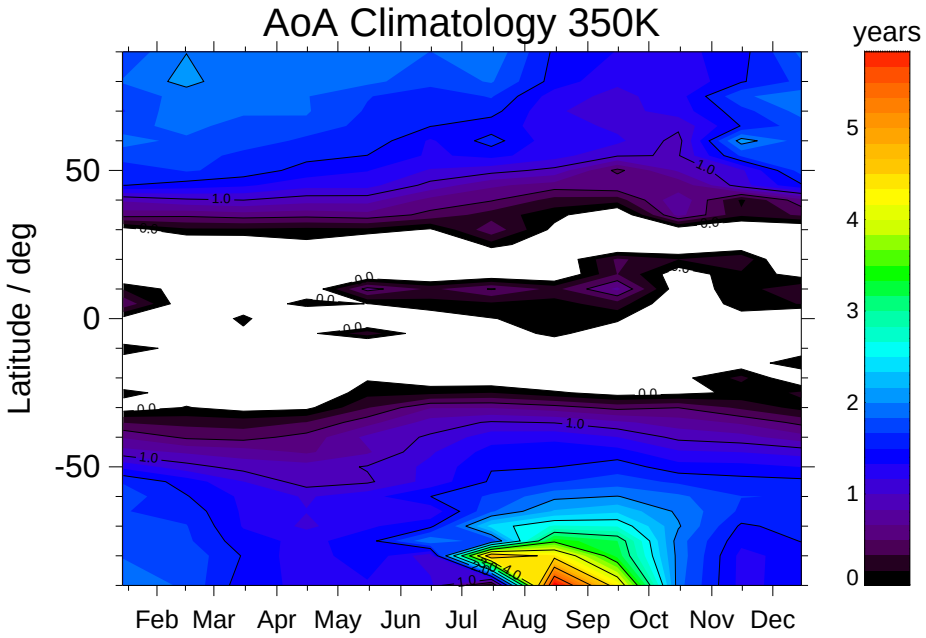

Figure 8.25: MIPAS climatology of the seasonality of AoA over latitude at a potential temperature of 350 K

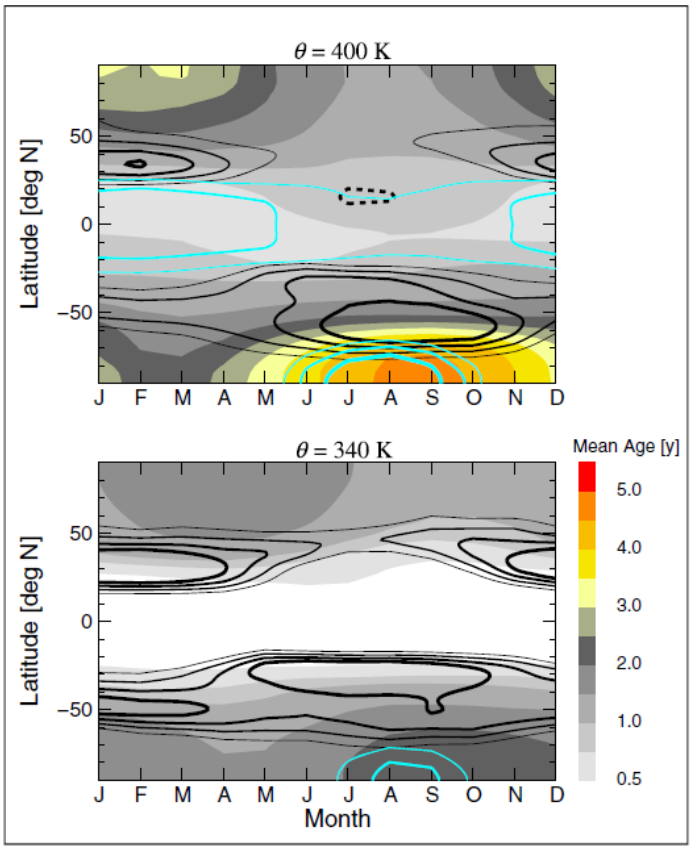

Figure 8.26: Seasonality of AoA simulated with the CLaMS model at a potential temperature of 400 K (upper panel) and 340 K (lower panel). The black lines represent isolines of the zonal wind (15, 20, 25, and 30 m/s) whereas the cyan lines represent temperatures (198, 194, and 190 K) from thin to thick, respectively (figure from Konopka et al. [2015] by courtesy of AGU).

characteristic feature of the MIPAS data set seems to be that youngest air above the tropopause (400 K) is observed between 20°-30° N/S rather than in the inner tropics, which would mean that strongest upwelling of tropospheric air is observed in the subtropics. However, this feature is not confirmed by the CLaMS model data, even though it has been observed in ERA-Interim data and corroborated by simulations e.g. with the Hadley Centre Global Environmental Model (version 2) [Osprey et al., 2013] (their Figure 6) or with a multi model mean as in [Hardiman et al., 2014] (their Figure 5). At 30°N youngest air at 400 K is observed in the end of winter to spring, slightly shifted compared to the inner tropics, where the maximum of upwelling is expected during winter. Around 30°S the minimum of AoA is also observed during spring, in addition a second AoA minimum occurs in February to April. This again could be caused by the intricate interplay between the seasonality of tropical upwelling and in-mixing of

older extratropical air. At 350 K these areas of minimum age decrease even below zero, which means that MIPAS detected higher SF_6 vmrs than the reference value. In accordance to the definition of AoA, the CLaMS model yields an age of zero at 340 K in the tropics.

In general, the main features and patterns of the MIPAS AoA climatologies (Figures 8.24 and 8.25) are reflected well by the CLaMS simulations.

8.4 The seasonality of the trend

In this section the seasonality of the MIPAS AoA trend is analysed, i.e. the trend analysis described in Sections 8.1 and 8.1.1 is carried out separately for every month. In a first step, AoA time series have been constructed comprising only data points of a certain month, for instance all Januaries covered by the MIPAS period. Such AoA time series were built for each month. In a second step, the linear regression model described above was fitted to the time series to infer a decadal trend for every latitude/altitude bin and every month. Because the only data points of the selected month were considered in the analysed time series, the distance of two adjacent data points is always exactly one year. Therefore it does not make sense to include oscillations with periods of one year or even overtones of the seasonal cycle in the regression model. However, the QBO was considered in the fit and the interannual variability seemed to be largely induced by the QBO, which was also reported by Ploeger and Birner [2016]; Ploeger et al. [2015b] in their study with the CLaMS model. The resulting 12 trend patterns are shown in Figures 8.27 and 8.28.

The largest all-year positive AoA trend, observed in the southern polar stratosphere (Figure 8.4), seems to be mainly caused by strong AoA increase between May and December, while during January, February and March (i.e. southern polar summer) weaker linear increase is observed. During April no significant trend could be detected, which means that the linear growth of AoA in the southern polar stratosphere has almost come to rest during that month.

Contrary to that, the upper northern polar stratosphere exhibits a positive trend during January to April, while during the rest of the year (from May to December) small positive, insignificant or even negative trends have been observed, which results in an overall weak positive trend, being not significant in most parts of the upper northern polar stratosphere.

This suggests that the positive AoA trend in the upper polar stratosphere is mainly driven by processes during hemispheric winter to spring, being especially enhanced and

enduring in the Southern Hemisphere and increasing over time. A possible candidate could be the downward transport of SF_6-depleted air from the mesosphere into the polar stratosphere during winter, which seems to be particularly pronounced in the Southern Hemisphere [e.g. Funke et al., 2005]. As the abundance of SF_6 has continuously increased in the troposphere due to anthropogenic activity it has also increased in the stratosphere and mesosphere. The major SF_6 loss reaction (see Section 2.5) is electron capture and its rate constant is therefore dependent on the concentration of SF_6 and free electrons. This implies that a higher abundance of SF_6 leads to a higher depletion of SF_6 in the mesosphere. Being transported downward during winter, this could explain the large AoA trend in the polar region during this time of the year, which is, however, not real, but an artefact caused by the SF_6 sink. To answer the question, whether the SF_6 depletion in the mesosphere is indeed responsible for the large AoA trends observed in the MIPAS data in these regions of the stratosphere, a model study comparing the AoA trends calculated with a "reactive SF_6 tracer" and a reference calculation with a "clock tracer" would be necessary.

The negative trend pattern in the Southern Hemisphere observed in Figure 8.4 is present in every month in Figures 8.27 and 8.28, which means that AoA has continuously decreased in this region over the period 2002-2012, however, it is most pronounced in April and May, as well as in November. In April and May also large parts of the southern and northern lower and lowermost stratosphere exhibit a linear decrease in AoA. The AoA in these regions is strongly determined by two-way mixing [Ploeger et al., 2015a] and the shallow branch of the BDC.

The northern midlatitudes, i.e. the region where Engel et al. [2009] observed a slight, but non-significant positive AoA trend, appear also with a slight positive or insignificant trend during most times of the year.

Another interesting region is the northern extratropical lowermost stratosphere (<20 km, 30°-60°) which exhibits extremely strong positive trends during August, i. e. a time when this regions is usually "flushed" with young air from the tropics (see Section 8.3). This may hint at a weakening of the mixing processes during that time of the year.

Other striking results are the strong negative AoA trends in the upper northern polar stratosphere during May and September/October which accompanied with strong positive trends in winter hint towards an enhancing seasonal cycle over time.

Also noticeable is the decrease of AoA in the middle and lower northern polar stratosphere during January and February which could be attributed to either less strong subsidence or frequent stratospheric warmings.

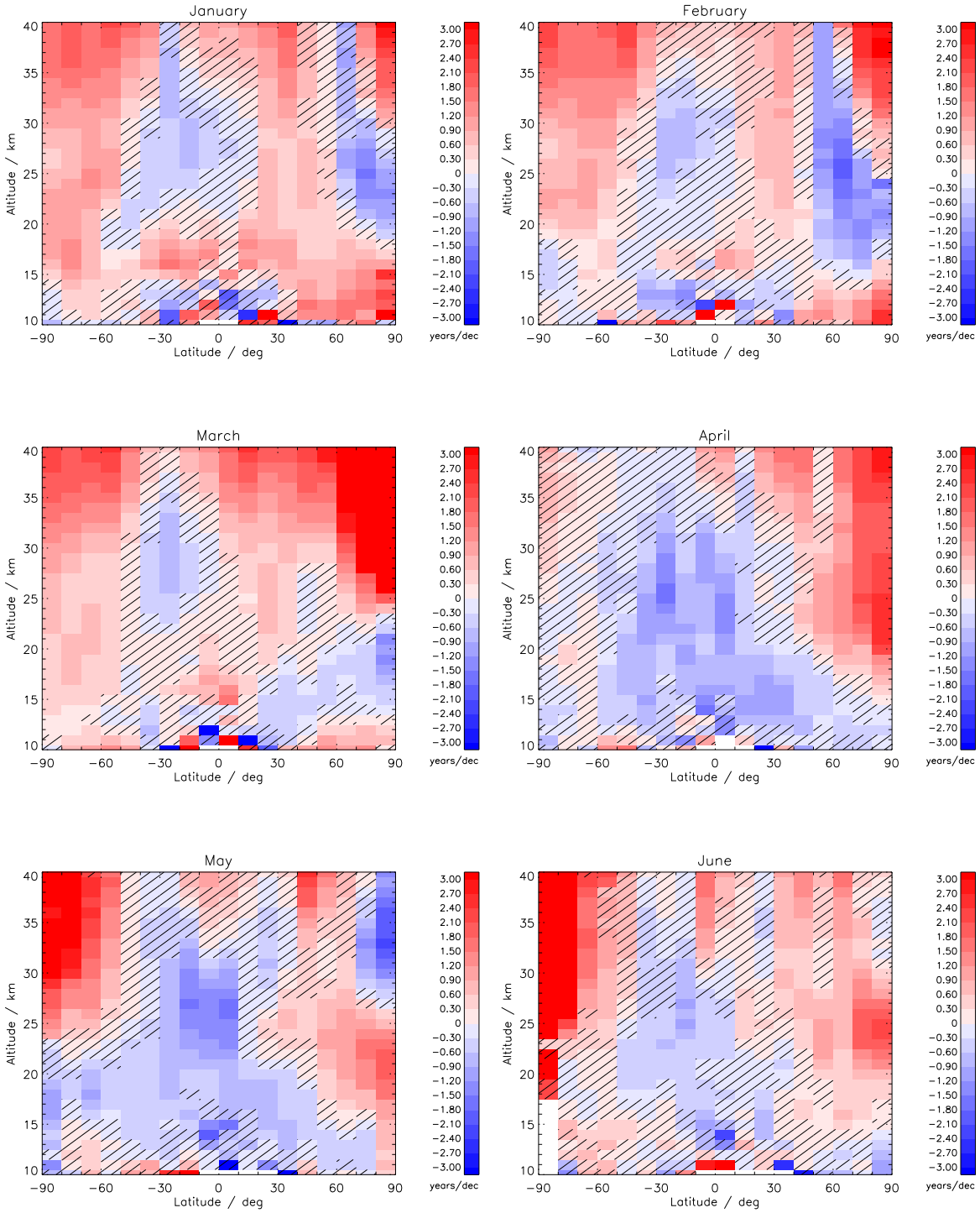

Figure 8.27: MIPAS AoA trends considering every month separately, from January to June. Hatched areas indicate where the trend is not significant.

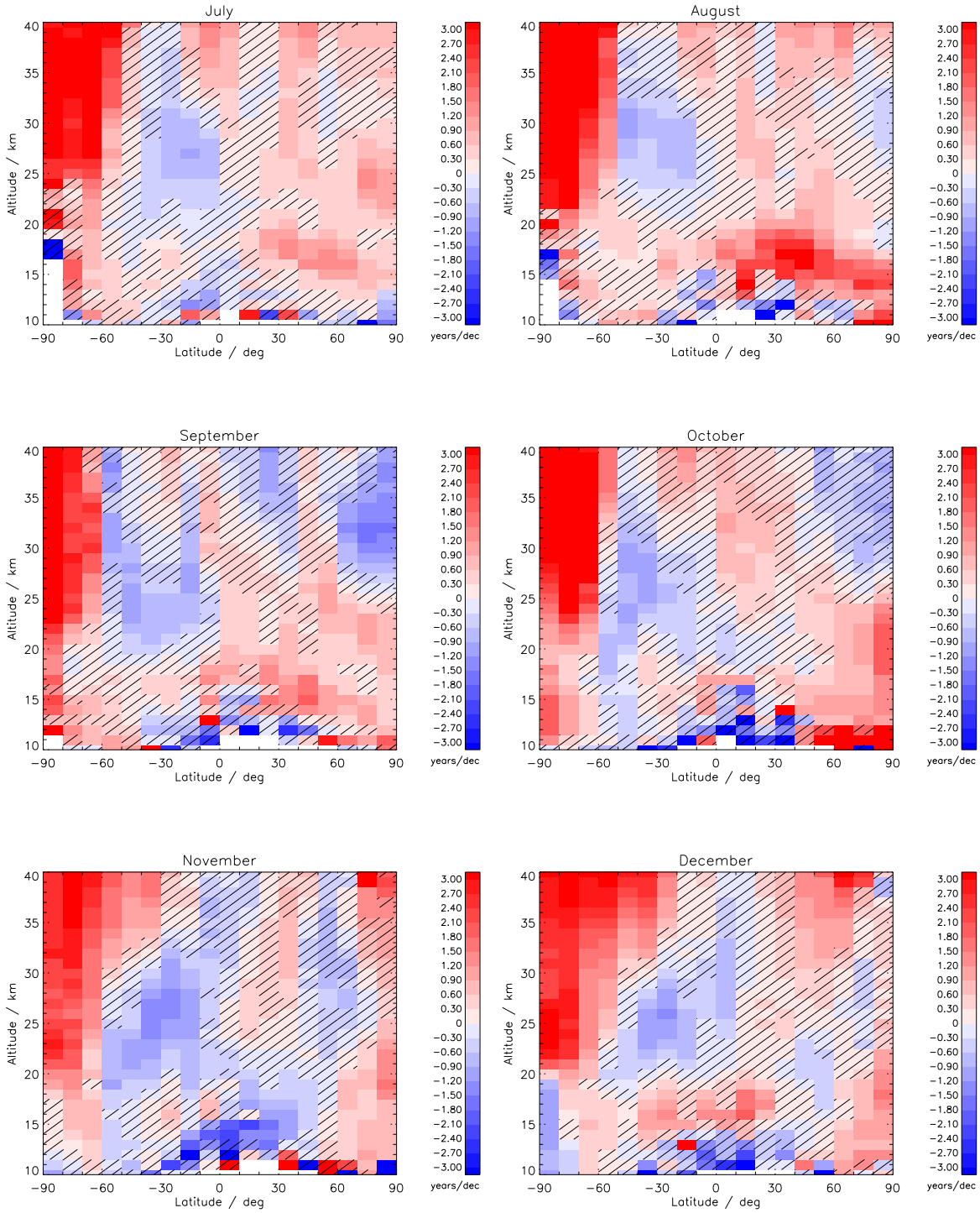

Figure 8.28: MIPAS AoA trends considering every month separately, from July to December. Hatched areas indicate where the trend is not significant.

Chapter 9

Comparison with independent data

9.1 Age of air trends from ACE-FTS

Inferring AoA trends from ACE-FTS SF_6 is very challenging, since measurements are very sparse. For this comparison ACE-FTS SF_6 measurements of version 3.5 with quality flag lower than 4 have been used (for more details concerning the quality flag see e.g. Sheese et al. [2015]). At first ACE-FTS SF_6 measurements were condensed into monthly zonal means as done with the MIPAS measurements. In a second step these mean SF_6 profiles were interpolated on the MIPAS altitude grid. Then these profiles were converted into AoA following the same procedure as with the MIPAS data described in Section 6.2. In the final step the AoA trends over the MIPAS measurement period were calculated in the same manner as for the MIPAS data (see Section 8.1 and 8.1.1).

Since the number of ACE-FTS measurements is very limited and much less than the MIPAS measurements available, especially in the tropics, it was decided to use a coarser latitude binning: The tropics have been condensed into two 30°-latitude bins, ranging from the equator to 30° N and S, respectively, while the other regions have been compiled into 20°-latitude bins. This way each monthly zonal mean contains more measurements, which in turn decreases the standard error of each mean and therefore decreases the propagated error on the estimated trend, which increases the significance of the trend. In addition, another problem occurred while calculating the ACE-FTS AoA trends in each latitude-altitude bin: Due to the sparseness of the ACE-FTS measurements oscillations with periods less than half a year in the multilinear regression model (see Section 8.1) could not successfully be fitted to the ACE-FTS data points and led to unrealistically high amplitudes. Therefore the overtones with periods of 3 and 4 months have been omitted in the analysis, and only the annual,

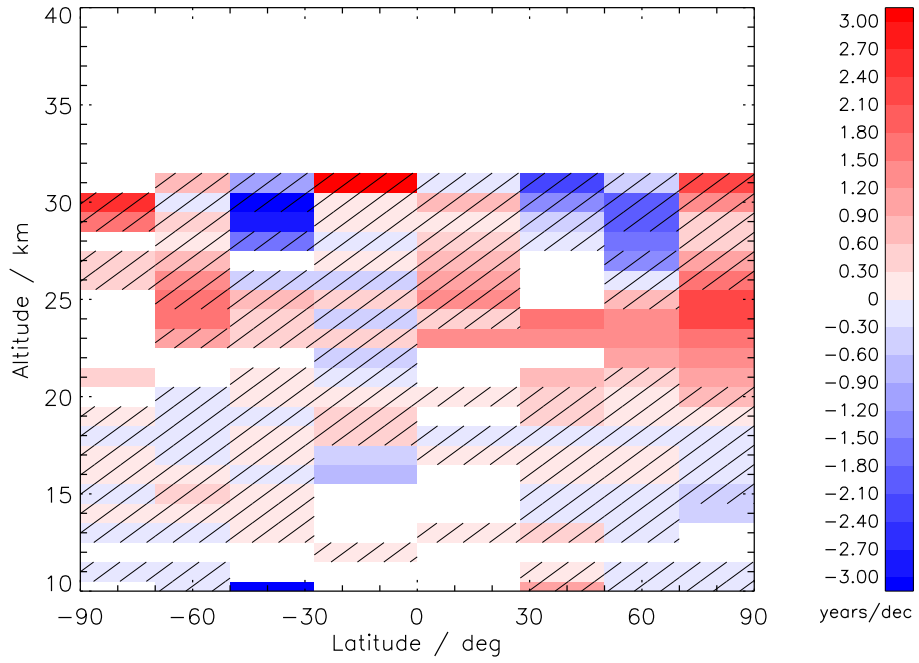

Figure 9.1: Age of air trends (model-error corrected) from ACE-FTS. Hatched areas indicate where the trend is not significant.

semiannual and QBO cycle was considered. The result is shown in Figure 9.1.

Most inferred trends are not significant (on the 2σ level), however, the Northern Hemisphere exhibits significant positive trends at an altitude of 20 to 25 km and confirms the findings with the MIPAS instrument as well as the balloon-borne measurements of Engel et al. [2009].

9.2 Comparison with model simulations

9.2.1 CLaMS

Figure 9.2 shows the comparison between MIPAS AoA trends and trends simulated with the CLaMS model driven by ERA-Interim data for the same period (2002-2012) as published in Ploeger et al. [2015b]. CLaMS AoA trends have been calculated using a "clock tracer" (see Section 2.4). The trend patterns (in terms of percentage changes per decade) are only compared up to an altitude of approximately 28 km and on latitudes ranging from 60°S to 60°N and are plotted on potential temperature as the vertical axis. In addition, this plot shows MIPAS AoA trends as derived in Haenel et al. [2015], which used a different multilinear regression model including more sinusoidal terms (see Chapter 8). For these reasons the MIPAS AoA trends appear slightly different from

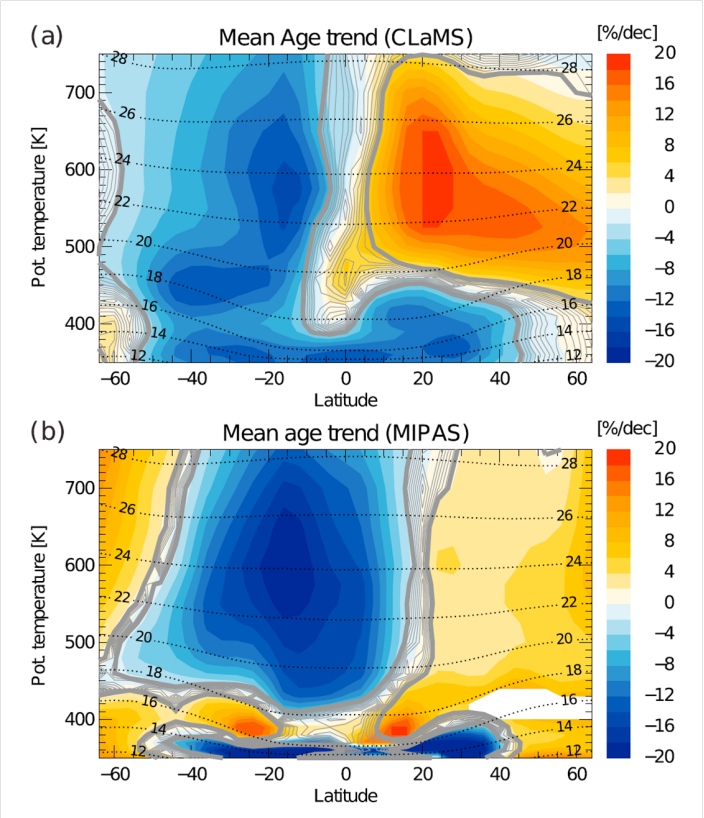

Figure 9.2: Age of air trends from CLaMS compared to MIPAS (figure from Ploeger et al. [2015b])

those shown in Figures 8.2 and 8.4. In addition, the trends for CLaMS have been derived with a different method as done for the MIPAS trends in this thesis.

The dipole-like structure of negative trends in the Southern Hemisphere and positive trends in the Northern Hemisphere in the MIPAS data is nicely confirmed with the CLaMS model. As stated in Ploeger et al. [2015b], however, the northern hemispheric increase in AoA is stronger in the model, whereas the AoA decrease in the Southern Hemisphere appears stronger in the MIPAS data. In addition, the zone of linear decrease extends into the northern tropics in the observations, while the trend pattern changes sign approximately at the equator in the model. The positive trend south of 50°S in the MIPAS data is likely due to the mesospheric SF_6 sink, as supposed by Ploeger et al. [2015b] and further discussed in Section 8.4. Another difference between modelled and observed trends is found in the lower stratosphere, where CLaMS consistently exhibits negative trends below 450 K, which appears in the MIPAS data further down (below 400 K). As pointed out by Ploeger et al. [2015b], even though there are some differences in the decadal trends between the model and the MIPAS observations, the similarities in the trend pattern are an encouraging result and indi-

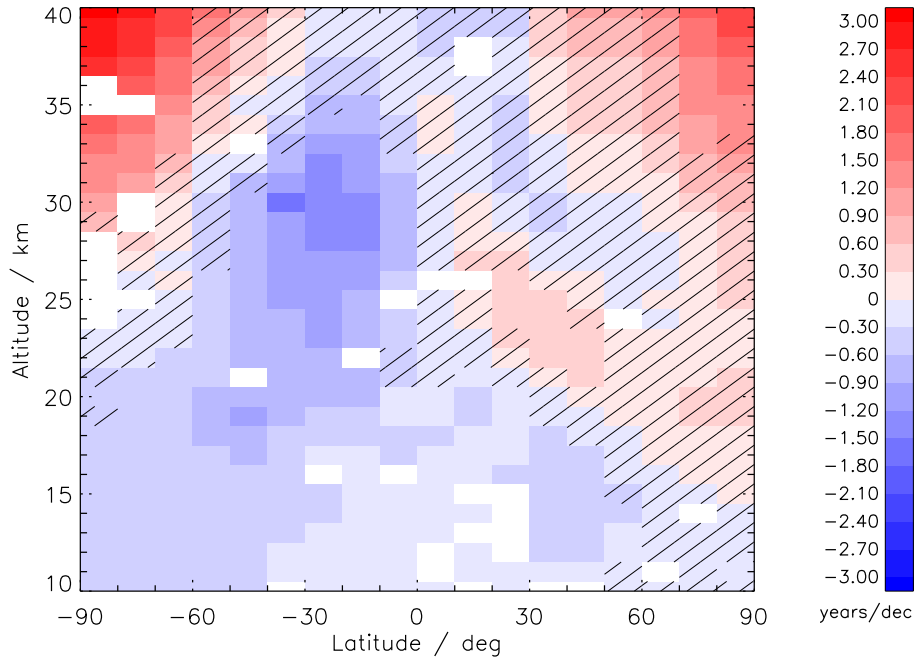

Figure 9.3: Calculated AoA trends for 2002–2012 from the KASIMA model with consideration of empirical errors and autocorrelation. Hatched areas indicate where the trend is not significant.

cate that stratospheric transport is well described by ERA-Interim data used to drive the model.

9.2.2 KASIMA

The MIPAS SF_6-based AoA trends for 2002–2012 are compared with trends derived from SF_6 distributions calculated with the Karlsruhe Simulation Model of the Middle Atmosphere (KASIMA) (see Kouker et al. [1999]; Reddmann et al. [2001, 2010]; Ruhnke et al. [1999] for a description of the model and some applications). Here the model in the configuration as described in Reddmann et al. [2001] but with a T42/L63 configuration corresponding to about $2.84° \times 2.84°$ horizontal resolution and 63 vertical levels between 7 and 120 km was used. In addition, the model was nudged to ERA-Interim analysis below 1 hPa. SF_6 mixing ratio values were set at the lower boundary of the model in the troposphere using NOAA/ESRL data. Note that the model includes the mesospheric loss of SF_6, which is implemented in the model according to Reddmann et al. [2001]. Previously, Stiller et al. [2008] showed that the apparent high mean age values in late polar stratospheric winter observed in MIPAS observations can only be reproduced by the model simulations when including mesospheric loss.

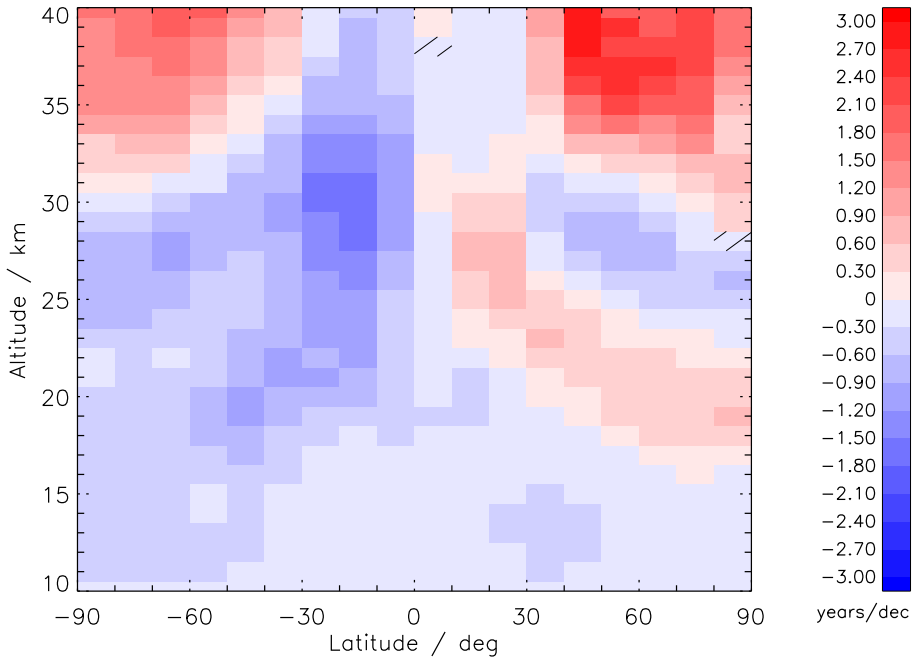

Figure 9.4: Calculated AoA trends for 2002–2012 from the KASIMA model without consideration of empirical errors and autocorrelation. Hatched areas indicate where the trend is not significant.

Figure 9.3 shows the distribution of AoA trends calculated with simulated SF_6 values from the KASIMA model as latitude–altitude cross section with consideration of empirical errors and autocorrelations.

The model results agree remarkably well with the observed AoA trends: positive decadal trends are found in the upper polar stratosphere in both hemispheres and at northern midlatitudes around 20 to 25 km while negative trends are found in the southern tropics and southern subtropics as well as in both hemispheres in the lower and lowermost stratosphere at midlatitudes, and in the southern polar region. The most pronounced negative trend is detected in the southern subtropics around 25 to 30 km, whereas it is found around 25 km in the MIPAS measurements. At northern midlatitudes at about 25 to 30 km altitude a tongue of negative trends is modelled, while MIPAS detected still weak positive trends there. At first glance there seems to be no disagreement between MIPAS and KASIMA in this region, because negative trends in KASIMA are not significant there. However, one has to be careful with the significances when comparing MIPAS and KASIMA: KASIMA is a nudged model, i.e. in wide parts of the atmosphere it represents the real atmosphere. This implies that the atmospheric variability patterns of KASIMA and MIPAS which are responsible for the error of the multilinear model share certain components and therefore cannot be

assumed as fully uncorrelated. Thus, this error characterises the expected difference between the regression function and truth; however, it cannot necessarily account for the differences between MIPAS and KASIMA. For this comparison the trends without consideration of the model errors may be more adequate. Figure 9.4 shows the AoA trends from the KASIMA model without consideration of the model errors and demonstrates that the region of the "negative tongue" is significant in KASIMA, whereas it is significantly positive in MIPAS (compare with Figure 8.2).

At high latitudes lower stratospheric trends are positive in the MIPAS but negative in the KASIMA data set. These trends are not significant for MIPAS; however, they are significant when comparing the respective figures of trends without consideration of the model error (Figures 9.4 and 8.2). So there is indeed a discrepancy in this region, which is most likely due to the "overaging" effect, which is more pronounced in the measured data because KASIMA underestimates polar winter subsidence.

What is striking in Figure 9.3 is the hemispheric asymmetry between significant negative trends in the Southern Hemisphere and significant positive trends in the Northern Hemisphere, which was also found in the MIPAS data. This hemispheric asymmetry was also noticed by Monge-Sanz et al. [2013] with the TOMCAT model and by Mahieu et al. [2014] with the SLIMCAT model and was later also confirmed by Ploeger et al. [2015b] with the CLaMS model (Figure 9.2). All these models are driven by ERA-Interim data. However, CLaMS driven by JRA-55 data does not reproduce this pattern [Konopka et al., 2016].

Chapter 10

Discussion and Conclusion

In this work the SF_6 retrieval setup for MIPAS-ENVISAT spectra has been improved over the one developed by Stiller et al. [2012] and a newer version of spectra provided by ESA (level 1b data, version 5.02/5.06) was used to retrieve global profiles of the trace gas SF_6. Monthly zonal means were converted in AoA using a tropospheric reference curve. The new AoA data set roughly resembles that of Stiller et al. [2012] but shows differences with respect to important details. Some spurious features of the old data set do no longer appear in the new data set. In particular, the new data set does not show the local AoA minimum at 36 km in the tropics, which is identified as a retrieval artefact of the previous version and could be eliminated by a refined consideration of continuum radiation. A possible high bias of the old AoA data set above 40 km has been removed by a more sensible application of profile regularisation in the retrieval and by applying a full non-LTE treatment of the interfering CO_2 lines.

The global data set of age of air covering a period of 10 years is robust and consolidated enough to allow, for the first time, a detailed study of the stratospheric circulation. The latitudinal and altitudinal dependence of AoA, the seasonal variation (amplitudes and phases), and the impact of the QBO on the circulation could be studied for the first time for a whole decade. The data set is an invaluable tool for validation of the circulation modelling in reanalysis, chemistry transport and chemistry climate models.

The latitudinal cross section of AoA at 20 km was compared to airborne observations from the 1990s and no substantial differences to the previous comparison of Stiller et al. [2012] were found. The comparison of AoA profiles with airborne measurements shows that in the tropics MIPAS AoA is now older at all altitudes. At northern midlatitudes MIPAS agrees with most of SF_6 in-situ data whereas at high northern latitudes MIPAS AoA is again older, and only the SF_6 air samples inside the polar

vortex agree with the MIPAS data. It cannot be decided from the available data if these discrepancies are due to a changed circulation (e.g. increased mixing over the subtropical transport barriers) or due to different measuring systems.

The temporal variability of AoA over the 10 years of MIPAS measurements (2002–2012) was analysed by fitting a regression model to the AoA time series. The annual cycle in AoA of particular regions in the stratosphere was investigated and found to be in good agreement with specific model studies.

The derived AoA decadal trends show a pronounced hemispheric asymmetry above the lowermost stratosphere. The results of Stiller et al. [2012] were confirmed with respect to the typical values and the general morphology. The overall picture of linear increase/decrease in the latitude–altitude plane, however, is more contiguous and less patchy with the new data. Positive linear trends were confirmed for the northern midlatitudes and southern polar middle stratosphere whereas negative trends were confirmed for the lowermost tropical stratosphere and lowermost southern midlatitudinal stratosphere. Differences to the previous data set occur in the northern polar upper stratosphere, where trends are now positive, and in the middle tropical stratosphere, where trends are now negative. The latter might be explained by the removal of the retrieval artefact which changed the shape of the AoA profile in the tropics considerably. The linear increase in the southern and northern polar stratosphere and in the northern midlatitudes can be considered as robust results. The significant positive trend in the northern midlatitudes is in agreement with the findings of Engel et al. [2009] and the inferred trends agree impressively well with the estimated trend by Engel et al. [2009].

The hemispheric asymmetry in AoA found in the MIPAS data for the period 2002-2012 is nicely confirmed by simulations with the CLaMS model, driven by ERA-Interim data, for the same time period.

The comparison with the KASIMA model for the period 2002–2012 shows that the linear increase in the upper polar stratosphere and in the northern midlatitudes can be reproduced in the model at least when data are sampled and analysed in the same manner as the MIPAS data. It demonstrates that the ERA-Interim data, used to nudge KASIMA, apparently are able to reproduce the observed transport trend, which shows that they are suitable for studies of the BDC and its trends. It also demonstrates that models which are driven by ERA-Interim meteorological reanalysis (like CLaMS) or are nudged to them (like KASIMA) can reproduce the general morphology of AoA trends observed with MIPAS.

The refined MIPAS observations on AoA in this study disagree with the results of various studies with free-running models, which consistently predict a decreasing

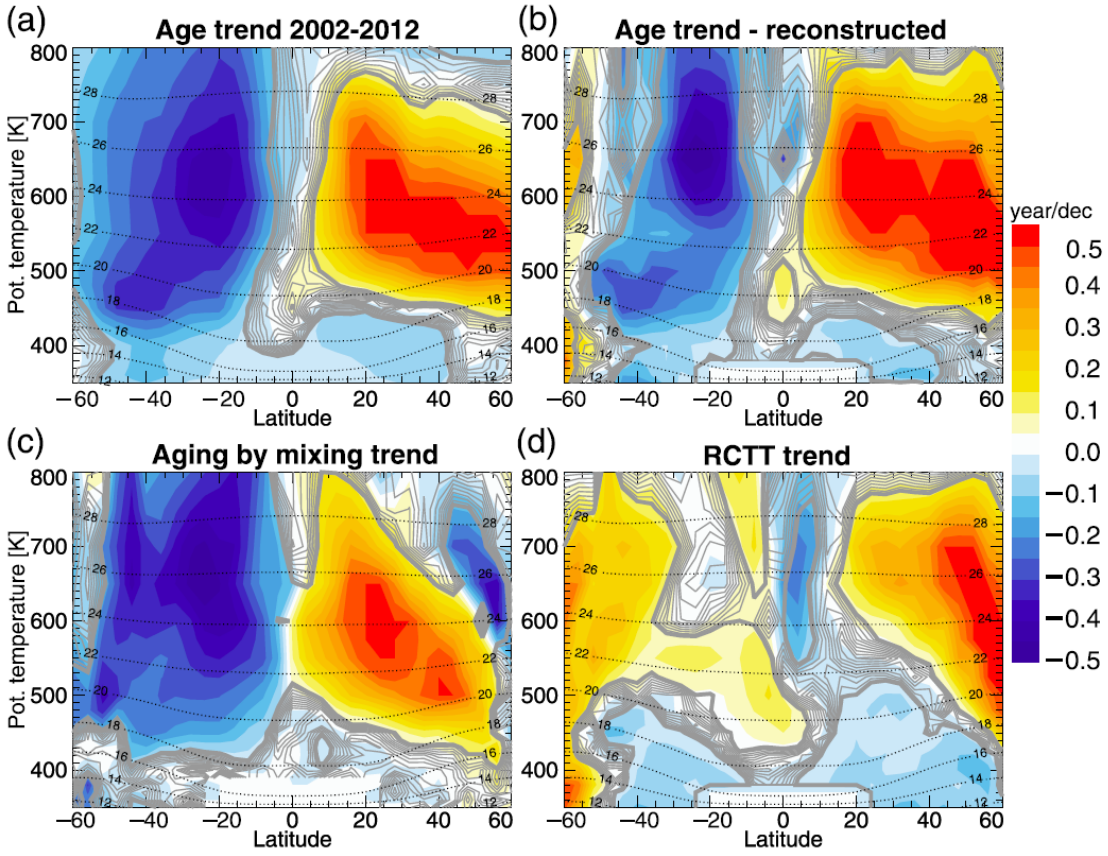

Figure 10.1: Trends for 2002-2012 simulated with the CLaMS model: (a) mean age of air, (b) mean AoA reconstructed as sum of residual circulation and mixing, (c) trend of aging by mixing, and (d) trend of RCTT. Gray shading indicates where trends are not significant at the 2σ level. Dashed lines mark altitude levels in km (figure from Ploeger et al. [2015a] by courtesy of AGU).

AoA for the whole stratosphere. However, the analysed time period in this thesis of approximately one decade is too short to be comparable with results from long-term model studies, since decadal variability is high [see e.g. Ploeger et al., 2015a].

Nevertheless this study finds a negative AoA trend in the tropics and in the lower and lowermost midlatitudinal southern stratosphere in agreement with long-term model studies and hence supports the idea of an increasing shallow branch of the BDC, which was also proposed by Bönisch et al. [2011] and supported by Diallo et al. [2012], at least in the Southern Hemisphere.

Ploeger et al. [2015a] show that the hemispheric asymmetry found in the CLaMS AoA trends during 2002 to 2012 is mainly caused by the trend in the integrated effect of mixing, also referred to as "aging by mixing" (see Section 2.4.2), rather than in trends of the residual circulation. Only below about 20 km the negative trends in mean age

are reflected in the trends of the residual circulation, meaning that in these regions the observed mean age trends can be attributed to the trends of the residual circulation transit time (see Figure 10.1). This corroborates the hypothesis of an accelerated shallow branch of the BDC, which is also supported by the MIPAS data (for the Southern Hemisphere). In turn, trends in the integrated effect of mixing (along the path of the residual circulation) can result from changes in the local mixing intensity or from changes of the residual circulation.

Ploeger et al. [2015a] also showed that AoA trends in CLaMS from 1990 to 2013 differ significantly from the decadal trends (2002-2012) presented here and are mainly negative throughout the stratosphere in accordance with climate model simulations, but also confirm the balloon-borne derived trends from Engel et al. [2009] as the AoA trends show insignificant to slight positive trends in northern midlatitudes above 24 km. (see their Figure 2). This hints towards a strong decadal variability in AoA trends and limits the possibility to extrapolate the MIPAS results towards other periods.

Even though, as mentioned above, the analysed time period in this study is relatively short, and inferred AoA trends might be influenced by decadal variability, the MIPAS observations presented in this thesis monitored decadal changes in stratospheric transport and has been proven suitable to validate model results, which in turn, could be further improved and eventually lead to a better understanding of the atmosphere and the climate system and improved prediction of future climate states. Still large uncertainties of the stratospheric response to a rapidly changing climate exist. It is therefore necessary to further monitor global changes in stratospheric dynamics and chemistry with satellite instruments like MIPAS.

References

A. E. Andrews, K. A. Boering, B. C. Daube, S. C. Wofsy, E. J. Hintsa, E. M. Weinstock, and T. P. Bui. Empirical age spectra for the lower tropical stratosphere from in situ observations of CO_2: Implications for stratospheric transport. *J. Geophys. Res.*, 104 (D21):26,581–26,595, 1999. 14

A. E. Andrews, K. A. Boering, B. C. Daube, S. C. Wofsy, M. Loewenstein, H. Jost, J. R. Podolske, C. R. Webster, R. L. Herman, D. C. Scott, G. J. Flesch, E. J. Moyer, J. W. Elkins, G. S. Dutton, D. F. Hurst, F. L. Moore, E. A. Ray, P. A. Romashkin, and S. E. Strahan. Mean ages of stratospheric air derived from in situ observations of CO_2, CH_4, and N_2O. *J. Geophys. Res.*, 106(D23):32,295–32,314, 2001a. doi: 10.1029/2001JD000465. 83

A. E. Andrews, K. A. Boering, S. C. Wofsy, B. C. Daube, D. B. Jones, S. Alex, M. Loewenstein, J. R. Podolske, and S. E. Strahan. Empirical age spectra for the midlatitude lower stratosphere from in situ observations of CO_2: Quantitative evidence for a subtropical barrier to horizontal transport. *Journal of Geophysical Research: Atmospheres*, 106(D10):10257–10274, 2001b. ISSN 2156-2202. doi: 10.1029/2000JD900703. URL http://dx.doi.org/10.1029/2000JD900703. 14

J. Austin and F. Li. On the relationship between the strength of the Brewer-Dobson circulation and the age of stratospheric air. *Geophys. Res. Lett.*, 33:L17807, 2006. doi: 10.1029/2006GL026867. 3

M. P. Baldwin, L. J. Gray, T. J. Dunkerton, K. Hamilton, P. H. Haynes, W. R. Randel, J. R. Holton, M. J. Alexander, I. Hirota, T. Horinouchi, D. B. A. Jones, J. S. Kinnersley, C. Marquardt, K. Sato, and M. Takahashi. The quasi–biennial oscillation. *Rev. Geophys.*, 39(2):179–229, 2001. 7

T. Birner and H. Bönisch. Residual circulation trajectories and transit times into the extratropical lowermost stratosphere. *Atmos. Chem. Phys.*, 11(2):817–827, 2011. doi: 10.5194/acp-11-817-2011. 2, 16

REFERENCES

K. A. Boering, S. C. Wofsy, B. C. Daube, H. R. Schneider, M. Loewenstein, J. R. Podolske, and T. J. Conway. Stratospheric mean ages and transport rates from observations of carbon dioxide and nitrous oxide. *Science*, 274(5291):1340–1343, 1996. doi: 10.1126/science.274.5291.1340. 83

H. Bönisch, A. Engel, J. Curtius, Th. Birner, and P. Hoor. Quantifying transport into the lowermost stratosphere using simultaneous in-situ measurements of SF_6 and CO_2. *Atmospheric Chemistry and Physics*, 9(16):5905–5919, 2009. doi: 10.5194/acp-9-5905-2009. URL http://www.atmos-chem-phys.net/9/5905/2009/. 14, 106

H. Bönisch, A. Engel, T. Birner, P. Hoor, D. W. Tarasick, and E. A. Ray. On the structural changes in the Brewer-Dobson circulation after 2000. *Atmos. Chem. Phys.*, 11(8):3937–3948, 2011. doi: 10.5194/acp-11-3937-2011. 4, 8, 9, 127, 143

G. Brasseur and S. Solomon. *Aeronomy of the Middle Atmosphere–Chemistry and Physics of the Stratosphere and Mesosphere*. Atmospheric and Oceanographic Sciences Library 32. Springer, P. O. Box 17, 3300 AA Dordrecht, The Netherlands, third edition, 2005. 7

A. W. Brewer. Evidence for a world circulation provided by the measurements of helium and water vapour distribution in the stratosphere. *Quarterly Journal of the Royal Meteorological Society*, 75(326):351–363, 1949. ISSN 1477-870X. doi: 10.1002/qj.49707532603. URL http://dx.doi.org/10.1002/qj.49707532603. 2

F. Bunzel and H. Schmidt. The Brewer-Dobson circulation in a changing climate: impact of the model configuration. *J. Atmos. Sci.*, 70:14371455, 2013. 3

N. Butchart. The Brewer-Dobson circulation. *Rev. Geophys.*, 52(2):157–184, 2014. doi: 10.1002/2013RG000448. 3, 10

N. Butchart and A. A. Scaife. Removal of chlorofluorocarbons by increased mass exchange between the stratosphere and troposphere in a changing climate. *Nature*, 410:799–802, 2001. doi: doi:10.1038/35071047. 3

N. Butchart, A. A. Scaife, M. Bourqui, J. de Grandpre, S. H. E. Hare, J. Kettleborough, U. Langematz, E. Manzini, F. Sassi, K. Shibata, D. Shindell, and M. Sigmond. Simulations of anthropogenic change in the strength of the Brewer-Dobson circulation. *Clim. Dyn.*, 27(7-8):727–741, 2006. doi: 10.1007/s00382-006-0162-4. 3

N. Butchart, I. Cionni, V. Eyring, T. G. Shepherd, D. W. Waugh, H. Akiyoshi, J. Austin, C. Brühl, M. P. Chipperfield, E. Cordero, M. Dameris, R. Deckert,

S. Dhomse, S. M. Frith, R. R. Garcia, A. Gettelman, M. A. Giorgetta, D. E. Kinnison, F. Li, E. Mancini, C. McLandress, S. Pawson, G. Pitari, D. A. Plummer, E. Rozanov, F. Sassi, J. F. Scinocca, K. Shibata, B. Steil, and W. Tian. Chemistry-climate model simulations of twenty–first century stratospheric climate and circulation changes. *J. Climate*, 23:53495374, 2010. 3

N. Calvo and R. R. Garcia. Wave forcing of the tropical upwelling in the lower stratosphere under increasing concentrations of greenhouse gases. *J. Atmos. Sci.*, 66: 31843196, 2009. 3

Ping Chen. Isentropic cross-tropopause mass exchange in the extratropics. *Journal of Geophysical Research: Atmospheres*, 100(D8):16661–16673, 1995. ISSN 2156-2202. doi: 10.1029/95JD01264. URL http://dx.doi.org/10.1029/95JD01264. 106

M. Chirkov, G. P. Stiller, A. Laeng, S. Kellmann, T. von Clarmann, C. Boone, J. W. Elkins, A. Engel, N. Glatthor, U. Grabowski, C. M. Harth, M. Kiefer, F. Kolonjari, P. B. Krummel, A. Linden, C. R. Lunder, B. R. Miller, S. A. Montzka, J. Mühle, S. O'Doherty, J. Orphal, R. G. Prinn, G. Toon, M. K. Vollmer, K. A. Walker, R. F. Weiss, A. Wiegele, and D. Young. Global HCFC-22 measurements with MIPAS: retrieval, validation, global distribution and its evolution over 2005-2012. *Atmos. Chem. Phys.*, 16(5):3345–3368, 2016. doi: 10.5194/acp-16-3345-2016. 72

R.A. Craig. *The Upper Atmosphere: Meteorology and Physics*. International Geophysics Series. Academic Press, 1965. 70

M. Diallo, B. Legras, and A. Chédin. Age of stratospheric air in the ERA-Interim. *Atmos. Chem. Phys.*, 12(24):12133–12154, 2012. doi: 10.5194/acp-12-12133-2012. 4, 82, 99, 105, 106, 127

G. M. B. Dobson. Origin and distribution of the polyatomic molecules in the atmosphere. *Proceedings of the Royal Society of London A: Mathematical, Physical and Engineering Sciences*, 236(1205):187–193, 1956. ISSN 0080-4630. doi: 10.1098/rspa.1956.0127. URL http://rspa.royalsocietypublishing.org/content/236/1205/187. 2

G. M. B. Dobson, D. N. Harrison, and J. Lawrence. Measurements of the amount of ozone in the earth's atmosphere and its relation to other geophysical conditions. part iii. *Proceedings of the Royal Society of London A: Mathematical, Physical and Engineering Sciences*, 122(790):456–486, 1929. ISSN 0950-1207. doi: 10.1098/rspa.

1929.0034. URL http://rspa.royalsocietypublishing.org/content/122/790/456. 2

A. R. Douglass, R. S. Stolarski, M. R. Schoeberl, C. H. Jackman, M. L. Gupta, P. A. Newman, J. E. Nielsen, and E. L. Fleming. Relationship of loss, mean age of air and the distribution of CFCs to stratospheric circulation and implications for atmospheric lifetimes. *J. Geophys. Res.*, 113:D14309, 2008. doi: 10.1029/2007JD009575. 3

A. Engel, T. Möbius, H.-P. Haase, H. Bönisch, T. Wetter, U. Schmidt, I. Levin, T. Reddmann, H. Oelhaf, G. Wetzel, K. Grunow, N. Huret, and M. Pirre. Observation of mesospheric air inside the arctic stratospheric polar vortex in early 2003. *Atmos. Chem. Phys.*, 6:267–282, 2006. 65

A. Engel, T. Möbius, H. Bönisch, U. Schmidt, R. Heinz, I. Levin, E. Atlas, S. Aoki, T. Nakazawa, S. Sugawara, F. Moore, D. Hurst, J. Elkins, S. Schauffler, A. Andrews, and K. Boering. Age of stratospheric air unchanged within uncertainties over the past 30 years. *Nature Geosci.*, 2:28–31, 2009. doi: 10.1038/ngeo388. i, 3, 4, 86, 87, 90, 91, 92, 115, 120, 126, 128, 146

H. Fischer, C. Blom, H. Oelhaf, B. Carli, M. Carlotti, L. Delbouille, D. Ehhalt, J.-M. Flaud, I. Isaksen, M. López-Puertas, C. T. McElroy, and R. Zander. *Envisat-MIPAS, an instrument for atmospheric chemistry and climate research.* European Space Agency-Report SP-1229, C. Readings and R. A. Harris (eds.), ESA Publications Division, ESTEC, P. O. Box 299, 2200 AG Noordwijk, The Netherlands, 2000. 19

H. Fischer, M. Birk, C. Blom, B. Carli, M. Carlotti, T. von Clarmann, L. Delbouille, A. Dudhia, D. Ehhalt, M. Endemann, J. M. Flaud, R. Gessner, A. Kleinert, R. Koopmann, J. Langen, M. López-Puertas, P. Mosner, H. Nett, H. Oelhaf, G. Perron, J. Remedios, M. Ridolfi, G. Stiller, and R. Zander. MIPAS: an instrument for atmospheric and climate research. *Atmos. Chem. Phys.*, 8:2151–2188, 2008. 19, 20, 21

J.-M. Flaud, C. Piccolo, B. Carli, A. Perrin, L. H. Coudert, J.-L. Teffo, and L. R. Brown. Molecular line parameters for the MIPAS (Michelson Interferometer for Passive Atmospheric Sounding) experiment. *Atmos. Oceanic Opt.*, 16(3):172–182, March 2003. 49

B. Funke and M. Höpfner. Non-LTE and radiative transfer. In G. P. Stiller, editor, *The Karlsruhe Optimized and Precise Radiative transfer Algorithm (KOPRA)*, Wis-

senschaftliche Berichte FZKA 6487, pages 101–106. Forschungszentrum Karlsruhe, 2000. 28, 39

B. Funke, M. López-Puertas, S. Gil-López, T. von Clarmann, G. P. Stiller, H. Fischer, and S. Kellmann. Downward transport of upper atmospheric NO_x into the polar stratosphere and lower mesosphere during the Antarctic 2003 and Arctic 2002/2003 winters. *J. Geophys. Res.*, 110:D24308, 2005. doi: 10.1029/2005JD006463. 105, 115

R. R. Garcia and W. J. Randel. Acceleration of the Brewer-Dobson circulation due to increases in greenhouse gases. *J. Atmos. Sci.*, 65(8):2731–2739, 2008. doi: 10.1175/2008JAS2712.1. 3

H. Garny, T. Birner, H. Bönisch, and F. Bunzel. The effects of mixing on age of air. *J. Geophys. Res. Atmos.*, 119(12):7015–7034, 2014. doi: 10.1002/2013JD021417. 16, 17, 99

F. J. Haenel, G. P. Stiller, T. von Clarmann, B. Funke, E. Eckert, N. Glatthor, U. Grabowski, S. Kellmann, M. Kiefer, A. Linden, and T. Reddmann. Reassessment of MIPAS age of air trends and variability. *Atmos. Chem. Phys.*, 15(22):13161–13176, 2015. doi: 10.5194/acp-15-13161-2015. 5, 85, 86, 107, 108, 120

T. W. N. Haine, H. Zhang, D. W. Waugh, and M. Holzer. On transit times distributions in unsteady circulation models. *Ocean Mod.*, 21:35–45, 2008. 14, 15, 16

B. D. Hall, G. S. Dutton, D. J. Mondeel, J. D. Nance, M. Rigby, J. H. Butler, F. L. Moore, D. F. Hurst, and J. W. Elkins. Improving measurements of SF_6 for the study of atmospheric transport and emissions. *Atmos. Meas. Tech.*, 4:2441–2451, 2011. doi: 10.5194/amt-4-2441-2011. 59

T. M. Hall and R. A. Plumb. Age as a diagnostic of stratospheric transport,. *J. Geophys. Res.*, 99(D1):1059–1070, 1994. 3, 10, 11, 12, 13, 14, 58, 59

T. M. Hall, D. W. Waugh, K. A. Boering, and R. A. Plumb. Evaluation of transport in stratospheric models. *J. Geophys. Res.*, 104(D15):18,815–18,839, 1999. 82, 83, 145

Steven C. Hardiman, Neal Butchart, and Natalia Calvo. The morphology of the Brewer-Dobson circulation and its response to climate change in CMIP5 simulations. *Quarterly Journal of the Royal Meteorological Society*, 140(683):1958–1965, 2014. ISSN 1477-870X. doi: 10.1002/qj.2258. URL http://dx.doi.org/10.1002/qj.2258. 113

J. Harnisch, R. Borchers, P. Fabian, and M. Maiss. Tropospheric trends for CF_4 and C_2F_6 since 1982 derived from SF_6 dated stratospheric air. *Geophys. Res. Lett.*, 23 (10):1099–1102, 1996. 83

M. I. Hegglin and T. G. Shepherd. O_3–N_2O correlations from the Atmospheric Chemistry Experiment: Revisiting a diagnostic of transport and chemistry in the stratosphere. *J. Geophys. Res.*, 112:D19301, 2007. doi: 10.1029/2006JD008281. 106

J. R. Holton. On the global exchange of mass between the stratosphere and troposphere. *Journal of the Atmospheric Sciences*, 47(3):392–395, 1990. doi: 10.1175/1520-0469(1990)047⟨0392:OTGEOM⟩2.0.CO;2. URL http://dx.doi.org/10.1175/1520-0469(1990)047<0392:OTGEOM>2.0.CO;2. 10

J. R. Holton, P. H. Haynes, M. E. McIntyre, A. R. Douglass, R. B. Rood, and L. Pfister. Stratosphere-troposphere exchange. *Rev. Geophys.*, 33(4):403–439, 1995. 8

James R. Holton. *An introduction to dynamic meteorology*. International Geophysics Series. Elsevier Academic Press,, Burlington, MA, 4 edition, 2004. ISBN 9780123540157. 8

M. Höpfner. Derivatives and interface to the retrieval. In G. P. Stiller, editor, *The Karlsruhe Optimized and Precise Radiative transfer Algorithm (KOPRA)*, Wissenschaftliche Berichte FZKA 6487, pages 133–144. Forschungszentrum Karlsruhe, 2000. 27

H. Kida. General circulation of air parcels and transport characteristics derived from a hemispheric GCM, Part 2, Very long-term motions of air parcels in the troposphere and stratosphere. *J. Meteorol. Soc. Jpn.*, 61:510–522, 1983. 10

M. K. W. Ko, N. D. Sze, W.-C. Wang, G. Shia, A. Goldman, F. J. Murcray, D. G. Murcray, and C. P. Rinsland. Atmospheric sulfur hexafluoride: Sources, sinks and greenhouse warming. *J. Geophys. Res.*, 98(D6):10,499–10,507, 1993. doi: 10.1029/93JD00228. 17

P. Konopka, F. Ploeger, B. Legras, M. Tao, L. Poshyvailo, X. Yan, J. Wright, R. Müller, and M. Riese. How robust are stratospheric H_2O and AoA trends derived from different re-analysis products?, 2016. SPARC Data Assimilation (DA) Workshop and SPARC Reanalysis Intercomparison Project (S-RIP) Workshop October 17- 21, 2016 Victoria, BC, Canada. 124

Paul Konopka, Felix Ploeger, Mengchu Tao, Thomas Birner, and Martin Riese. Hemispheric asymmetries and seasonality of mean age of air in the lower stratosphere: Deep versus shallow branch of the Brewer-Dobson circulation. *Journal of Geophysical Research: Atmospheres*, 120(5):2053–2066, 2015. ISSN 2169-8996. doi: 10.1002/2014JD022429. URL http://dx.doi.org/10.1002/2014JD022429. 2014JD022429. 10, 62, 82, 108, 110, 111, 113, 147, 148

W. Kouker, D. Offermann, V. Küll, T. Reddmann, R. Ruhnke, and A. Franzen. Streamers observed by the CRISTA experiment and simulated in the KASIMA model. *J. Geophys. Res.*, 104(D13):16,405–16,418, 1999. 122

T. Kovács, W. Feng, A. Totterdill, J. M. C. Plane, S. Dhomse, J. C. Gómez-Martín, G. P. Stiller, F. J. Haenel, C. Smith, P. M. Forster, R. R. García, D. R. Marsh, and M. P. Chipperfield. Determination of the atmospheric lifetime and global warming potential of sulphur hexafluoride using a three-dimensional model. *Atmospheric Chemistry and Physics Discussions*, 2016:1–32, 2016. doi: 10.5194/acp-2016-671. URL http://www.atmos-chem-phys-discuss.net/acp-2016-671/. 17, 61

E. Kyrölä, J. Tamminen, V. Sofieva, J. L. Bertaux, A. Hauchecorne, F. Dalaudier, D. Fussen, F. Vanhellemont, O. Fanton d'Andon, G. Barrot, M. Guirlet, T. Fehr, and L. Saavedra de Miguel. GOMOS O_3, NO_2, and NO_3 observations in 2002-2008. *Atmos. Chem. Phys.*, 10(16):7723–7738, 2010. doi: 10.5194/acp-10-7723-2010. 86

A. Laeng, J. Plieninger, T. von Clarmann, U. Grabowski, G. Stiller, E. Eckert, N. Glatthor, F. Haenel, S. Kellmann, M. Kiefer, A. Linden, S. Lossow, L. Deaver, A. Engel, M. Hervig, I. Levin, M. McHugh, S. Noël, G. Toon, and K. Walker. Validation of MIPAS IMK/IAA methane profiles. *Atmos. Meas. Tech.*, 8(12):5251–5261, 2015. doi: 10.5194/amt-8-5251-2015. 69

F. Li, J. Austin, and J. Wilson. The strength of the Brewer-Dobson circulation in a changing climate: coupled chemistry-climate model simulations. *J. Climate*, 21: 40–57, 2008. 3

F. Li, R. S. Stolarski, and P. A. Newman. Stratospheric ozone in the post-CFC era. *Atmos. Chem. Phys.*, 9(6):2207–2213, 2009. 3

Feng Li, Darryn W. Waugh, Anne R. Douglass, Paul A. Newman, Steven Pawson, Richard S. Stolarski, Susan E. Strahan, and J. Eric Nielsen. Seasonal variations of stratospheric age spectra in the Goddard Earth Observing System Chemistry

Climate Model (GEOSCCM). *Journal of Geophysical Research: Atmospheres*, 117 (D5):n/a–n/a, 2012. ISSN 2156-2202. doi: 10.1029/2011JD016877. URL http://dx.doi.org/10.1029/2011JD016877. 16, 99, 105, 106

Kuo-Nan Liou. *An Introduction to Atmospheric Radiation*, volume 26. Academic Press Inc., 1980. 25, 26, 27

E. Mahieu, M. P. Chipperfield, J. Notholt, T. Reddmann, J. Anderson, P. F. Bernath, T. Blumenstock, M. T. Coffey, S. S. Dhomse, W. Feng, B. Franco, L. Froidevaux, D. W. T. Griffith, J. W. Hannigan, F. Hase, R. Hossaini, N. B. Jones, I. Morino, I. Murata, H. Nakajima, M. Palm, C. Paton-Walsh, J. M. Russell III, M. Schneider, C. Servais, D. Smale, and K. A. Walker. Recent northern hemisphere stratospheric HCl increase due to atmospheric circulation changes. *Nature*, 515:104–107, 2014. 4, 124

M. Maiss and I. Levin. Global increase of SF_6 observed in the atmosphere. *Geophys. Res. Lett.*, 21(7):569–572, 1994. 17

C. McLandress and T. G. Shepherd. Simulated anthropogenic changes in the Brewer-Dobson circulation, including its extension to high latitudes. *J. Clim.*, 22:1516–1540, 2009. doi: 10.1175/2008JCLI2679.1. 3

B. M. Monge-Sanz, M. P. Chipperfield, D. P. Dee, A. J. Simmons, and S. M. Uppala. Improvements in the stratospheric transport achieved by a chemistry transport model with ECMWF (re)analyses: identifying effects and remaining challenges. *Quarterly Journal of the Royal Meteorological Society*, 139(672):654–673, 2013. ISSN 1477-870X. doi: 10.1002/qj.1996. URL http://dx.doi.org/10.1002/qj.1996. 4, 124

R. R. Neely III, J. M. English, O. B. Toon, S. Solomon, M. Mills, and J. P. Thayer. Implications of extinction due to meteoritic smoke in the upper stratosphere. *Geophys. Res. Lett.*, 38(24):L24808, 2011. doi: 10.1029/2011GL049865. 43

H. Norton and R. Beer. New apodizing functions for Fourier spectrometry. *J. Opt. Soc. Am*, 66(3):259–264, 1976. (Errata J. Opt. Soc. Am., 67, 419,1977). 23

Sophie Oberländer, Ulrike Langematz, and Stefanie Meul. Unraveling impact factors for future changes in the Brewer-Dobson circulation. *Journal of Geophysical Research: Atmospheres*, 118(18):10,296–10,312, 2013. ISSN 2169-8996. doi: 10.1002/jgrd.50775. URL http://dx.doi.org/10.1002/jgrd.50775. 3

K. Okamoto, K. Sato, and H. Akiyoshi. A study on the formation and trend of the Brewer-Dobson circulation. *Journal of Geophysical Research: Atmospheres*, 116 (D10):n/a–n/a, 2011. ISSN 2156-2202. doi: 10.1029/2010JD014953. URL http://dx.doi.org/10.1029/2010JD014953. 3

Scott M. Osprey, Lesley J. Gray, Steven C. Hardiman, Neal Butchart, and Tim J. Hinton. Stratospheric variability in twentieth-century CMIP5 simulations of the Met Office Climate Model: High top versus low top. *Journal of Climate*, 26(5): 1595–1606, 2013. doi: 10.1175/JCLI-D-12-00147.1. 113

G.W. Petty. *A first course in atmospheric radiation*. Sundog Publishing, 2004. ISBN 0972903305. 26

F. Ploeger and T. Birner. Seasonal and inter-annual variability of lower stratospheric age of air spectra. *Atmospheric Chemistry and Physics*, 16(15):10195–10213, 2016. doi: 10.5194/acp-16-10195-2016. URL http://www.atmos-chem-phys.net/16/10195/2016/. 15, 16, 61, 62, 97, 98, 106, 114, 143

F. Ploeger, M. Abalos, T. Birner, P. Konopka, B. Legras, R. Müller, and M. Riese. Quantifying the effects of mixing and residual circulation on trends of stratospheric mean age of air. *Geophysical Research Letters*, 42(6):2047–2054, 2015a. ISSN 1944-8007. doi: 10.1002/2014GL062927. URL http://dx.doi.org/10.1002/2014GL062927. 2014GL062927. 16, 17, 115, 127, 128, 148

F. Ploeger, M. Riese, F. Haenel, P. Konopka, R. Müller, and G. Stiller. Variability of stratospheric mean age of air and of the local effects of residual circulation and eddy mixing. *J. Geophys. Res. Atmos.*, 120(2):716–733, 2015b. doi: 10.1002/2014JD022468. 4, 105, 106, 114, 120, 121, 124, 148

R. A. Plumb. A "tropical pipe" model of stratospheric transport. *J. Geophys. Res.*, 101(D2):3957–3972, 1996. 8

W. J. Randel, F. Wu, H. Vömel, G. E. Nedoluha, and P. Forster. Decreases in stratospheric water vapor after 2001: Links to changes in the tropical tropopause and the Brewer–Dobson circulation. *J. Geophys. Res.*, 111:D12312, 2006. doi: 10.1029/2005JD006744. 82

A. R. Ravishankara, S. Solomon, A. A. Turnipseed, and R. F. Warren. Atmospheric lifetimes of long-lived halogenated species. *Science*, 259(5092):194–199, 1993. doi: 10.1126/science.259.5092.194. 17

E. A. Ray, F. L. Moore, J. W. Elkins, G. S. Dutton, D. W. Fahey, H. Vömel, S. J. Oltmans, and K. H. Rosenlof. Transport into the Northern Hemisphere lowermost stratosphere revealed by in situ tracer measurements. *J. Geophys. Res.*, 104(D21): 26,565–26,580, 1999. doi: 10.1029/1999JD900323. 83

T. Reddmann, R. Ruhnke, and W. Kouker. Three–dimensional model simulations of SF_6 with mesospheric chemistry. *J. Geophys. Res.*, 106(D13):14,525–14,537, 2001. doi: 10.1029/2000JD900700. 17, 122

T. Reddmann, R. Ruhnke, S. Versick, and W. Kouker. Modeling disturbed stratospheric chemistry during solar-induced NOx enhancements observed with MIPAS/ENVISAT. *Journal of Geophysical Research: Atmospheres*, 115(D1):n/a–n/a, 2010. ISSN 2156-2202. doi: 10.1029/2009JD012569. URL http://dx.doi.org/10.1029/2009JD012569. 122

G. C. Reid and K. S. Gage. On the annual variation in height of the tropical tropopause. *J. Atmos. Sci.*, 38:1928–1938, 1981. 70, 74

J. J. Remedios, R. J. Leigh, A. M. Waterfall, D. P. Moore, H. Sembhi, I. Parkes, J. Greenhough, M. P. Chipperfield, and D. Hauglustaine. MIPAS reference atmospheres and comparisons to V4.61/V4.62 MIPAS level 2 geophysical data sets. *Atmos. Chem. Phys. Discuss.*, 7:9973–10017, 2007. 40, 46, 47, 48

D. Rind, R. Suozzo, N. K. Balachandran, and M. J. Prather. Climate change and the middle atmosphere. part i: the doubled CO_2 climate. *J. Atmos. Sci.*, 47:465–494, 1990. 3

C. D. Rodgers. *Inverse Methods For Atmospheric Sounding - Theory And Practice*, volume 2. World Scientific, 2000. 31, 34

W. Roedel. *Physik unserer Umwelt: die Atmosphäre*. Springer, 2000. ISBN 9783540671800. 7, 9

Karen H. Rosenlof. Seasonal cycle of the residual mean meridional circulation in the stratosphere. *Journal of Geophysical Research: Atmospheres*, 100(D3):5173–5191, 1995. ISSN 2156-2202. doi: 10.1029/94JD03122. URL http://dx.doi.org/10.1029/94JD03122. 10, 61, 107

L. S. Rothman, A. Barbe, D. C. Benner, L. R. Brown, C. Camy-Peyret, M. R. Carleer, K. Chance, C. Clerbaux, V. Dana, V. M. Devi, A. Fayt, J.-M. Flaud, R. R. Gamche,

A. Goldman, D. Jacquemart, K. W. Jucks, W. J. Lafferty, J.-Y. Mandin, S. T. Massie, V. Nemtchinov, D. A. Newnham, A. Perrin, C. P. Rinsland, J. Schroeder, K. M. Smith, M. A. H. Smith, K. Tang, R. A. Toth, J. Vander Auwera, P. Varanasi, and K. Yoshino. The HITRAN molecular spectroscopic database: edition of 2000 including updates through 2001. *J. Quant. Spectrosc. Radiat. Transfer*, 82:5–44, 2003. doi: 10.1016/S0022-4073(03)00146-8. 29, 49

R. Ruhnke, W. Kouker, and T. Reddmann. The influence of the OH+NO_2+M reaction on the NO_y partitioning in the late Arctic winter 1992/1993 as studied with KASIMA. *J. Geophys. Res.*, 104(D3):3755–3772, 1999. 122

M. R. Schoeberl, A. R. Douglass, B. Polansky, C. Boone, K. A. Walker, and P. Bernath. Estimation of stratospheric age spectrum from chemical tracers. *J. Geophys. Res.*, 110:D21303, 2005. doi: 10.1029/2005JD006125. 14

William J. M. Seviour, Neal Butchart, and Steven C. Hardiman. The Brewer-Dobson circulation inferred from ERA-Interim. *Quarterly Journal of the Royal Meteorological Society*, 138(665):878–888, 2012. ISSN 1477-870X. doi: 10.1002/qj.966. URL http://dx.doi.org/10.1002/qj.966. 61

P. E. Sheese, C. D. Boone, and K. A. Walker. Detecting physically unrealistic outliers in ACE-FTS atmospheric measurements. *Atmospheric Measurement Techniques*, 8(2): 741–750, 2015. doi: 10.5194/amt-8-741-2015. URL http://www.atmos-meas-tech.net/8/741/2015/. 119

T. G. Shepherd. Dynamics, stratospheric ozone, and climate change. *Atmosphere-Ocean*, 46(1):117–138, 2008. doi: 10.3137/ao.460106. 3

SPARC CCMVal. Neu, J. and S. Strahan, Chapter 5. Transport. In V. Eyring, T. G. Shepherd, and D. W. Waugh, editors, *SPARC Report on the Evaluation of Chemistry-Climate Models*. SPARC Report No. 5, WCRP-132, WMO/TD-No. 1526, 2010. URL http://www.atmosp.physics.utoronto.ca/SPARC. 82

T. Steck. *Bestimmung von Vertikalprofilen von Spurengasen aus MIPAS–Messungen unter Hinzunahme von a priori Wissen*. PhD thesis, Institut für Meteorologie und Klimaforschung, Universität Karlsruhe, Kernforschungszentrum Karlsruhe, 2000. Dissertation, DLR–FB 2000–01, ISSN 1434-8454. 27, 143

T. Steck. Methods for determining regularization for atmospheric retrieval problems. *Appl. Opt.*, 41(9):1788–1797, 2002. 44, 54

G. P. Stiller, editor. *The Karlsruhe Optimized and Precise Radiative Transfer Algorithm (KOPRA)*, volume FZKA 6487 of *Wissenschaftliche Berichte*. Forschungszentrum Karlsruhe, 2000. 24, 28, 39

G. P. Stiller, T. von Clarmann, B. Funke, N. Glatthor, F. Hase, M. Höpfner, and A. Linden. Sensitivity of trace gas abundances retrievals from infrared limb emission spectra to simplifying approximations in radiative transfer modelling. *J. Quant. Spectrosc. Radiat. Transfer*, 72(3):249–280, 2002. 39

G. P. Stiller, T. v. Clarmann, M. Höpfner, N. Glatthor, U. Grabowski, S. Kellmann, A. Kleinert, A. Linden, M. Milz, T. Reddmann, T. Steck, H. Fischer, B. Funke, M. López-Puertas, and A. Engel. Global distribution of mean age of stratospheric air from MIPAS SF_6 measurements. *Atmos. Chem. Phys.*, 8:677–695, 2008. 4, 39, 40, 42, 43, 44, 50, 55, 63, 122

G. P. Stiller, T. von Clarmann, F. Haenel, B. Funke, N. Glatthor, U. Grabowski, S. Kellmann, M. Kiefer, A. Linden, S. Lossow, and M. López-Puertas. Observed temporal evolution of global mean age of stratospheric air for the 2002 to 2010 period. *Atmos. Chem. Phys.*, 12:3311–3331, 2012. doi: 10.5194/acp-12-3311-2012. i, 4, 39, 40, 42, 43, 44, 48, 50, 52, 58, 59, 60, 82, 85, 86, 87, 89, 90, 103, 105, 107, 125, 126

A. Tikhonov. On the solution of incorrectly stated problems and method of regularization. *Dokl. Akad. Nauk. SSSR*, 151(3):501–504, 1963. 33, 44

P. Varanasi, Z. Li, V. Nemtchinov, and A. Cherukuri. Spectral absorption-coefficient data on HCFC-22 and SF_6 for remote-sensing applications. *J. Quant. Spectrosc. Radiat. Transfer*, 52(3/4):323–332, 1994. doi: 10.1016/0022-4073(94)90162-7. 29

T. von Clarmann. Zur Fernerkundung der Erdatmosphäre mittels Infrarotspektrometrie: Rekonstruktionstheorie und Anwendung. Wissenschaftliche Berichte FZKA 6928, Forschungszentrum Karlsruhe, 2003. 23, 29, 37

T. von Clarmann. Smoothing error pitfalls. *Atmos. Meas. Tech.*, 7:3023–3034, 2014. doi: 10.5194/amtd-7-3023-2014. 36

T. von Clarmann, N. Glatthor, U. Grabowski, M. Höpfner, S. Kellmann, M. Kiefer, A. Linden, G. Mengistu Tsidu, M. Milz, T. Steck, G. P. Stiller, D. Y. Wang, H. Fischer, B. Funke, S. Gil-López, and M. López-Puertas. Retrieval of temperature and tangent altitude pointing from limb emission spectra recorded from space by the

Michelson Interferometer for Passive Atmospheric Sounding (MIPAS). *J. Geophys. Res.*, 108(D23):4736, 2003. doi: 10.1029/2003JD003602. 23, 38, 39, 57

T. von Clarmann, M. Höpfner, S. Kellmann, A. Linden, S. Chauhan, B. Funke, U. Grabowski, N. Glatthor, M. Kiefer, T. Schieferdecker, G. P. Stiller, and S. Versick. Retrieval of temperature, H_2O, O_3, HNO_3, CH_4, N_2O, $ClONO_2$ and ClO from MIPAS reduced resolution nominal mode limb emission measurements. *Atmos. Meas. Techn. Discuss.*, 2:181–236, 2009. 39

T. von Clarmann, G. Stiller, U. Grabowski, E. Eckert, and J. Orphal. Technical note: Trend estimation from irregularly sampled, correlated data. *Atmos. Chem. Phys.*, 10:6737–6747, 2010. 86, 89

D. W. Waugh and T. M. Hall. Age of stratospheric air: theory, observations, and models. *Rev. Geophys.*, 40(4):1010, 2002. doi: 10.1029/2000RG000101. 3, 11, 12, 13, 14, 59, 60, 82, 83, 99, 145

S. Zorn, T. von Clarmann, G. Echle, B. Funke, F. Hase, M. Höpfner, H. Kemnitzer, M. Kuntz, and G. P. Stiller. Analytical expressions for modeling of radiative transfer and instrumental effects in KOPRA. In G. P. Stiller, editor, *The Karlsruhe Optimized and Precise Radiative transfer Algorithm (KOPRA)*, Wissenschaftliche Berichte FZKA 6487, pages 9–27. Forschungszentrum Karlsruhe, 2000. 28

List of Figures

List of Tables

Acknowledgements

This work was funded by the "CAWSES" priority programme of the German Research Foundation (DFG) under project STI 210/5-3 and by the German Federal Ministry of Education and Research (BMBF) within the "ROMIC" programme under project 01LG1221B. I would like to acknowledge provision of MIPAS level 1b data by ESA and the SF_6 data from the NOAA/ESRL halocarbons in-situ programme.

I would like to thank:

- Prof. Dr. Johannes Orphal for giving me the opportunity to do my PhD at his institute, for being my PhD adviser and for supporting me for such a long time.
- PD Dr. Michael Höpfner for being my second examiner and his interest in my work.
- Dr. Gabriele Stiller and PD Dr. Thomas von Clarmann for the outstanding excellent supervision of my work, for all the intensive discussions and for supporting me through all the years.
- Dr. Norbert Glatthor for all his help especially with the MIPAS spectroscopy.
- Andrea Linden, Sylvia Kellmann and Dr. Udo Grabowski for their support and help with the MIPAS retrieval processor.
- Dr. Gabriele Stiller, Dr. Thomas von Clarmann, Johannes Plieninger, Ellen Eckert, Dr. Alexandra Laeng, Dr. Norbert Glatthor and Dr. Michael Kiefer for help with and providing IDL and Fortran routines.
- Dr. Thomas Reddmann for providing SF_6 data simulated by the KASIMA model and helpful discussions.
- Dr. Felix Ploeger for the excellent collaboration, providing age spectra simulated by the CLaMS model and all the helpful discussions on age of air.

- Prof. Dr. Andreas Engel for providing SF_6 cryosampler data and his support within the ROMIC programme.
- Prof. Dr. Kaley Walker for providing and her help with ACE-FTS SF_6 data.
- Dr. Alexandra Laeng for her help with MIPAS validation.
- Dr. Gabriele Stiller, Dr. Thomas von Clarmann and Andrea Linden for proofreading of my thesis.
- Dr. Bernd Funke and Prof. Dr. Manuel López-Puertas for their help with Non-LTE, helpful discussions and organising interesting MIPAS Data User Meetings in Granada.
- Prof. Dr. Ulrike Langematz for letting me take part at the interesting SHARP-meetings and Dr. Felix Bunzel for helpful discussions on the Brewer-Dobson circulation.
- The whole satellite group of IMK-ASF for their support and the nice working atmosphere.
- Johannes Plieninger, Dr. Udo Grabowski, Johann Seemayer and Dr. Arne Babenhauserheide for technical help with the computers and the cluster.
- Mrs. Wiessner, Derya Cayiroglu and Sandra Leist for their help and organisation.
- My family, especially my father Matthias Haenel, my brother Alexander Haenel, my aunt Katharina Haenel and my uncle Leopold Haenel for all their support and everything.
- All the PhD students and young researchers of IMK-ASF, especially Stefan Bender, Johannes Plieninger, Ellen Eckert, Tobias Schieferdecker, Mahesh Kumar Sha, Wolfgang Woiwode, Andreas Wiegele, Jennifer Schröter, Matthäus Kiel, Sören Johansson, Katharina Maurer, Matthias Frey, Annika Günther, Darko Dubravica, Stefan Versick, Arne Babenhauserheide, Alexey Vlasov, Johannes Eckstein, Qiansi Tu, Ugur Cayoglu as well as the tennis community for distraction, their support and the nice time.
- My friends from home Hossam Ali, Ahmed Ali, Boris Schulze and Gerburg Muder for their support in difficult times.